

TWINNING AND NONLINEAR OPTICS

by

ANDREI SZILAGYI

B.A., Harvard University

(1976)

SUBMITTED IN PARTIAL FULFILLMENT
OF THE REQUIREMENTS OF THE
DEGREE OF

DOCTOR OF PHILOSOPHY

at the

MASSACHUSETTS INSTITUTE OF TECHNOLOGY

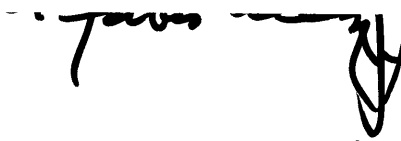
January 1984

© Massachusetts Institute of Technology 1984

Signature of Author —

Department of Physics
January 5, 1984

Certified by —



C. Forbes Dewey, Jr.
Thesis Supervisor

Accepted by —

George F. Koster
Chairman, Departmental Graduate Committee

MASSACHUSETTS INSTITUTE
OF TECHNOLOGY

MAR 14 1984

LIBRARIES

ARCHIVES

TWINNING AND NONLINEAR OPTICS

by

ANDREI SZILAGYI

Submitted to the Department of Physics
in partial fulfillment of the requirements
for the Degree of Doctor of Philosophy
January 5, 1984

ABSTRACT

A comprehensive theory of quasi-phase-matched (QPM) three-wave interactions in twinned plates of $\bar{4}3m$ semiconductors is developed. The 180° phase change required by QPM is studied by treating the nonlinear polarization as a bilinear form in the applied electric field and decomposing it into invariant and sign changing parts under a 2-fold rotation of an arbitrary crystal lattice. A new 3×3 matrix representation of the third rank nonlinear susceptibility tensor is found for all crystal classes. In the $\bar{4}3m$ case the decomposition of this form results in sufficiently compact expressions enabling the evaluation of the nonlinear polarization generated by mixing elliptically polarized waves. The theory shows that use of circularly polarized light is a factor of two more efficient than the conventional linearly polarized light.

The predicted 1% second harmonic generation (SHG) efficiency is verified experimentally for a stack of 6 twinned CdTe plates in a Brewster-angle immersion cell using carbon disulphide as index matching medium

While SHG was demonstrated in selected twinned material, practical implementation requires either routine optical contacting of large stacks of twinned plates, or the achievement of controlled twinning during crystal growth. The brittleness of CdTe renders the former alternative difficult to implement. The latter alternative, however, is shown to hold significant promise of success.

CdTe crystals were grown in a sealed Vertical Bridgman configuration. The systematics of twinning were studied and a special ampoule was designed that allowed some degree of orientational control over twin formation. The experimentally-derived observations, together with information derived from a literature survey led to the proposal of a new model of growth interface anisotropy based on the density of dangling

bonds \mathcal{N} . The 6-lobe \mathcal{N} -surface for elemental semiconductors and 12-lobe extension in the polar case both conform to the general form given by Herring in 1951, and represent the first calculation of the γ plots in these crystal systems.

The model is found to explain a variety of phenomena related to the interface anisotropy including solitary and lamellar twinning, faceting and etching. In particular, the higher twinning frequency of "A" seeded polar crystals is shown to be the result of the low density of dangling bonds exposed to the melt in that orientation. For elemental semiconductors, a stability map against twinning is explicitly given. Although accidental and two-dimensional nucleation mechanisms are not ruled out, their use is not required. It is concluded that growth twinning represents in general a response of the advancing solid-melt interface to a change in the local kinetic undercooling and the orientation of the solidification front relative to the lattice.

An alternative model of growth twinning is also provided for materials characterized by highly-associated melts. Relatively stable 8-atom-clusters are shown to be capable of nucleating the observed oblique twins and predict the existence of a minimal thermal gradient for monocrystalline growth.

The dangling bond model provides a framework for further study of anisotropic interfacial phenomena. In particular further quantification of the lamellar mechanism holds the promise of controlled twinning for nonlinear optical applications.

Thesis Supervisor: Dr. C. Forbes Dewey, Jr.

Title: Professor of Mechanical Engineering

Table of Contents

Abstract.....p.	1
<u>I General Introduction.....p.</u>	<u>5</u>
1. Background.....p.	6
2. Acknowledgements.....p.	11
Appendices	
A1. Abbreviations.....p.	14
A2. List of figures and tables.....p.	16
References.....p.	21
<u>II Nonlinear Optics.....p.</u>	<u>23</u>
1. Introduction.....p.	24
2. Sign changes in the nonlinear polarization.....p.	27
3. The new form of $\chi^{(2)}$p.	32
4. Algebraic decomposition of P in the $\bar{4}3m$ class.... p.	35
5. Trigonometric evaluation for SHG.....p.	40
6. Frequency mixing.....p.	47
7. Elliptically polarized fundamental.....p.	51
8. (1,1,1) propagation.....p.	59
9. Summation over twinned domains.....p.	63
10. Stacking of twinned plates.....p.	66
11. Experiments.....p.	73
12. Conclusions.....p.	78
Appendices	
A1. Idealized SHG intensity in coherence-length plate (cgs).....p.	80

A2. Nonlinear susceptibilities in new matrix form.....p. 85

A3. Mixing of elliptically polarized light.....p. 90

References.....p. 93

Figures and Table.....p. 96

III. Growth Twinning.....p. 105

1. Introduction.....p. 106

2. Literature review.....p. 108

3. Experimental program.....p. 114

 3.1 Description of system

 3.2 Processing steps

 3.3 Characterization

 3.4 Highlights of growth experiments

4. Summary of observations and propositions.....p. 123

5. Dangling bond model of the growth interface.....p. 126

6. Supporting evidence and applications of the
dangling bond model.....p. 131

7. Internal lamellar twinning.....p. 138

8. Polar effects.....p. 141

9. Clustering model of growth twinning.....p. 145

10. Conclusions.....p. 150

11. Future research.....p. 152

Appendices

A1. Estimate of sticking probability during growth....p. 154

A2. Twinning operations and low index directions.....p. 156

A3. Filling factor versus coordination number.....p. 157

References.....p. 159

Figures and Tables.....p. 164

CHAPTER I

General Introduction

I.1 Background

As of this writing, the quarter-century-old field of nonlinear optics (NLO) may justifiably be said to have reached maturity. Commercially available frequency doublers and mixers are used routinely to obtain coherent radiation at frequencies not readily supplied by existing lasers. Various nonlinear optical effects have been shown to have applications in electronics, communications, energy conversion, photochemistry, spectroscopy, etc. Introductions to the field, reviews and collections of articles on NLO have been given by Bloembergen 1965, Baldwin 1969, Zernike and Midwinter 1973, Rabin and Tang 1975, Shen 1976 and 1977, Harper and Wherrett 1977, and others.

The conversion of coherent light in nonlinear crystals must overcome the problem of different phase velocities of the input and output beams. The conventional solution, called phase-matching, utilizes natural birefringence to compensate for the frequency dispersion. This approach, unfortunately, eliminates from the discussion many highly nonlinear materials with low or no birefringence.

An alternate approach called quasi-phase-matching (QPM) was proposed in one of the fundamental papers of NLO (Armstrong, Bloembergen, Ducuing and Pershan 1962), allowing the use of nonbirefringent materials. In that method, the continuously changing phase difference between the source and the output beams is discretely and periodically returned to a

favorable value by suitably modulating the optical properties of the working material. In particular, the stack-of-plates implementation of QPM (Bloembergen 1968), which accomplishes this modulation by rotating every other plate of a stack 180° about an axis normal to the propagation direction, enjoyed a flurry of interest in the mid 1970's (Yacoby, Aggarwal and Lax 1973, McMullen 1975, Okada, Takizawa and Yeiri 1976, Szilagyi, Hordvik and Schlossberg 1976 and 1977, Thompson, McMullen and Anderson 1976 and Piltch, Cantrell and Sze 1976).

Another way to modulate the nonlinear susceptibility is through an artificially (Bloembergen and Sievers 1970, Tang and Bey 1973) or naturally (Dewey and Hocker 1975, Hocker and Dewey 1976, Dewey 1976) generated domain structure. In zincblende materials, lamellar twinning provides an example of the latter structure type.

A rotational twin plane is a two-dimensional crystalline defect separating two otherwise perfect crystal domains. Adjacent domains differ in orientation by a 180° rotation about the common twin normal. Since atoms at or near the twin boundary have only minor differences in their environment compared to bulk atoms, the twin itself does not have any unusual interaction with the light field. The change in orientation across the defect, however, acts as a modulation of the effective nonlinear susceptibility.

The successful demonstration of QPM in rotationally twinned crystals by Dewey and Hocker (1975) provided the initial stimulus for this thesis. The primary objectives of

the thesis were therefore the development of a theory of frequency mixing and doubling in twinned materials and a study of growth twinning mechanisms.

The NLO part is treated in Chapter II. The theory presented therein supplies a number of new results, with varying degrees of generality. They include: a more symmetric form of $\chi^{(2)}$; a systematic procedure to identify the quasi-phase-matched portion of the nonlinear polarization; and quantitative calculations of the effects of arbitrary twin plane distributions, of stacking twinned plates and of using elliptically polarized light. The frequency doubling efficiency predicted by this theory is verified experimentally in the first demonstration of second harmonic generation by a stack of twinned plates (Szilagyı and Dewey 1979).

The difficulties encountered in optically contacting the CdTe nonlinear plates served to emphasize the necessity for controlling twinning, so that efficient devices could be constructed without stacking. The need to understand twinning, however, is even older than the field of nonlinear optics. Since the performance of many devices is impaired by the presence of grain boundaries (of which, twin planes are special examples), the electronics industry has from its inception had an interest in the control and elimination of twinning.

The investigation of growth twinning mechanisms is presented in Chapter III. Cadmium telluride ingots were grown by the sealed, Vertical Bridgman method. The observed

systematics of twinning as well as findings from the published literature led to the formulation of a model of the growth interface anisotropy. Based upon the density of dangling bonds at the solid-melt interface, this model is capable of explaining in a unified way such phenomena as solitary and lamellar twinning, faceting and etching. The calculation of the density of dangling bonds as a function of interfacial orientation is in itself new, constituting the first evaluation of the γ plot in tetrahedrally coordinated semiconductors.

The large body of evidence available in the literature supporting the presented model serves to reinforce the view that growth twinning is a feature of intrinsic materials, thus obviating the need for explanations in terms of growth accidents. However, for semiconducting materials with highly associated melts such as CdTe, a clustering model is also compatible with the observed characteristics of twinning. Metastable 8-atom clusters formed in the melt at some statistical rate lead to the qualitative prediction of a minimal thermal gradient below which single crystals cannot be grown.

In addition to explaining various phenomena associated with interfacial anisotropy, the dangling bond model of Chapter III also forms a convenient framework in terms of which future experiments can be interpreted. Moreover, the model lends itself to further extension and refinement in the context of crystal growth theory and provides good cause for

an optimistic outlook in regards to the control of growth twinning.

I.2 Acknowledgments

Over the years of graduate work, this author has had the good fortune of belonging to two major research environments at M.I.T., the Fluid Mechanics Laboratory under the direction of Professor C. Forbes Dewey, Jr. and the Electronic Materials Processing Group headed by Professor August F. Witt. I, as well as my thesis, have benefitted in many ways from interacting with more people, in these and other groups, than I could hope to list here or even recollect. Thanks are due to all, but in particular to a number of individuals whose contributions I wish to acknowledge more specifically.

As the person who brought me to M.I.T. and saw me through the thesis defense, first thanks must go to my Thesis Supervisor, Professor C. F. Dewey, Jr.. In the good times (research funding) and the hard times (no research funding) he has been there competently to reassure and advise me in matters technical and stylistic.

During the growth twinning part of my thesis I have benefitted most from my association with Professor A. F. Witt. With his guidance, my entry into the field of crystal growth was made more productive than some have thought possible. My thanks for his support and expert advice in the shaping of my recent research.

As the representative of the Physics Department on my Thesis Committee, Professor J. David Litster has helped to bring balance into my work, between nonlinear optics and

crystal growth and between theory and experiment. I am also grateful for the technical advice he has rendered during our conversations.

Here are some of the members of the Fluids Lab who have also earned my gratitude and friendship. Early on, Dr. Lon Hocker contributed helpful advice and good humor. Dick Fenner provided indispensable technical know-how and a sympathetic ear. Marj Joss, Donna Wilker and Margaret Conlin have frequently helped me weather the logistical storms associated with thesis typing and seminar preparation. Jim Harrison and John Flint have provided much needed assistance with my frequency doubling experiments. Darrell Jan and Andrea Remuzzi helped with the Hamamatsu camera observations of twin spacing.

Among members of the Electronic Materials Group, special thanks are due to Dr. Mike Wargo for his advice regarding crystal growth and other areas, notably photographic techniques. Thanks go also to Dr. Edith Bourret for her demonstration of the Bridgman growth system, to Jim Nakos for TEM micrography, Dergao Lin for the use of his high-vacuum diffusion pump, Gloria Landahl and Joe di Maria for logistical support. Very helpful technical support was also provided by Wilfred (Pat) Doucette with glass blowing, Art Gregor with macrophotography, Libby Shaw with SEM micrography, Walter Correia with analytical and spectroscopic services and Francia Lindon with professional drafting.

Acknowledgments and thanks are due to Prof. Ely

Yablonovich and Jerry Black, formerly of Harvard University, for making their laser available to me, and to Mr. James Hawkey of II-VI, Inc. for his help in the selection and fabrication of CdTe samples.

For their friendship and human touch, Chrissy Wang, Ricky Garcia and Jung-Hoon Chun have earned my special gratitude. My thanks go also to all my dancing friends who have helped me retain my physical and mental health.

Last, but not least, I wish to acknowledge the financial support in the form of research contracts from the U.S. Energy Research and Development Administration, the U.S. Air Force Weapons Laboratory and Office of Scientific Research, the Office of Naval Research, the Advanced Research Projects Agency and the U.S. Army Research Office, as well as support by the Department of Physics taking the form of the Malcolm Cotton Brown Fellowship and five semesters of teaching assistantships, without which this thesis could not have been completed.

I.A1 Abbreviations

The following abbreviations will be found in the following two chapters:

Chapter II

NLO Nonlinear Optics
QPM Quasi-Phase-Matching
SHG Second Harmonic Generation
SFG Sum Frequency Generation
DFG Difference Frequency Generation

Chapter III

SEM Scanning Electron Microscope
TEM Transmission Electron Microscope
GB Grain Boundary
GBE Grain Boundary Energy
TPE Twin Plane Energy
SFE Stacking Fault Energy
RCP Random-Close-Packed

In addition, special symbols were used, as follows:

$\hat{}$ (caret).....for unit vectors
 $\tilde{}$ (tilde).....for for the Hermitian adjoint operation

Subscripts:

+ . . . invariant under twinning operation
- . . . sign-changing under twinning operation
 \parallel . . . component along \hat{a} (twin plane normal)
 \perp . . . component parallel to a twin plane

Superscripts:

\pm . . . component along ξ_{\pm}

t . . . matrix transposition

' . . . quantity evaluated after a rotation operation

Note that negative vector components are interchangeably shown with an overbar or a minus sign. Commas are occasionally used to separate the components of row vectors.

I.A2 List of figures and tables

Figures

Chapter II

- 5.1 Crystal coordinate system and angle definitions
- 7.1 Euler angles (after Messiah 1966, Fig. XIII.1)
- 8.1 Relation between the fundamental (\vec{E}) and second harmonic (\vec{P}) polarizations for (111) propagation
- 10.1a Effective number (M) of ideal plates vs. the actual number of optically contacted plates for various phase angles $= 180^\circ r_d / l_c$
- b Effective number (M) of ideal plates vs. the actual number of coherence-length plates immersed in medium with $l_c = 29 \mu\text{m}$ for various spacings
- 11.1a Argand plot of SH field in twinned crystal
- b Argand plot for portion of the crystal selected for experiment
- 11.2 Brewster angle immersion cell (schematic)

Chapter III

- 3.1 Vertical Bridgman crystal growth set-up
- 3.2 Growth assembly
- 3.3 CdTe crystal grown by the Liquid Encapsulated Bridgman method
 - a Last to freeze region ("meniscus")
 - b Laue back-reflection from "meniscus"

- c 1000X SEM of etched "meniscus" showing crack
 - d X-ray energy dispersive analysis of "meniscus" showing segregated tellurium
 - e 59X SEM of etched, twinned CdTe boule 2mm below "meniscus"
 - f 1100X SEM of etched twin boundary showing origin of visible grain contrast
 - g External grooving (scale divisions .01 in. apart)
- 3.4a Graphite mandrel
- b, c Etched CdTe boule viewed from opposite directions, showing preferential alignment of lamellar twins
- 3.5 Etched axial cut through CdTe crystal. This boule did not wet the quartz ampoule
- 3.6a Etched axial cut through nearly single CdTe boule
- b (110) pole TEM electron diffraction (courtesy J. Nakos)
- 5.1a Nearest neighbor tetrahedral coordination showing important crystallographic directions
- b Projection of nearest neighbor tetrahedron onto the $\{1\bar{1}0\}$ plane
- 5.2 Typical dangling bond configurations of interfaces with normals in the $(1\bar{1}0)$ zone
- 5.3 Density of dangling bonds vs. interface orientation (polar plots)
- a Normals in the (001) zone
 - b Normals in the $(1\bar{1}0)$ zone
 - c Normals in the (111) zone
- 5.4 Constant density of dangling bonds contours in

stereographic projection

a (001) zenith

b (111) zenith

6.1 Etched Si single crystal (from Lee 1969)

6.2 Cusp at advancing interface, due to anisotropic growth kinetics. The density of dangling bonds for the two grains is shown in a polar plot. The kinetic undercooling is indicated qualitatively

6.3 Qualitative external faceting behavior in elemental semiconductors

a Definition of interface curvature

b, c, d Sequence of boule cross sections as a function of interface curvature

6.4 Effect of oblique ($\bar{1}11$) twinning on the density of dangling bonds for a (111) seeded crystal. The composite curves select from the two crystal orientations the one with the higher density of dangling bonds

6.5 Effect of twinning on the density of dangling bonds for a (001) seeded crystal

6.6 Stability map against twinning; a density-of-dangling-bonds composite surface for a (001) seeded crystal and all of its first-order twins (projection of the 3-dimensional surface onto the {001} surface)

6.7 Stability map against twinning; shows preferred twin operations and stable regions vs. interface orientation

7.1a, b First to freeze portion of CdTe boule showing relatively uniform lamellar twinning

7.2 Initiation of a twin lamella from a twin boundary
(schematic)

a Cusp at solid-melt interface due to orientation
difference across twin boundary

b Nucleation of second order twin including a high energy
boundary

c The favorable orientation of the new grain gives it a
lower kinetic undercooling

7.3a Atomic model of the thinnest (3 double layers) twin
lamella allowed by crystallographic constraints

b, c Etched CdTe surface showing an example of a twin
lamella (courtesy B. Fabes)

7.4a Lamellar twinning with acute dihedral angle towards the
melt

b Lamellar twinning with obtuse dihedral angle towards the
melt

8.1 Density of dangling bonds vs. interface orientation for
a polar semiconductor with $\xi = 1$

9.1 8-atom twin nucleus with an average of 1.75 dangling
bonds per atom

9.2 Initiation of oblique twin at 8-atom cluster

9.3 Crystallographically allowed oblique twin planes

9.4 Stability region (cross hatched) against twinning in
thermal gradient vs. growth rate space, as predicted by the
clustering model

9.5 Filling factor (ff) (or packing fraction) vs.
coordination number (n)

Tables

Chapter II

7.1 Calculation of the nonlinear polarization with all fields expressed in terms of the "natural" coordinates

Chapter III

9.1 Average number of dangling bonds per atom for small, tetrahedrally coordinated clusters

9.2 Relative volume change on melting

A2.1 Transformation matrices for first and second order twinning

A2.2 Cubic and tetrahedral directions after first and second order twinning

A3.1 Filling factors for simple crystal lattices

References

- Armstrong, J.A., Bloembergen, N., Ducuing, J. and Pershan, P.S.
Interactions between light waves in a nonlinear dielectric
Phys. Rev. 127, 1918 (1962)
- Baldwin, G.C.
An Introduction to Nonlinear Optics
Plenum, New York 1969
- Bloembergen, N.
Nonlinear Optics
Benjamin, Reading, MA 1965
- Bloembergen, N.
Apparatus for converting light energy from one frequency to another
U.S. Patent 3,384,433, May 21, 1968
- Bloembergen, N. and Sievers, A.J.
Nonlinear optical properties of periodic laminar structures
Appl. Phys. Lett. 17, 483 (1970)
- Dewey, Jr., C.F.
Nonlinear amplifying
U.S. Patent 3,988,593, October 26, (1976)
- Dewey, Jr., C.F. and Hocker, L.O.
Enhanced nonlinear optical effects in rotationally twinned crystals
Appl. Phys. Lett. 26, 442 (1975)
- Harper, P.G. and Wherrett, B.S., eds.
Nonlinear Optics
Acad. Press, London 1977
- Hocker, L.O. and Dewey, Jr., C.F.
Enhancement of second-harmonic generation in zinc selenide by crystal defects
Appl. Phys. Lett. 28, 267 (1976)
- McMullen, J.D.
Optical parametric interactions in isotropic materials using a phase-corrected stack of nonlinear dielectric plates
J. Appl. Phys. 46, 3076 (1975)
- Okada, M., Takizawa, K. and Ieiri, S.
Second harmonic generation by periodic laminar structure of nonlinear optical crystal
Opt. Comm. 18, 331 (1976)

Piltch, M.S., Cantrell, C.D. and Sze, R.C.
Infrared second-harmonic generation in nonbirefringent cadmium telluride
J. Appl. Phys. 47, 3514 (1976)

Rabin, H. and Tang, C.L., eds.
Quantum Electronics
Acad. Press, New York 1975

Shen, Y.-R.
Recent advances in nonlinear optics
Rev. Mod. Phys. 48, 1 (1976)

Shen, Y.-R., ed.
Nonlinear Infrared Generation
Springer-Verlag, Berlin 1977

Szilagyi, A. and Dewey, Jr., C.F.
Efficient infrared frequency doubling in rotationally twinned CdTe
in Proc. 2nd Int. Conf. on IR Physics, E. Affolter and F. Kneubuehl, eds., Zuerich 1979

Szilagyi, A., Hordvik, A. and Schlossberg, H.R.
A quasi-phase-matching technique for efficient optical mixing and frequency doubling
J. Appl. Phys. 47, 2025 (1976)

Szilagyi, A., Hordvik, A. and Schlossberg, H.R.
Apparatus for producing efficient second harmonic generation and frequency mixing
U.S. Patent 4,016,427, April 5, 1977

Tang, C.L. and Bey, P.P.
Phase-matching in second-harmonic generation using artificial periodic structures
J. Quant. Electr. QE-9, 9 (1973)

Thompson, D.E., McMullen, J.D. and Anderson, D.B.
Second harmonic generation in GaAs "stack of plates" using high power CO₂ laser radiation
Appl. Phys. Lett. 29, 113 (1976)

Yacoby, Y., Aggarwal, R.L. and Lax, B.
Phase matching by periodic variation of nonlinear coefficients
J. Appl. Phys. 44, 3181 (1973)

Zernike, F. and Midwinter, J.E.
Applied Nonlinear Optics
Wiley, New York 1973

CHAPTER II

Nonlinear Optics

II.1 Introduction

The enhancement of nonlinear optical processes by quasi-phase-matching (QPM) was first proposed in 1962 (Armstrong et al. 1962). Its implementation in rotationally twinned zincblende - type crystals forms the subject of this chapter.

The second-order nonlinear optical (NLO) phenomena of second harmonic generation (SHG), and sum and difference frequency generation (SFG and DFG), may be treated using Maxwell's classical equations of electrodynamics. In NLO materials, the constitutive relations supply a nonlinear polarization source term to the usual wave equation. After a number of approximations (see e.g. Byer and Herbst 1977; also Appendix A1) the wave equation for the electric field amplitude \vec{E}^3 radiated at frequency ω_3 is simplified to

$$\frac{\partial \vec{E}^3}{\partial r} = a \vec{P}^3 e^{i \Delta k r} \quad (1.1)$$

where a is given in Eq. (A1.12) and Δk is the wave vector mismatch. The phase - matching condition

$$\Delta k = 0 \quad (1.2)$$

results in monotonic change of the useful radiated field. In particular, appropriate initial conditions will cause \vec{E}^3 to increase continuously until complete or maximal conversion is achieved.

If $\Delta k \neq 0$, \vec{E}^3 changes sinusoidally with a half period (coherence length) l_c given by

$$\zeta_c = \frac{\pi}{|\Delta k|} \quad (1.3)$$

The QPM method (Armstrong et al. 1962) consists of using Eq. (1.1) only when \vec{E}^3 is on the increasing half of its period. Thus, ideally, just as the phase factor has changed sign (or $\Delta k r$ has reached the value π) one would like the polarization \vec{P}^3 to change sign as well, thereby restoring the growth ability of \vec{E}^3 .

The stack - of - plates method (Yacoby et al. 1973, McMullen 1975, Okada et al. 1976, Szilagyi et al. 1976 and 1977, Thompson et al. 1976, Piltch et al. 1976) uses the above prescription almost unaltered. But useful nonlinear effects do not always require the above conditions. As long as the rate of change of \vec{E}^3 is more often positive than negative, we can expect substantial growth over sufficiently large optical paths. Crystalline defects, naturally occurring in a random or quasi - periodic manner, can also produce an enhancement of the nonlinear optical properties. Among such defects, rotational twinning was first proposed by Dewey et al. (1975) and Hocker et al. (1976) and is now considered to hold great promise as a convenient frequency conversion tool (Dewey 1977 and Szilagyi et al. 1979).

The sign changes required by QPM are first treated quite generally in Section 2. Also independent of crystal class is a new form of the nonlinear susceptibility (Section 3) which enables a more systematic handling of transformations as well as of the subsequent development. In the $\bar{4}3m$ class the decomposition of the nonlinear polarization into invariant and

sign-changing components under the twinning operation is carried out both algebraically and trigonometrically (Sections 4 and 5, respectively). Frequency mixing in the same system is presented in Section 6. The treatment is expanded in Sections 7 and 8 to include doubling and mixing of general elliptically polarized beams. The cumulative effects due to twinning and to stacking of twinned plates are dealt with in Sections 9 and 10, respectively. The experimental verification of the SHG efficiency in an immersed stack of CdTe plates is described in Section 11. Among the conclusions of Section 12 is the necessity for an investigation of twinning as a growth process, with a view to its eventual utilization in the production of efficient nonlinear optical devices.

II.2 Sign changes in the nonlinear polarization

To simplify notation, we now drop the superscript identifying the frequency of the fields.

All of the original suggestions for sign reversal (e.g. Armstrong 1962) involved operations that reversed the sign of \vec{E} . They were based on the observation that

$$\vec{P} \cdot \vec{E} = \sum_{ijk=1}^3 d_{ijk} E_i E_j E_k \quad (2.1)$$

being cubic in the electric field, will necessarily also change sign.

While this suggestion did serve those configurations where the component of a SH polarization in the plane of incidence of a laser was of interest, it did not cover other components of \vec{P} , nor those mixing experiments where the fields are non-collinear. The need addressed in this section is to provide more general and systematic ways of effecting these desirable sign changes.

We begin by considering those transformations which reverse the orientation of a vector, and are also experimentally accessible. The surviving operations are only solid body rotations (since inversions and reflections cannot be physically carried out). The rotation angle is 180° about an arbitrary axis \hat{a} .

A vector \vec{A} can be decomposed in parallel (\vec{A}_{\parallel}) and normal (\vec{A}_{\perp}) components

$$\vec{A} = \vec{A}_{\parallel} + \vec{A}_{\perp} \quad (2.2)$$

such that

$$\begin{aligned}\vec{A}_{||} &\equiv \hat{a} A_{||} = \hat{a} (\vec{A} \cdot \hat{a}) \quad \text{and} \\ \vec{A}_{\perp} &= \hat{a} \times (\vec{A} \times \hat{a})\end{aligned}\quad (2.3)$$

After rotation, the perpendicular component changes sign

$$\vec{A}' \equiv \vec{A}'_{||} + \vec{A}'_{\perp} = \vec{A}_{||} - \vec{A}_{\perp}\quad (2.4)$$

It will be convenient to regard the nonlinear polarization \vec{P} as a bilinear form

$$\vec{P}(\vec{A}, \vec{B}) \equiv \sum_{mpq=1}^3 \hat{i}_m d_{mpq} (\vec{A} \cdot \hat{i}_p) (\vec{B} \cdot \hat{i}_q)\quad (2.5)$$

where \hat{i}_p are the unit coordinate vectors. Then for second harmonic generation (SHG)

$$\vec{P} \equiv \vec{P}(\vec{E}) \equiv \vec{P}(\vec{E}, \vec{E})\quad (2.6a)$$

and for SFG (with obvious extension for DFG) of fields \vec{E} and

$$\vec{H} \quad \vec{P} \equiv \vec{P}(\vec{E}, \vec{H}) + \vec{P}(\vec{H}, \vec{E})\quad (2.6b)$$

For definiteness we specialize to the SHG case. The application to mixing will be readily apparent in the development which follows.

Proceeding as in Eqs. (2.2) - (2.4) we separate \vec{P} in components:

$$\vec{P} = \vec{P}_{||}(\vec{E}_{||} + \vec{E}_{\perp}) + \vec{P}_{\perp}(\vec{E}_{||} + \vec{E}_{\perp})\quad (2.7)$$

The polarization \vec{P}' after the crystal rotation, can be expressed in terms of quantities pertaining to the unrotated, or laboratory, frame as

$$\vec{P}' = \vec{P}_{||}(\vec{E}_{||} - \vec{E}_{\perp}) - \vec{P}_{\perp}(\vec{E}_{||} - \vec{E}_{\perp})\quad (2.8)$$

Using the bilinearity of \vec{P} as expressed in Eqs. (2.5) and (2.6a) it is clear that \vec{P} may be written as a sum of an

invariant term \vec{P}_+ and a term \vec{P}_- which changes sign under the 180° rotation:

$$\vec{P} = \vec{P}_+ + \vec{P}_- \quad (2.9a)$$

$$\vec{P}' = \vec{P}_+ - \vec{P}_- = -\vec{P} + 2\vec{P}_+ \quad (2.9b)$$

where

$$\vec{P}_+ \equiv \vec{P}_{||}(\vec{E}_{||}) + \vec{P}_{||}(\vec{E}_{\perp}) + 2\vec{P}_{\perp}(\vec{E}_{||}, \vec{E}_{\perp}) \quad (2.10a)$$

$$\vec{P}_- \equiv \vec{P}_{\perp}(\vec{E}_{||}) + \vec{P}_{\perp}(\vec{E}_{\perp}) + 2\vec{P}_{||}(\vec{E}_{||}, \vec{E}_{\perp}) \quad (2.10b)$$

Note here that we have chosen to simplify the notation by assuming a susceptibility tensor symmetric in the last two indices. This in no way restricts the generality of the method, which could just as easily be carried out retaining both permutations of $(\vec{E}_{||}, \vec{E}_{\perp})$ instead of the factors of 2 in Eqs. (2.10).

A more detailed evaluation can be carried out for \vec{P}_+ by using definition (2.3a) and bilinearity, and expressing a perpendicular component in terms of the full, unrotated field less its (invariant) component along \hat{a} .

$$\begin{aligned} \vec{P}_+ = & \hat{a}(\hat{a} \cdot \vec{P}) + 2(\hat{a} \cdot \vec{E}) \left[\vec{P}(\hat{a}, \vec{E}) - 2\hat{a} \hat{a} \cdot \vec{P}(\hat{a}, \vec{E}) \right] - \\ & - 2(\hat{a} \cdot \vec{E}) \left[\vec{P}(\hat{a}) - 2\hat{a} \hat{a} \cdot \vec{P}(\hat{a}) \right] \end{aligned} \quad (2.11)$$

\vec{P}_- can be evaluated in the simplest way by combining Eqs. (2.9a) and (2.11) and solving for \vec{P}_- .

We are now in a position to state under what conditions the component of \vec{P} along an arbitrary unit vector \hat{A} (fixed in the laboratory frame) will change sign after the crystal rotation:

$$\begin{aligned} \hat{A} \cdot \vec{P}' = & -\hat{A} \cdot \vec{P} + 2 \{ (\hat{A} \cdot \hat{a})(\hat{a} \cdot \vec{P}) + 2(\hat{a} \cdot \vec{E})[\hat{A} \cdot \vec{P}(\hat{a}, \vec{E})] - \\ & - 2(\hat{A} \cdot \hat{a}) \hat{a} \cdot \vec{P}(\hat{a}, \vec{E}) \} - \\ & - 2(\hat{a} \cdot \vec{E})[\hat{A} \cdot \vec{P}(\hat{a}) - 2(\hat{A} \cdot \hat{a}) \hat{a} \cdot \vec{P}(\hat{a})] \} \end{aligned} \quad (2.12)$$

The primary result of Eq. (2.12), namely that for \vec{E} fields in the plane normal to the rotation axis, the \vec{P} component in that plane changes sign, could also have been obtained directly from the definition of \vec{P} and parity considerations. But Eq. (2.12) and indeed, the development of this entire section retain far more generality. Not only are we not limited by a geometrical configuration, but the crystal class itself remains unspecified. As mentioned above, mixing could be accommodated with equal facility. Moreover, the same method could be used to treat nonlinear polarizations of any order (e.g. in the n^{th} order we would handle a n -linear form, the rest of the argument obtaining identically).

Applications of the above results exist in a number of areas even before further development. For example, in the stack-of-plates method of QPM using Brewster angle incidence, it is the component of \vec{P} in the plane of incidence that is of interest ($\hat{A} = \hat{E}$). The only \hat{a} which is perpendicular to \vec{E} and maintains the plates at the Brewster angle, is perpendicular to the plane of incidence.

A second example is at the heart of this thesis. Rotational twinning such as occurs in zincblende type crystals is equivalent to a 180° rotation of the crystal lattice on opposite sides of a $\{111\}$ composition plane. It is easy to see that for propagation in a direction normal to the twin

plane, the component of \vec{P} parallel to such planes will change sign from domain to domain.

II.3 The new form of $\chi^{(2)}$

There is one more result to be derived before specializing to our crystal class.

For SHG purposes the nonlinear polarization \vec{P} is customarily written in the Miller notation:

$$\begin{pmatrix} P_1 \\ P_2 \\ P_3 \end{pmatrix} = \begin{pmatrix} d_{11} & d_{12} & d_{13} & d_{14} & d_{15} & d_{16} \\ d_{21} & d_{22} & d_{23} & d_{24} & d_{25} & d_{26} \\ d_{31} & d_{32} & d_{33} & d_{34} & d_{35} & d_{36} \end{pmatrix} \begin{pmatrix} E_1^2 \\ E_2^2 \\ E_3^2 \\ 2E_2E_3 \\ 2E_3E_1 \\ 2E_1E_2 \end{pmatrix} \quad (3.1)$$

This formulation takes advantage of the symmetry $d_{ijk} = d_{ikj}$ (for SHG). This form is convenient for listing the relevant non-vanishing coefficients in the various crystal classes. we have found that for certain computational purposes and for the physical intuition Eq. (3.1) may be cast into a more convenient form:

$$P_j = (E_1, E_2, E_3) \begin{pmatrix} d_{j1} & d_{j6} & d_{j5} \\ d_{j6} & d_{j2} & d_{j4} \\ d_{j5} & d_{j4} & d_{j3} \end{pmatrix} \begin{pmatrix} E_1 \\ E_2 \\ E_3 \end{pmatrix} \quad (3.2a)$$

$$\equiv E^t D^j E \quad (3.2b)$$

Thus we can avail ourselves of the well developed theory of quadratic forms (or bilinear forms for SFG or DFG). For

example we may want to maximize the component of \vec{P} along some vector \vec{A} . We write

$$\vec{P} \cdot \vec{A} = \mathbf{E}^t (\vec{A} \cdot \vec{D}) \mathbf{E} = \mathbf{E}^t \left(\sum_j A_j \mathbf{D}^j \right) \mathbf{E} \quad (3.3)$$

where \mathbf{D} is a matrix-vector (i.e. a vector whose three components are each 3X3 matrices). This reduces to the standard problem of maximizing a quadratic form, or diagonalizing a 3X3 matrix. Eqs. (3.2a,b) are also very useful when we need to investigate the rotational properties of \vec{P} (which are by no means clear in the form of the 3*6 and 6*1 matrices of Eq. (3.1)). Thus the operation of rotation of the crystal with respect to a lab frame is written as the transformation of the crystal axes \hat{i}_j :

$$\hat{i}'_j = \sum_k R_{jk} \hat{i}_k \quad (3.4)$$

so that the \vec{E} field components transform like

$$E'_j \equiv \vec{E} \cdot \hat{i}'_j \quad (3.5)$$

$$= \sum_k R_{jk} E_k \quad (3.6)$$

where R_{jk} is a three dimensional rotation matrix.

The polarization \vec{P} in the rotated system is

$$\vec{P}' = (E'_1, E'_2, E'_3) \left[\sum_{j'} \hat{i}'_{j'} \mathbf{D}^{j'} \right] \begin{pmatrix} E'_1 \\ E'_2 \\ E'_3 \end{pmatrix} \quad (3.7a)$$

$$= \sum_{j'} \hat{i}'_{j'} \sum_{nm} \mathbf{D}^{j'}_{kl} E'_m E'_n \quad (3.7b)$$

Or, in terms of the unrotated (lab) frame

$$\vec{P} = \sum_j \hat{i}_j \sum_{kl} (D')_{kl}^j E_k E_l \quad (3.8)$$

where

$$(D')_{kl}^j = \sum_{j'mn} D_{mn}^{j'} R_{j'j} R_{mj} R_{nl} \quad (3.9)$$

Eq. (3.9) plus the definition of Eq. (3.2b) give us the transformation properties of the nonlinear coefficients in the Miller notation under rotation of the crystal axes.

For the present investigation, the important crystal class is $\bar{4}3m$. Here the matrix-vector \vec{D} is

$$\vec{D} = d_{14} \begin{pmatrix} 0 & \hat{i}_3 & \hat{i}_2 \\ \hat{i}_3 & 0 & \hat{i}_1 \\ \hat{i}_2 & \hat{i}_1 & 0 \end{pmatrix} \quad (3.10)$$

For ready reference we list \vec{D} corresponding to the various crystal classes in Appendix II.A2.

As we shall see in the next section, Eq. (3.10) and the results of section II.2 are very advantageous tools for the detailed evaluation of the nonlinear polarization.

II.4 Algebraic decomposition of \vec{P} in the $\bar{4}3m$ class

According to the results of Eqs. (2.9b) and (2.10a) we need to evaluate

$$\vec{P}_+ = \vec{P}_{||}(\vec{E}_{||}) + \vec{P}_{||}(\vec{E}_{\perp}) + 2\vec{P}_{\perp}(\vec{E}_{||}, \vec{E}_{\perp}) \quad (4.1)$$

As mentioned above, in the sphalerite or $\bar{4}3m$ crystal class twinning takes place with an effective rotation axis

$$\hat{a} = \frac{1}{\sqrt{3}} (1, 1, 1) \quad (4.2)$$

Recalling the decomposition of Eqs. (2.2) and (2.3) we write the unit coordinate vectors \hat{i}_j as

$$\hat{i}_j = \frac{1}{\sqrt{3}} \hat{a} + \sqrt{\frac{2}{3}} \hat{v}_j \quad (4.3)$$

where

$$\hat{v}_j = \frac{1}{\sqrt{6}} [3\hat{i}_j - (1, 1, 1)] = \sqrt{\frac{3}{2}} \hat{a} \times (\hat{i}_j \times \hat{a}) \quad (4.4)$$

(e.g. $\hat{v}_1 = \frac{1}{\sqrt{6}} (2, -1, -1)$ etc.).

We refer to \hat{v}_j as the "three-fold" vectors.

Also by way of definition we now distinguish between two kinds of vectors: the physical ones, pointing in definite directions in real space, and the abstract (contravariant) ones which are sets of components constituted in row or column matrices for the purpose of matrix multiplication. For an observer rotating with the crystal, a contravariant vector describes the apparent position of an object fixed in the laboratory coordinates. The abstract vectors are denoted by special bold face symbols as in the following example:

$$\vec{E} = \sum E_j \hat{i}_j = \mathbb{E}^t \begin{pmatrix} \hat{i}_1 \\ \hat{i}_2 \\ \hat{i}_3 \end{pmatrix} \quad (4.5)$$

Rotating the crystal axes by means of the operator R as in Eq. (3.4), changes the \vec{E} field components according to Eq. (3.6). Then Eq. (4.5) becomes

$$\vec{E}' = \mathbb{E}^t R^t R \begin{pmatrix} \hat{i}_1 \\ \hat{i}_2 \\ \hat{i}_3 \end{pmatrix} = \vec{E} \quad (4.6)$$

That \vec{E} is invariant when the crystal is rotated should be expected since \vec{E} is fixed in the lab. Its components however transform as shown.

With these preliminaries out of the way, we proceed to decompose \vec{E} and \vec{D} into components parallel and perpendicular to \hat{a} :

$$\mathbb{E} = E_{||} \hat{a} + \sqrt{\frac{2}{3}} \sum_j E_j \hat{v}_j \equiv \mathbb{E}_{||} + \mathbb{E}_{\perp} \quad (4.7)$$

$$\frac{\vec{D}}{d_{14}} = \begin{pmatrix} 0 & \hat{i}_3 & \hat{i}_2 \\ \hat{i}_3 & 0 & \hat{i}_1 \\ \hat{i}_2 & \hat{i}_1 & 0 \end{pmatrix} = \frac{1}{\sqrt{3}} \hat{a} \begin{pmatrix} 0 & 1 & 1 \\ 1 & 0 & 1 \\ 1 & 1 & 0 \end{pmatrix} + \sqrt{\frac{2}{3}} \begin{pmatrix} 0 & \hat{v}_3 & \hat{v}_2 \\ \hat{v}_3 & 0 & \hat{v}_1 \\ \hat{v}_2 & \hat{v}_1 & 0 \end{pmatrix} \quad (4.8a)$$

$$\equiv \frac{\vec{D}_{||}}{d_{14}} + \frac{\vec{D}_{\perp}}{d_{14}} \quad (4.8b)$$

$$\equiv \vec{d}_{||} + \vec{d}_{\perp} \equiv \vec{d} \quad (4.8c)$$

Similarly we define a lower case polarization \vec{p} by

$$\vec{p} \equiv \frac{\vec{P}}{d_{14}} = \mathbb{E}^t \vec{d} \mathbb{E} \quad (4.9)$$

We have found that subsequent calculations are significantly eased by introducing a compact notation for the susceptibility tensor d_{ij} . We do this by subtracting the

quantity

$$\sum_{j=1}^3 \hat{\vartheta}_j = 0 \quad (4.10)$$

from each matrix element of \vec{d}_{\perp} :

$$\vec{d}_{ij} = \left[\frac{1}{\sqrt{3}} \hat{a} - \sqrt{\frac{2}{3}} (\hat{\vartheta}_i + \hat{\vartheta}_j) \right] (1 - \delta_{ij}) \quad (4.11a)$$

$$(\vec{d}_{\parallel})_{ij} = \frac{1}{\sqrt{3}} \hat{a} (1 - \delta_{ij}) \quad (4.11b)$$

$$(\vec{d}_{\perp})_{ij} = -\sqrt{\frac{2}{3}} (\hat{\vartheta}_i + \hat{\vartheta}_j) (1 - \delta_{ij}) \quad (4.11c)$$

It is convenient to examine the effect of sandwiching each of the two orthogonal components of \vec{d} between two arbitrary vectors \vec{A} and \vec{B} :

$$\vec{A} \vec{d}_{\parallel} \vec{B} = \frac{1}{\sqrt{3}} \hat{a} (3A_{\parallel} B_{\parallel} - \vec{A} \cdot \vec{B}) = \vec{P}_{\parallel}(\vec{A}, \vec{B}) \quad (4.12a)$$

$$\begin{aligned} \vec{A} \vec{d}_{\perp} \vec{B} &= -\sqrt{3} (A_{\parallel} \vec{B}_{\perp} + B_{\parallel} \vec{A}_{\perp}) + 2\sqrt{\frac{2}{3}} \sum_j A_j B_j \hat{\vartheta}_j \\ &= \vec{P}_{\perp}(\vec{A}, \vec{B}) \end{aligned} \quad (4.12b)$$

In this last equation we have used the form of the perpendicular component of a vector given in Eq. (4.7).

Simpler forms are obtained in a few instances when one of the vectors has only a parallel or only a perpendicular component to \hat{a} :

$$\vec{P}_{\parallel}(\vec{A}_{\parallel}, \vec{B}) = \frac{2}{\sqrt{3}} \hat{a} A_{\parallel} B_{\parallel} = \vec{P}_{\parallel}(\vec{A}_{\parallel}, \vec{B}_{\parallel}) \quad (4.13a)$$

$$\vec{P}_{\parallel}(\vec{A}_{\perp}, \vec{B}) = -\frac{1}{\sqrt{3}} \hat{a} \vec{A}_{\perp} \cdot \vec{B}_{\perp} = \vec{P}_{\parallel}(\vec{A}_{\perp}, \vec{B}_{\perp}) \quad (4.13b)$$

$$\vec{P}_{||}(\vec{A}_{||}, \vec{B}_{\perp}) = 0 \quad (4.13c)$$

$$\vec{P}_{\perp}(\vec{A}_{||}, \vec{B}) = -\frac{1}{\sqrt{3}} A_{||} \vec{B}_{\perp} = \vec{P}_{\perp}(\vec{A}_{||}, \vec{B}_{\perp}) \quad (4.13d)$$

$$\vec{P}_{\perp}(\vec{A}_{||}, \vec{B}_{||}) = 0 \quad (4.13e)$$

With these results, evaluation of Eqs. (2.10a and b) no longer presents any problem. The former is

$$\begin{aligned} \vec{P}_{+} &= \frac{2}{\sqrt{3}} \hat{a} E_{||}^2 - \frac{1}{\sqrt{3}} \hat{a} E_{\perp}^2 - \frac{2}{\sqrt{3}} E_{||} \vec{E}_{\perp} \\ &= \frac{1}{\sqrt{3}} \hat{a} (3 E_{||}^2 - E^2) - \frac{2}{\sqrt{3}} E_{||} \vec{E}_{\perp} \end{aligned} \quad (4.14)$$

while the latter becomes

$$\begin{aligned} \vec{P}_{-} &= \vec{P}_{\perp}(\vec{E}_{\perp}) \\ &= \vec{P}_{\perp}(\vec{E}) + \vec{P}_{\perp}(\vec{E}_{||}) - 2 \vec{P}_{\perp}(\vec{E}_{||}, \vec{E}) \\ &= \vec{P}_{\perp}(\vec{E}) - 2 \vec{P}_{\perp}(\vec{E}_{||}, \vec{E}_{\perp}) \end{aligned} \quad (4.15a)$$

Using Eq. (4.12b)

$$\begin{aligned} \vec{P}_{-} &= -2\sqrt{3} E_{||} \vec{E}_{\perp} + 2\sqrt{\frac{2}{3}} \sum_j E_j^2 \hat{U}_j + \frac{2}{\sqrt{3}} E_{||} \vec{E}_{\perp} \\ &= 2\sqrt{\frac{2}{3}} \sum_{j=1}^3 E_j (E_j - \frac{2}{\sqrt{3}} E_{||}) \hat{U}_j \end{aligned} \quad (4.15b)$$

The quantity in parantheses will be recognized as the negative of the \vec{E} field component in the rotated crystal coordinates:

$$E_j' = \hat{U}_j \cdot (-\vec{E} + 2 E_{||} \hat{a})$$

so that

$$\vec{P}_{-} = -2\sqrt{\frac{2}{3}} \sum_{j=1}^3 E_j E_j' \hat{U}_j \quad (4.16)$$

Since $E_j E_j'$ is obviously invariant under the 180° rotation,

while \hat{v}_j changes sign when viewed from the lab frame, \vec{p}_- has now come to deserve its label as the sign changing part of the nonlinear polarization.

To sum up

$$\begin{aligned} \vec{p} &= \vec{p}_+ + \vec{p}_- \\ &= \frac{2}{\sqrt{3}} \left[\left(\frac{3E_{\parallel}^2 - E^2}{2} \right) \hat{a} - E_{\parallel} \vec{E}_{\perp} \right] - 2\sqrt{\frac{2}{3}} \sum_{j=1}^3 E_j \cdot E_j' \hat{U}_j \end{aligned} \quad (4.17)$$

II.5 Trigonometric evaluation for SHG

We will base the calculation of the nonlinear polarization on the geometrical configuration of Fig. 5.1 . The orientation of the unit internal electric field vector can accordingly be written

$$\hat{E} = \frac{1}{\sqrt{3}}(111)\cos\eta + \hat{u}(\varphi)\sin\eta = \frac{\vec{E}_{\parallel} + \vec{E}_{\perp}}{|\vec{E}|} \quad (5.1a)$$

where

$$\hat{u}(\varphi) = \frac{1}{\sqrt{6}}(2, -1, -1)\cos\varphi + \frac{1}{\sqrt{2}}(0, 1, -1)\sin\varphi \quad (5.1b)$$

If we define φ_j as the azimuthal angles of the coordinate axes when viewed from a system with \hat{a} as the polar axis, we also have

$$\hat{u}(\varphi) = \sqrt{\frac{2}{3}} \sum_j \hat{j} \cos(\varphi - \varphi_j) \quad (5.1c)$$

where

$$\varphi_j = (j-1) \frac{2\pi}{3}$$

such that

$$\hat{u}(\beta) \cdot \hat{u}(\gamma) = \cos(\beta - \gamma)$$

Substitution into Eq. (4.16) immediately results in

$$\vec{P}_+ = \frac{1}{\sqrt{3}} E^2 \left[(3\cos^2\eta - 1)\hat{a} - 2\sin\eta\cos\eta \hat{u}(\varphi) \right] \quad (5.2)$$

Evaluation of $\vec{P}_- = -2\sqrt{\frac{2}{3}} \sum_j E_j E'_j \hat{u}_j$ (Eq. (4.16)) is more difficult.

From Eq. (5.1a), we express E_j and E'_j as

$$E'_j = \frac{1}{\sqrt{3}} \cos\eta + \hat{j} \cdot \hat{u}(\varphi) \sin\eta \quad (5.3a)$$

$$\hat{E}'_j = \frac{1}{\sqrt{3}} \cos \eta - \hat{j} \cdot \hat{u}(\varphi) \sin \eta \quad (5.3b)$$

while

$$\hat{O}_j = \frac{1}{\sqrt{6}} [3\hat{j} - (1,1,1)] \quad (5.4)$$

Substitute in Eq. (4.16) and collect terms

$$\begin{aligned} \vec{P} &= -\frac{2}{\sqrt{3}} E^2 \sin^2 \eta \left\{ \hat{a} - \sqrt{3} \sum_{j=1}^3 \hat{j} [\hat{j} \cdot \hat{u}(\varphi)]^2 \right\} \\ &= \frac{4}{3} E^2 \sin^2 \eta \sum_j \hat{j} \frac{1}{2} [3(\hat{j} \cdot \hat{u})^2 - 1] \end{aligned} \quad (5.5a)$$

$$= \frac{4}{3} E^2 \sin^2 \eta \sum_j \hat{j} P_2(\cos \tau_j) \quad (5.5b)$$

where $P_2(\cos \tau) = \frac{1}{2}(3\cos^2 \tau - 1)$ is a Legendre polynomial and τ_j are the angles between \hat{u} and the unit vectors \hat{j} .

Let us now use the addition theorem for the associated Legendre polynomials P_l^m (see e.g. Schiff 1968, p. 258):

$$\begin{aligned} P_l(\cos \theta) &= P_l(\cos \theta_1) P_l(\cos \theta_2) + \\ &+ 2 \sum_{m=1}^l \frac{(l-m)!}{(l+m)!} P_l^m(\cos \theta_1) P_l^m(\cos \theta_2) \cos m(\varphi_1 - \varphi_2) \end{aligned}$$

Here θ_i, φ_i are the polar coordinates of the two unit vectors whose scalar product is $\cos \theta$. In our case, using

\hat{a} as \hat{z} axis

$$\begin{aligned} P_2(\cos \tau_j) &= P_2\left(\frac{1}{\sqrt{3}}\right) P_2(0) + 2 \left[\frac{(2-1)!}{(2+1)!} P_2^1\left(\frac{1}{\sqrt{3}}\right) P_2^1(0) \cos(\varphi_j - \varphi) + \right. \\ &\quad \left. + \frac{(2-2)!}{(2+2)!} P_2^2\left(\frac{1}{\sqrt{3}}\right) P_2^2(0) \cos 2(\varphi_j - \varphi) \right] \end{aligned} \quad (5.6)$$

With Schiff's definitions (p. 79-80, op. cit.) we have

$$P_2^1 = 3\sqrt{(1-\cos^2 \theta)} \cos \theta \quad ; \quad P_2^2 = 3(1-\cos^2 \theta)$$

so that $P_2\left(\frac{1}{\sqrt{3}}\right) = 0 = P_2^1(0)$ and the only surviving term in

Eq. (5.6) is the last one:

$$P_2(\cos \tau_j) = \frac{2}{4!} \cdot 2 \cdot 3 \cdot \cos 2(\varphi_j - \varphi) = \frac{1}{2} \cos(2\varphi_j - 2\varphi) \quad (5.7)$$

With this result Eq. (5.5b) begins to look more manageable:

$$\vec{P}_- = \frac{2}{3} E^2 \sin \eta \sum_j \hat{j} \cos(2\varphi_j - 2\varphi) \quad (5.8)$$

But

$$\begin{aligned} \cos(2\varphi_j - 2\varphi) &= \cos(3\varphi_j - \varphi_j - 2\varphi) \\ &= \cos(-2\varphi - 2\varphi_j) \end{aligned}$$

since

$$3\varphi_j = (j-1)2\pi$$

Recalling expression (5.1c) for $U(\varphi)$, we finally obtain

$$\vec{P}_- = \sqrt{\frac{2}{3}} E^2 \sin^2 \eta \hat{U}(-2\varphi) \quad (5.9)$$

We record here the combined form of Eqs. (5.2 and 5.9):

$$\vec{P} = \frac{2}{\sqrt{3}} E^2 \left\{ \left[P_2^0(\cos \eta) - \frac{1}{3} P_2^1(\cos \eta) \hat{U}(\varphi) \right] + \frac{1}{3\sqrt{2}} P_2^2(\cos \eta) \hat{U}(-2\varphi) \right\} \quad (5.10a)$$

$$= \frac{1}{\sqrt{3}} E^2 \left[(3\cos^2 \eta - 1) \hat{a} - 2 \sin \eta \cos \eta \hat{U}(\varphi) + \sqrt{2} \sin^2 \eta \hat{U}(-2\varphi) \right] \quad (5.10b)$$

The reason we were able to express \vec{P} in terms of the associated Legendre functions is that the latter (actually the closely related spherical harmonics Y_1^m) are basis functions for an irreducible representation of the rotation group. The $l = 2$ value is a direct consequence of the presence of two powers of the electric field. The discussion for higher

orders of nonlinearity proceeds along the same lines.

In hindsight, a change of coordinate system

$$\begin{aligned}\hat{z} &= \frac{1}{\sqrt{3}}(1, 1, 1) \\ \hat{x} &= \frac{1}{\sqrt{6}}(2, -1, -1) \\ \hat{y} &= \frac{1}{\sqrt{2}}(0, 1, -1)\end{aligned}\tag{5.11a}$$

or

$$\begin{pmatrix} \hat{x} \\ \hat{y} \\ \hat{z} \end{pmatrix} = \begin{pmatrix} \sqrt{\frac{2}{3}} & -\sqrt{\frac{1}{6}} & -\sqrt{\frac{1}{6}} \\ 0 & \sqrt{\frac{1}{2}} & -\sqrt{\frac{1}{2}} \\ \sqrt{\frac{1}{3}} & \sqrt{\frac{1}{3}} & \sqrt{\frac{1}{3}} \end{pmatrix} \begin{pmatrix} \hat{c} \\ \hat{j} \\ \hat{k} \end{pmatrix}\tag{5.11b}$$

would have straightforwardly lead to the same result. For variety we now display it in two different ways:

$$\vec{P} = \frac{1}{\sqrt{3}} \left\{ (3E_z^2 - E^2) \hat{z} - 2E_z(E_x \hat{x} + E_y \hat{y}) + \sqrt{2} [\hat{x}(E_x^2 - E_y^2) - 2\hat{y} E_x E_y] \right\}\tag{5.12a}$$

$$= \frac{1}{\sqrt{3}} E^2 \sqrt{\frac{16\pi}{5}} \left[\hat{z} Y_2^0 - \frac{1}{\sqrt{3}} (\hat{\epsilon}_+ Y_2^{-1} - \hat{\epsilon}_- Y_2^1) + \sqrt{\frac{2}{3}} (\hat{\epsilon}_+ Y_2^2 + \hat{\epsilon}_- Y_2^{-2}) \right]\tag{5.12b}$$

The spherical harmonics Y_l^m in Eq. (5.12b) are defined to

be

$$\begin{aligned}Y_2^0 &= \sqrt{\frac{5}{16\pi}} (3 \cos^2 \eta - 1) \\ Y_2^{\pm 1} &= \mp \sqrt{\frac{15}{8\pi}} \sin \eta \cos \eta e^{\pm i\varphi} \\ Y_2^{\pm 2} &= \sqrt{\frac{15}{32\pi}} \sin^2 \eta e^{\pm 2i\varphi}\end{aligned}\tag{5.13}$$

while the circular polarization unit vectors $\hat{\epsilon}_{\pm}$ are

$$\hat{\mathbf{E}}_{\pm} = \frac{1}{\sqrt{2}} (\hat{x} \pm i\hat{y}) \quad (5.14)$$

An interesting feature of our result (5.10) is that rotating the crystal around the three-fold axis $\hat{\mathbf{a}}$ while keeping $\vec{\mathbf{E}}$ fixed in the lab gives the nonlinear polarization $\vec{\mathbf{p}}$ two counter-rotating components (ignoring the constant along $\hat{\mathbf{a}}$ itself). One of the components is locked in angular phase with the fundamental, while the other counter-rotates at twice the rate with respect to the crystal or three times as fast with respect to the lab. We see that a $\pi/3$ crystal rotation turns the latter component by π with respect to its initial lab position. For (1,1,1) propagation ($\cos \eta = 0$) the only radiating component is this term which will change sign across the twin boundary, as required for quasi-phase-matching.

Equation (5.10) also shows that the magnitude of the radiating polarization is independent of the angle φ when propagation is along the three-fold axis ($\mathbf{E} \perp \hat{\mathbf{a}}$) and it is given by

$$|\vec{\mathbf{p}}_{\perp}| = \sqrt{\frac{2}{3}} E^2 \quad (\cos \eta = 0) \quad (5.15)$$

The magnitude of the total polarization is readily obtained from Eq. (5.10)

$$|\vec{\mathbf{p}}| = \frac{2}{\sqrt{3}} E^2 \left[(P_2^0)^2 + \frac{1}{9} (P_2^1)^2 + \frac{1}{18} (P_2^2)^2 - \frac{2}{9\sqrt{2}} P_2^1 P_2^2 \cos 3\varphi \right]^{1/2} \quad (5.16)$$

For (1,1,1) propagation this becomes

$$|\vec{\mathbf{p}}| = E^2 \quad (\cos \eta = 0) \quad (5.17)$$

From Eqs. (5.10b), (5.15) and (5.17) it is clear that the polarization revolves on a conic surface coaxial with $(-\hat{a})$ with a cone half-angle θ of

$$\theta = \arcsin \sqrt{\frac{2}{3}} \approx 54.7^\circ \quad (\cos \eta = 0) \quad (5.18)$$

and which contains the three $(-1, 0, 0)$ type axes. In fact, the simplified expression

$$\vec{p} = E^2 \left[-\frac{1}{\sqrt{3}} \hat{a} + \sqrt{\frac{2}{3}} \hat{u}(-2\varphi) \right] \quad (5.19)$$

shows that

$$\vec{p}(\varphi = \frac{\pi}{2} + \varphi_j) = -E^2 \hat{c}_j \quad (5.20)$$

and

$$\vec{p} \cdot \hat{u}(\varphi_0) = \vec{p}_\perp \cdot \hat{u}(\varphi_0) = 0 \quad \text{whenever} \quad \cos 3\varphi_0 = 0 \quad (5.21)$$

or

$$\varphi_0 = \pm \frac{\pi}{2} + \varphi_j$$

Thus, whenever E is along one of the six $(0, 1, -1)$ type axes normal to \hat{a} , the radiated field will be normal to the plane of incidence, and could then be efficiently filtered out using a Brewster angle window.

Similarly, Eq. (5.19) shows that the radiated field

would be in the plane of incidence whenever $\varphi = \varphi_j$, i.e.
when \vec{E} is aligned with one of the six $(2,-1,-1)$ type axes
normal to \hat{a} .

II.6 Frequency mixing

Assuming for simplicity that the symmetry of the second harmonic susceptibility tensor is retained by a second order mixing process, the nonlinear polarization at the mixed (output) frequency \vec{p}^M is

$$\vec{p}^M = \vec{p}(\vec{E}, \vec{H}) + \vec{p}(\vec{H}, \vec{E}) = 2\vec{p}(\vec{E}, \vec{H}) \quad (6.1)$$

Equations (4.12) and (4.13) come in handy again and with no further complications we obtain

$$\frac{1}{2}\vec{p}_+^M = \frac{2}{\sqrt{3}} \left[\left(\frac{3E_{||}H_{||} - \vec{E} \cdot \vec{H}}{2} \right) \hat{a} - \left(\frac{E_{||}H_{\perp} + H_{||}E_{\perp}}{2} \right) \right] \quad (6.2a)$$

$$\frac{1}{2}\vec{p}_-^M = \vec{p}_{\perp}(\vec{E}_{\perp}, \vec{H}_{\perp}) = -\sqrt{\frac{2}{3}} \sum_j (H_j E_j' + E_j H_j') \hat{U}_j \quad (6.2b)$$

Defining ν and ψ as the polar and the azimuthal angles of \vec{H} in the manner of Eqs. (5.1) we also readily arrive at the trigonometric form of \vec{p}_+^M :

$$\frac{1}{2}\vec{p}_+^M = \frac{1}{\sqrt{3}}EH \left\{ \left[3\cos\eta \cos\nu - (\cos\eta \cos\nu + \sin\eta \sin\nu \cos(\varphi - \psi)) \right] \hat{a} - \left[\cos\eta \sin\nu \hat{U}(\psi) + \cos\nu \sin\eta \hat{U}(\varphi) \right] \right\} \quad (6.3)$$

To calculate \vec{p}_-^M we will use a different, more direct method than that of Section II.5. We substitute

$$\left(\hat{E}_{\perp} \right)_i = \left[\hat{e}_i \cdot \hat{U}(\varphi) \right] \sin\eta = \sqrt{\frac{2}{3}} \sin\eta \cos(\varphi - \varphi_i) \quad (6.4a)$$

and

$$\left(\hat{H}_{\perp} \right)_j = \sqrt{\frac{2}{3}} \sin\nu \cos(\psi - \varphi_j) \quad (6.4b)$$

in the expression for $\vec{p}_{\perp}(\vec{E}_{\perp}, \vec{H}_{\perp})$ arising from Eq. (4.11c)

$$\frac{1}{2} \vec{P}^M = - \left(\frac{\sqrt{2}}{3} \right)^2 \frac{2}{3} E H \sin \eta \sin \nu \sum_{ij} \cos(\varphi - \varphi_j) (\hat{U}_i + \hat{U}_j) (1 - \delta_{ij}) \cos(\psi - \varphi) \quad (6.5)$$

The term multiplying the "1" of $(1 - \delta_{ij})$ gives a null result since it is proportional to

$$\sum_j \cos(\varphi - \varphi_j) \sim \hat{a} \cdot \hat{a} = 0$$

The remaining term is

$$\frac{1}{2} \vec{P}^M = 2 \sqrt{\frac{2}{3}} \frac{2}{3} E H \sin \eta \sin \nu \sum_j \cos(\varphi - \varphi_j) \cos(\psi - \varphi_j) \hat{U}_j$$

Write the product of cosines as

$$\frac{1}{2} [\cos(\varphi + \psi - 2\varphi_j) + \cos(\varphi - \psi)]$$

and notice that the second term will multiply something proportional to

$$\sum_j \hat{U}_j = 0$$

leaving only

$$\sum_j \frac{1}{2} \cos(\varphi + \psi + \varphi_j - 3\varphi_j) \hat{U}_j = \sum_j \frac{1}{2} \cos(\varphi + \psi + \varphi_j) \hat{U}_j$$

inside the summation. Now

$$\frac{1}{2} \vec{P}^M = \frac{2}{3} E H \sin \eta \sin \nu \sum_j \left\{ \sqrt{\frac{2}{3}} \cos[-(\varphi - \psi) - \varphi_j] \right\} \hat{U}_j$$

But according to Eq. (4.7) the summation is $\sqrt{(3/2)}$ times the perpendicular part of a vector whose components are

$$\sqrt{\frac{2}{3}} \cos[-(\varphi + \psi) - \varphi_j]$$

This is none other than $\hat{a}(-\varphi - \psi)$ (see Eq. 5.1c), i.e.

$$\frac{1}{2} \vec{P}^M = \frac{2}{3} E H \sin \eta \sin \nu \sqrt{\frac{3}{2}} \hat{a}_1(-\varphi - \psi) = \sqrt{\frac{2}{3}} E H \sin \eta \sin \nu \hat{a}(-\varphi - \psi) \quad (6.6)$$

since $\hat{0}$ is perpendicular to \hat{a} by definition.

To summarize

$$\frac{1}{2} \vec{P}^M = \frac{1}{\sqrt{3}} E H \left\{ [2 \cos \eta \cos \nu - \sin \eta \sin \nu \cos(\varphi - \psi)] \hat{a} - \right.$$

$$- \left[\cos \eta \sin \nu \hat{u}(\psi) + \cos \nu \sin \eta \hat{u}(\varphi) \right] + \sqrt{2} \sin \eta \sin \nu \hat{u}(-\varphi - \psi) \} \quad (6.7)$$

The major results of Section 5 also hold for mixing.

Propagating along (1,1,1) ($\eta = \nu = \pi/2$)

$$\frac{1}{2} \vec{p}^M = EH \left[-\frac{1}{\sqrt{3}} \cos(\varphi - \psi) \hat{a} + \frac{\sqrt{2}}{3} \hat{u}(-\varphi - \psi) \right] \quad (6.8)$$

Here again the magnitude of the radiating polarization is independent of the azimuthal angle of either field. However the total polarization does depend on the angle between the two planes of incidence $\varphi - \psi$:

$$\left| \frac{1}{2} \vec{p}^M \right| = EH \sqrt{\frac{2 + \cos^2(\varphi - \psi)}{3}} \quad (\eta = \nu = \pi/2) \quad (6.9)$$

It is noteworthy that when the mixing fields are mutually perpendicular ($\varphi - \psi = \pm \pi/2$), $\vec{p}_{\parallel}^M = 0$ which could already be seen in Eq. (6.2a).

If $\vec{E} \parallel \vec{H}$, $(1/2)\vec{p}^M$ reduces to the form of Eq. (5.19) so that once again the radiating polarization may be made normal to the common plane of incidence by aligning the field with a (0,1,-1) type axis.

A different approach to the whole topic of mixing stems from the observation that the nonlinear polarization is a symmetric bilinear form ($\vec{p}(\vec{E}, \vec{H}) = \vec{p}(\vec{H}, \vec{E})$). By defining two new independent fields \vec{F} and \vec{G} as

$$\vec{F} = \frac{1}{2} (\vec{E} + \vec{H}) \quad (6.10a)$$

$$\vec{G} = \frac{1}{2} (\vec{E} - \vec{H}) \quad (6.10b)$$

the polarization can be expressed in the explicitly symmetric form of the second harmonic:

$$\vec{P}(\vec{E}, \vec{H}) = \vec{P}(\vec{F} + \vec{G}, \vec{F} - \vec{G}) = \vec{P}(\vec{F}) + \vec{P}(\vec{G}, \vec{F}) - \vec{P}(\vec{F}, \vec{G}) - \vec{P}(\vec{G})$$

or

$$\frac{1}{2} \vec{P} = \vec{P}(\vec{F}) - \vec{P}(\vec{G}) \quad (6.11)$$

Having succeeded in expressing the mixing as a superposition of second harmonic polarizations, all of the results of Sections II.4 and 5 can be taken over intact, with the proviso that the "fundamentals" \vec{F} and \vec{G} are the averages of \vec{E} with \vec{H} , and \vec{E} with $(-\vec{H})$ respectively.

One final observation: letting $\vec{E} = \vec{H}$ in Eq. (6.1) cannot recover the second harmonic expression but rather twice that. This famous factor of two is often referred to as the permutation degeneracy and introduced ad hoc to yield the correct result. It may however be understood in light of the fact that in the degenerate case the second harmonics of each individual field must be added in as well, resulting in four times the single field SHG value. But this is as it should be, considering that in this case the fields add coherently and we are really looking at the SHG of a field twice the strength of the original one.

II.7 Elliptically polarized fundamental

An interesting and useful generalization of the preceding theory obtains in considering the case of circular and elliptical polarization. Practically, such fundamentals can result anytime linearly polarized laser light is subjected to total internal reflection (viz. Born and Wolff 1980, section 1.5), or passed through a $\frac{1}{4}$ -wave plate. Heuristically, this situation can be shown to be desirable by recalling the dependence of the nonlinear polarization on the electric field strength. In linearly polarized light the field undergoes oscillations with a resulting rms value down a factor of $\sqrt{2}$ from the peak. The rms nonlinear polarization is then half of its peak, and the rms SH intensity only a quarter of the value corresponding to the maximum fundamental field strength. By contrast, with circularly polarized light, the fundamental field describes a helix of constant radius equal to the peak field strength, resulting in four times as much SH intensity. Normalizing to the same fundamental intensity, the SH intensity is still twice that of the linear case. In this and the following section we will put these ideas on a quantitative basis.

Consider an arbitrary cartesian coordinate system OXYZ. Denoting the usual phase angle by

$$\psi = kZ - \omega t \quad (7.1)$$

a general elliptically polarized wave propagating in the \hat{z} direction may be described by means of its real electric field

vector:

$$\vec{E} = a \cos \psi \hat{X} + b \sin \psi \hat{Y} \quad (7.2a)$$

Linear polarization obtains for $b=0$, while $a=b$ implies a right hand circularly polarized wave (conforming to the optical handedness definition; this corresponds to

left-handed screw motion). In complex form Eq. (7.2) reads

$$\vec{E} = \frac{e^{i\psi}}{2} (a \hat{X} - ib \hat{Y}) + c.c. \quad (7.2b)$$

or

$$\vec{E} = a \hat{X} - ib \hat{Y} \quad (7.2c)$$

The complex circular polarization unit vectors are

$$\hat{E}_+ = \frac{1}{\sqrt{2}} (\hat{X} + i\hat{Y}) \quad \text{left-handed (optics)} \quad (7.3a)$$

$$\hat{E}_- = \frac{1}{\sqrt{2}} (\hat{X} - i\hat{Y}) \quad \text{right-handed (optics)} \quad (7.3b)$$

(In what follows we will use the handedness definition

customary in optics). Equations (7.3) are easily inverted:

$$\hat{X} = \frac{1}{\sqrt{2}} (\hat{E}_+ + \hat{E}_-) \quad (7.4a)$$

$$\hat{Y} = \frac{1}{i\sqrt{2}} (\hat{E}_+ - \hat{E}_-) \quad (7.4b)$$

In terms of the epsilons, the complex \vec{E} amplitude is

$$\vec{E} = \frac{a-b}{\sqrt{2}} \hat{E}_+ + \frac{a+b}{\sqrt{2}} \hat{E}_- \quad (7.5)$$

i.e. our field can also be conceived of as a superposition of unequal, counter-rotating circularly polarized fields.

In cgs the instantaneous light intensity is

$$I(t) = \frac{cn}{4\pi} (\vec{E})^2 \quad (7.6a)$$

while the measurable rms value is

$$I = \frac{cn}{4\pi} \langle (\vec{E})^2 \rangle_{rms} \quad (7.6b)$$

With the elliptically polarized field of Eq. (7.2)

$$\langle (\vec{E})^2 \rangle_{rms} = \frac{a^2 + b^2}{2} = \frac{1}{2} |\vec{E}|^2 \quad (7.7)$$

which illustrates the factor of 2 variation in intensity as

the state of polarization changes from linear ($b=0$) to circular ($b=\pm a$).

It is convenient to describe an arbitrary propagation direction \hat{z} in terms of its deviation from the preferred $\hat{z} = (1/\sqrt{3})(1,1,1)$. Figure (7.1) shows the use of the Euler angles α , β and γ (after Messiah 1966, Fig. XIII.1) to parametrize the departure of the OXYZ from the Oxyz system previously defined in Eqs. (5.11a). The rotation matrix R which connects the two systems

$$\begin{pmatrix} X \\ Y \\ Z \end{pmatrix} = R^t \begin{pmatrix} x \\ y \\ z \end{pmatrix} \quad (7.8)$$

is conveniently found in Messiah 1966, Eq. (C.45) in terms of the Euler angles:

$$R(\alpha\beta\gamma) = \begin{pmatrix} \cos\gamma \cos\beta \cos\alpha - \sin\gamma \sin\alpha & -\sin\gamma \cos\beta \cos\alpha - \cos\gamma \sin\alpha & \sin\beta \cos\alpha \\ \cos\gamma \cos\beta \sin\alpha + \sin\gamma \cos\alpha & -\sin\gamma \cos\beta \sin\alpha + \cos\gamma \cos\alpha & \sin\beta \sin\alpha \\ -\cos\gamma \sin\beta & \sin\gamma \sin\beta & \cos\beta \end{pmatrix} \quad (7.9)$$

Furthermore, if we denote by M the unitary matrix

$$M = \frac{1}{\sqrt{2}} \begin{pmatrix} 1 & 1 & 0 \\ -i & i & 0 \\ 0 & 0 & \sqrt{2} \end{pmatrix} \quad (7.10)$$

arising from Eqs. (7.4), the transformation between circular polarization coordinate systems is

$$\begin{pmatrix} \hat{\epsilon}_+ \\ \hat{\epsilon}_- \\ \hat{z} \end{pmatrix} = \tilde{M} R^t M \begin{pmatrix} \hat{\epsilon}_+ \\ \hat{\epsilon}_- \\ \hat{z} \end{pmatrix} \equiv \overline{R}^t \begin{pmatrix} \hat{\epsilon}_+ \\ \hat{\epsilon}_- \\ \hat{z} \end{pmatrix} \quad (7.11)$$

The tilde stands for the Hermitian adjoint operation (transposition and complex conjugation), and the lower case epsilons serve the circular polarization functions in the Oxyz system. The transformed matrix

$$\overline{R}^t = \begin{pmatrix} e^{-i\alpha} \left(\frac{\cos\beta+1}{2} \right) e^{-i\alpha} & e^{-i\alpha} \left(\frac{\cos\beta-1}{2} \right) e^{i\alpha} & -\frac{\sqrt{2}}{2} e^{-i\alpha} \sin\beta \\ e^{i\alpha} \left(\frac{\cos\beta-1}{2} \right) e^{-i\alpha} & e^{i\alpha} \left(\frac{\cos\beta+1}{2} \right) e^{i\alpha} & -\frac{\sqrt{2}}{2} e^{i\alpha} \sin\beta \\ \frac{\sqrt{2}}{2} \sin\beta e^{-i\alpha} & \frac{\sqrt{2}}{2} \sin\beta e^{i\alpha} & \frac{\sqrt{2}}{2} \cos\beta \end{pmatrix} \quad (7.12)$$

looks very much like the transformation matrix for the harmonic polynomials rY_1^m which the unit vectors \hat{e}_\pm , \hat{z} and \hat{e} , \hat{z} formally resemble.

The reason for invoking the foregoing mathematical apparatus becomes apparent when the connection is seen between the circular unit vectors and the positive "cubic" lattice directions (100), (010) and (001) (labeled by \hat{f}_j). A straight forward application of Eq. (5.11b) in conjunction with the definition of the epsilons reveals the following convenient expressions

$$\hat{E}_\pm = \frac{1}{\sqrt{3}} \sum_{j=1}^3 e^{\pm(j-1)i\frac{2\pi}{3}} \hat{f}_j \quad (7.13a)$$

$$\begin{pmatrix} \hat{E}_+ \\ \hat{E}_- \\ \hat{z} \end{pmatrix} = \frac{1}{\sqrt{3}} \begin{pmatrix} 1 & e^{i\frac{2\pi}{3}} & e^{i\frac{4\pi}{3}} \\ 1 & e^{-i\frac{2\pi}{3}} & e^{-i\frac{4\pi}{3}} \\ 1 & 1 & 1 \end{pmatrix} \begin{pmatrix} \hat{f}_1 \\ \hat{f}_2 \\ \hat{f}_3 \end{pmatrix} \quad (7.13b)$$

These we shall employ to advantage in complicated equations

such as (4.17)

A significant part of the earlier formalism has relied on the decomposition of vectors in components parallel and perpendicular to $\hat{z} = \hat{a}$, the three-fold axis of the $\bar{4}_3m$ system.

$$\vec{E} = \frac{1}{\sqrt{2}} \left[(a-b), (a+b), 0 \right] \begin{pmatrix} \hat{E}_+ \\ \hat{E}_- \\ \hat{z} \end{pmatrix} = \frac{1}{\sqrt{2}} \left[(a-b), (a+b), 0 \right] \bar{R}^T \begin{pmatrix} \hat{E}_+ \\ \hat{E}_- \\ \hat{z} \end{pmatrix} \quad (7.14a)$$

$$\equiv E_{\parallel} \hat{z} + E^+ \hat{E}_+ + E^- \hat{E}_- \quad (7.14a)$$

$$\equiv E_{\parallel} \hat{z} + \vec{E}_{\perp} \quad (7.14b)$$

The values of E_{\parallel} , E^+ and E^- are

$$E_{\parallel} = -\frac{1}{2} \left[(a+b) e^{i\gamma} + (a-b) e^{-i\gamma} \right] \sin \beta \quad (7.15a)$$

$$E^+ = \frac{1}{\sqrt{2}} \left[\left(\frac{a-b}{2} \right) e^{-i\gamma} (\cos \beta + 1) e^{-i\alpha} + \left(\frac{a+b}{2} \right) e^{i\gamma} (\cos \beta - 1) e^{-i\alpha} \right] \quad (7.15b)$$

$$E^- = \frac{1}{\sqrt{2}} \left[\left(\frac{a-b}{2} \right) e^{-i\gamma} (\cos \beta - 1) e^{i\alpha} + \left(\frac{a+b}{2} \right) e^{i\gamma} (\cos \beta + 1) e^{i\alpha} \right] \quad (7.15c)$$

The SH polarization is still described by the formulae of Section 4, but now the electric fields therein must be construed to be the complex quantities described in the present section. For example, E_{\perp}^2 of Eq. (4.14) is seen from Eq. (7.14a) to be

$$E_{\perp}^2 = 2 E^+ E^- \quad (7.16)$$

since

$$\hat{E}_+ \cdot \hat{E}_+ = 0 \quad (7.17a)$$

and

$$\hat{\mathcal{E}}_+ \cdot \hat{\mathcal{E}}_- = |\hat{\mathcal{E}}_{\pm}|^2 = 1 \quad (7.17b)$$

(Note that the \pm superscripts refer to the circular basis, whereas as subscripts, they refer to sign changing of invariant components under the twinning operation).

We have found that the evaluation of \vec{p}_+ and \vec{p}_- under these circumstances proceeds most efficiently by extending the simple results of Eqs. (4.13) to circular polarization. Using expression (7.13) for the circular unit vectors and the following identities

$$e^{\pm(j-1)i\frac{2\pi}{3}} = e^{\mp(j-1)i\frac{2\pi}{3}} \quad (7.18a)$$

and

$$\sum_{j=1}^3 e^{\pm(j-1)i\frac{2\pi}{3}} = 0 \quad (7.18b)$$

it is straight forward to derive the results listed in Table 7.1. Since any vector can be expanded in the circular basis (as in Eq. (7.14a)), this table plus the bilinearity of \vec{p} enables us to evaluate any doubling or mixing nonlinear polarization. Thus for SHG, \vec{p}_+ is simply

$$\vec{p}_+ = \frac{2}{\sqrt{3}} \left[\hat{\mathcal{E}} (E_{||}^2 - E^+ E^-) - E_{||} \vec{E}_{\perp} \right] \quad (7.19a)$$

$$= p_+'' \hat{\mathcal{E}} + p_+^+ \hat{\mathcal{E}}_+ + p_+^- \hat{\mathcal{E}}_- \quad (7.19b)$$

(see Eq. (4.14) for comparison) and

$$\vec{p}_- = \frac{2}{\sqrt{3}} \left[(E^-)^2 \hat{\mathcal{E}}_+ + (E^+)^2 \hat{\mathcal{E}}_- \right] \quad (7.20a)$$

$$\equiv p_+^+ \hat{\epsilon}_+ + p_-^- \hat{\epsilon}_- \quad (7.20b)$$

Note that in arriving at Eqs. (7.19) and (7.20) we have made no assumption concerning the orientation and state of polarization of the fundamental. They can still be chosen arbitrarily by giving values to the Euler angles as well as to the a and b amplitudes.

To obtain the state of polarization of the SH wave we must now transform back from $O \epsilon_+ \epsilon_- z$ to the $O \hat{\epsilon}_+ \hat{\epsilon}_- \hat{z}$

$$\begin{pmatrix} \hat{\epsilon}_+ \\ \hat{\epsilon}_- \\ \hat{z} \end{pmatrix} = (\bar{R}^t)^{-1} \begin{pmatrix} \epsilon_+ \\ \epsilon_- \\ z \end{pmatrix} = \tilde{M} R M \begin{pmatrix} \hat{\epsilon}_+ \\ \hat{\epsilon}_- \\ \hat{z} \end{pmatrix} = \tilde{R}^t \begin{pmatrix} \epsilon_+ \\ \epsilon_- \\ z \end{pmatrix} \equiv \bar{R} \begin{pmatrix} \hat{\epsilon}_+ \\ \hat{\epsilon}_- \\ \hat{z} \end{pmatrix} \quad (7.21)$$

We can read off $\bar{R} = \tilde{R}^t$ from Eq. (7.12)

$$\bar{R} = \begin{pmatrix} e^{i\alpha} \left(\frac{\cos\beta+1}{2}\right) e^{i\alpha} & e^{-i\alpha} \left(\frac{\cos\beta-1}{2}\right) e^{i\alpha} & \frac{\sqrt{2}}{2} \sin\beta e^{i\alpha} \\ e^{i\alpha} \left(\frac{\cos\beta-1}{2}\right) e^{-i\alpha} & e^{-i\alpha} \left(\frac{\cos\beta+1}{2}\right) e^{-i\alpha} & \frac{\sqrt{2}}{2} \sin\beta e^{-i\alpha} \\ -\frac{\sqrt{2}}{2} e^{i\alpha} \sin\beta & -\frac{\sqrt{2}}{2} e^{-i\alpha} \sin\beta & \frac{\sqrt{2}}{2} \cos\beta \end{pmatrix} \quad (7.22)$$

In the symbolic notation of Eqs. (7.19b) and (7.20b) the nonlinear polarization radiating at frequency 2ω in the \hat{z} direction is

$$\begin{aligned} \vec{P}_{\text{rad}} = & \left[p_+^+ e^{i\alpha} \left(\frac{\cos\beta+1}{2}\right) e^{i\alpha} + p_+^- e^{-i\alpha} \left(\frac{\cos\beta-1}{2}\right) e^{-i\alpha} - p_+^{\parallel} \frac{\sqrt{2}}{2} e^{i\alpha} \sin\beta \right] \hat{\epsilon}_+ + \\ & + \left[p_+^+ e^{-i\alpha} \left(\frac{\cos\beta-1}{2}\right) e^{i\alpha} + p_+^- e^{-i\alpha} \left(\frac{\cos\beta+1}{2}\right) e^{-i\alpha} - p_+^{\parallel} \frac{\sqrt{2}}{2} e^{-i\alpha} \sin\beta \right] \hat{\epsilon}_- + \\ & + \left[p_-^+ e^{i\alpha} \left(\frac{\cos\beta+1}{2}\right) e^{i\alpha} + p_-^- e^{i\alpha} \left(\frac{\cos\beta-1}{2}\right) e^{-i\alpha} \right] \hat{\epsilon}_+ + \\ & + \left[p_-^+ e^{-i\alpha} \left(\frac{\cos\beta-1}{2}\right) e^{i\alpha} + p_-^- e^{-i\alpha} \left(\frac{\cos\beta+1}{2}\right) e^{-i\alpha} \right] \hat{\epsilon}_- \end{aligned} \quad (7.23)$$

Of these four terms, the latter two (arising from the sign changing term of the nonlinear polarization) will tend to build up as the wave progresses through the twinned material.

II.8 (1,1,1) propagation

Intriguing as it may seem, \vec{p}_{rad} of Eq. (7.23) is much too general - and therefore complex - to extract physical insight from. Much more can be said, however, if we let $\hat{z} = \hat{z}$ in Fig. (7.1). Then, using our definition (5.1b)

$$\vec{E} = a \cos \psi \hat{u}(\varphi) + b \sin \psi \hat{u}\left(\varphi + \frac{\pi}{2}\right) \quad (8.1)$$

where

$$\hat{u}(\varphi) = \hat{X} \quad ; \quad \hat{u}\left(\varphi + \frac{\pi}{2}\right) = \hat{Y}$$

In the Oxyz system, \vec{E} is written

$$\begin{aligned} \vec{E} &= (a \cos \psi \cos \varphi - b \sin \psi \sin \varphi) \hat{x} + (a \cos \psi \sin \varphi + b \sin \psi \cos \varphi) \hat{y} \\ &= \left[\left(\frac{a+b}{2}\right) \cos(\psi + \varphi) + \left(\frac{a-b}{2}\right) \cos(\psi - \varphi) \right] \hat{x} + \left[\left(\frac{a+b}{2}\right) \sin(\psi + \varphi) + \left(\frac{a-b}{2}\right) \sin(\psi - \varphi) \right] \hat{y} \\ \vec{E} &= \left(\frac{a+b}{2}\right) \hat{u}(\psi + \varphi) + \left(\frac{a-b}{2}\right) \hat{u}(-\psi + \varphi) \end{aligned} \quad (8.2)$$

which shows the superposition of unequal, counter-rotating fields. As in Eq. (7.2c) the complex amplitude is

$$\vec{E} = a \hat{u}(\varphi) - ib \hat{u}\left(\varphi + \frac{\pi}{2}\right) \quad (8.3a)$$

$$= \frac{a-b}{\sqrt{2}} e^{-i\varphi} \hat{e}_+ + \frac{a+b}{\sqrt{2}} e^{i\varphi} \hat{e}_- \quad (8.3b)$$

The components of \vec{E} in the $0 \hat{e}_+ \hat{e}_-$ system (Eqs. (7.15)) are much simpler

$$E_{11} = 0 \quad (8.4a)$$

$$E_{1+} = \frac{a-b}{\sqrt{2}} e^{-i\varphi} \quad (8.4b)$$

$$E_{1-} = \frac{a+b}{\sqrt{2}} e^{i\varphi} \quad (8.4c)$$

as well as those of \vec{p}_+ (Eqs. (7.19))

$$\vec{P}_+ = -\frac{2}{\sqrt{3}} \hat{z} \left(\frac{a^2 - b^2}{2} \right) \quad (8.5)$$

and of \vec{P}_- (Eqs. (7.20a))

$$\vec{P}_- = \frac{1}{\sqrt{3}} \left[(a+b)^2 e^{2i\psi} \hat{E}_+ + (a-b)^2 e^{-2i\psi} \hat{E}_- \right] \quad (8.6)$$

To find the rectified polarization, we go back to Section 4 (keeping in mind a different value for the susceptibility), and in each quadratic expression in the electric field we replace one of the powers by its complex conjugate. Thus, Eq. (4.14) will read

$$\vec{P}_+(0) = \frac{2}{\sqrt{3}} \hat{a} |E_{||}|^2 - \frac{1}{\sqrt{3}} \hat{a} |E_{\perp}|^2 - \frac{2}{\sqrt{3}} E_{||} \vec{E}_{\perp}^* \quad (8.7)$$

It does not matter which of the factors is conjugated, since for the final expression only the real part remains. For (111) propagation Eq. (8.7) simplifies to

$$\vec{P}_+(0) = -\frac{2}{\sqrt{3}} \left[\left(\frac{a-b}{2} \right)^2 + \left(\frac{a+b}{2} \right)^2 \right] = -\frac{2}{\sqrt{3}} \hat{z} \left(\frac{a^2 + b^2}{2} \right) \quad (8.8)$$

Similarly, using the results of Table 7.1, \vec{P}_- of Eq. (4.15a) is changed to

$$\begin{aligned} \vec{P}_-(0) &= \vec{P}_{\perp}(\vec{E}_{\perp}, \vec{E}_{\perp}^*) = \frac{2}{\sqrt{3}} \left[(E^+) (E^-)^* \hat{E}_- + (E^-) (E^+)^* \hat{E}_+ \right] \\ &= \frac{2}{\sqrt{3}} \left(\frac{a^2 - b^2}{2} \right) \left(e^{-2i\psi} \hat{E}_- + e^{2i\psi} \hat{E}_+ \right) = \sqrt{\frac{2}{3}} (a^2 - b^2) \hat{u}(-2\psi) \end{aligned} \quad (8.9)$$

The total real time dependent nonlinear polarization is

$$\begin{aligned} \vec{P}(t) &= \left[\frac{1}{2} (\vec{P}_+ + \vec{P}_-) e^{i2\psi} + \frac{1}{2} (\vec{P}_+(0) + \vec{P}_-(0)) \right] + c.c. \\ &= \left[-\frac{1}{\sqrt{3}} \hat{z} (a^2 + b^2) + \sqrt{\frac{2}{3}} (a^2 - b^2) \hat{u}(-2\psi) \right] - \end{aligned} \quad (8.10a)$$

(dc polarization)

$$-\frac{1}{\sqrt{3}} \hat{z} (a^2 - b^2) \cos 2\psi +$$

(longitudinal wave)

$$+ 2\sqrt{\frac{2}{3}} \left[\left(\frac{a+b}{2} \right) \hat{u}(-2\psi - 2\varphi) + \left(\frac{a-b}{2} \right) \hat{u}(2\psi - 2\varphi) \right]$$

(radiating polarization)

(8.10b)

Equation (8.10b) reveals a number of interesting properties. Firstly the radiated field must in general be elliptically polarized and may be described as a superposition of counter-rotating circular fields. When the fundamental is circularly polarized ($a = \pm b$) the SH wave will be likewise. The input and output, however, have opposite handedness as has been previously pointed out (Simon and Bloembergen 1968).

In the linear case ($b=0$) the amplitude of the ac part reduces of course to the form of Eq. (5.19)

$$\vec{p}(t) = a^2 \left[-\frac{1}{\sqrt{3}} \hat{z} + \sqrt{\frac{2}{3}} \hat{u}(-2\varphi) \right] (1 + \cos 2\psi)$$

(8.11)

since

$$\hat{u}(-2\psi - 2\varphi) + \hat{u}(2\psi - 2\varphi) = 2 \cos 2\psi \hat{u}(-2\varphi)$$

A right-handed fundamental ($b=a$) leads to a SH polarization

$$\vec{p}(t) = a^2 \left[-\frac{\hat{z}}{\sqrt{3}} (1 + \cos 2\psi) + 2\sqrt{\frac{2}{3}} \hat{u}(-2\psi - 2\varphi) \right]$$

(8.12)

The relationship between the instantaneous orientations of the fundamental and the SH fields is depicted in Fig. 8.1 (there is no significance to their relative magnitude in the picture).

We are now in position to compare the efficiency of linear and circular polarizations for SHG. To do so, a

linearly polarized fundamental

$$\vec{E}_1(t) = a \hat{u}(\varphi) \cos \psi \quad (8.13)$$

is used firstly "as is" and secondly after passage through an ideal (no losses) quarter wave plate

$$\vec{E}_2(t) = \frac{a}{\sqrt{2}} \cos \psi \hat{u}(\varphi - \frac{\pi}{4}) + \frac{a}{\sqrt{2}} \sin \psi \hat{u}(\varphi + \frac{\pi}{4}) \quad (8.14)$$

In the first case the radiated polarization is

$$\vec{p}_1(t) = a^2 \sqrt{\frac{2}{3}} \hat{u}(-2\varphi) \cos 2\psi \quad (8.15)$$

while in the second case

$$\vec{p}_2(t) = a^2 \sqrt{\frac{2}{3}} \hat{u}(-2\psi - 2\varphi) \quad (8.16)$$

It is seen that, although the modulus of p is the same in both cases, the rms nonlinear polarization is $\sqrt{2}$ greater in the circular SHG. Consequently for equal input intensities, a circularly polarized fundamental would produce twice as much SHG intensity and conversion efficiency as its linear counterpart. This finding has apparently not been previously noted.

Frequency mixing of elliptical waves has analogous properties and is dealt with in Appendix A3.

II.9 Summation over twinned domains

In Section 1 the governing equation (1.1) for the second order field \vec{E}^3 (see Appendix II.A1 for derivation) was given to motivate the developments in subsequent sections on the sign-changing polarization components. This equation is equally valid for SHG and mixing (SFG and DFG) when the appropriate polarization is used for \vec{P}^3 . In the small signal approximation (II.A1) Eq. (1.1) integrates to

$$\vec{E}^3(r) - \vec{E}^3(r_0) = \frac{a \vec{P}^3}{i \Delta k} \left(e^{i \Delta k r} - e^{i \Delta k r_0} \right) \quad (9.1)$$

To avoid excessive handling of constants we now define a lower-case field \vec{e}^3 to parallel the definition of the lower-case polarization \vec{p}^3

$$\vec{E}^3 \equiv \frac{a d_{ijk}}{i \Delta k} \vec{e}^3 \quad (9.2)$$

so that Eq. (9.1) becomes

$$\vec{e}^3(r) - \vec{e}^3(r_0) = \vec{p}^3 \left(e^{i \Delta k r} - e^{i \Delta k r_0} \right) \quad (9.3)$$

We can apply solution (9.3) inside any homogeneous region ($\vec{p}^3 = \text{const.}$) such as the n th domain of a lamellarly twinned crystal, beginning at the $(n-1)$ th twin plane (r_{n-1}) and ending at the n th twin plane (r_n):

$$\vec{e}^3(r_n) - \vec{e}^3(r_{n-1}) = \vec{p}^3(n) \left(e^{i \Delta k r_n} - e^{i \Delta k r_{n-1}} \right) \quad (9.4)$$

If we now sum Eq. (9.4) over all domains j from 1 to n , the intermediate \vec{e}^3 fields drop out:

$$\vec{e}^3(n) - \vec{e}^3(0) = \vec{p}^3(n) e^{i\Delta k r_n} - \vec{p}^3(1) e^{i\Delta k r_0} + \sum_{j=1}^{n-1} [\vec{p}^3(j) - \vec{p}^3(j+1)] e^{i\Delta k r_j} \quad (9.5)$$

The reason we chose to group terms of equal phase together may already be apparent if one recalls the separation of \vec{p}^3 in an invariant and a sign changing part (e.g. Eq. 4.17):

$$\vec{p}^3(j) = \vec{p}^3_+ + (-1)^{j-1} \vec{p}^3_- = \vec{p}^3(j-1) + 2(-1)^{j-1} \vec{p}^3_- \quad (9.6)$$

Then the coefficient of each such phase factor in Eq. (9.5) is recognized to be

$$\begin{aligned} & [(-1)^{j-1} - (-1)^j] \vec{p}^3_- \\ \text{or} \\ \vec{e}^3(n) - \vec{e}^3(0) &= \vec{p}^3(n) e^{i\Delta k r_n} - \vec{p}^3(1) e^{i\Delta k r_0} - 2\vec{p}^3_- \sum_{j=1}^{n-1} (-1)^j e^{i\Delta k r_j} \\ &= \vec{p}^3(n) e^{i\Delta k r_n} - \vec{p}^3(0) e^{i\Delta k r_0} - 2\vec{p}^3_- \sum_{j=0}^{n-1} (-1)^j e^{i\Delta k r_j} \end{aligned} \quad (9.7)$$

This equation contains all the features of quasi-phase-matching. The simplest way to see this is to idealize each domain thickness as a coherence length, i.e.

$$\Delta k r_j = \sum_{l=1}^j \Delta k l_c = j\pi$$

Then Eq. (9.7) becomes

$$\vec{e}^3(n) - \vec{e}^3(0) = [(-1)^n - 1] \vec{p}^3_+ - 2n\vec{p}^3_- = \begin{cases} -2n\vec{p}^3_- & (n = \text{even}) \\ -2(\vec{p}^3_+ + n\vec{p}^3_-) & (n = \text{odd}) \end{cases} \quad (9.8)$$

With an even number of equal domains, Eq. (9.8) shows that only the sign changing part contributes. For a large n this is true regardless its parity. In both cases the nonlinear field is proportional to the number of domains n , i.e. the

intensity is quadratic in n .

If we take each domain to be an even number of coherence lengths thick, Eq. (9.4) already says that there is not any net gain in the nonlinear amplitude regardless of the number of domains. A more complete analysis of Eq. (9.7) in the case of equal domains was given earlier (Szilagyí, Hordvik and Schlossberg 1976).

Consider now a more general distribution of domain lengths. Eq. (9.7) still allows the statement that for an even number of coherence lengths the first two terms cancel identically and \vec{p}_- is still the only survivor.

It is worth emphasizing that none of the results in this section have depended on properties peculiar to any one crystal class. In other classes \vec{e}^3 would have been defined so that Eqs. (9.3 - 8) would involve the full nonlinear polarization instead of being rescaled by the nonlinear susceptibility coefficient. However, in the $\bar{4}3m$ class the preceding sections have obtained simple forms for the various nonlinear polarization components.

II.10 Stacking of twinned plates

The creation of artificial regularly twinned structures must await the development of the ideas presented in Chapter III. In the meantime, naturally twinned material may in principle be employed more effectively by stacking plates diced from the same plane-parallel piece. Initially proposed by Armstrong, Bloembergen, Ducuing and Pershan 1962, the stack-of-plates method has been implemented experimentally by a number of workers including Franken and Ward 1963 and Okada, Takizawa and Ieiri 1976 in quartz, Szilagyi, Hordvik and Schlossberg 1976 and Thompson, McMullen and Anderson 1976 in GaAs, and by Piltch, Cantrell and Sze 1976 in CdTe. The first achievement of SHG in a stack of twinned plates will be described in Section 11 for CdTe (Szilagyi and Dewey 1979).

For simplicity the propagation is coaxial with the stack normal and the spacings are assumed to be uniform. Ideally, to minimize Fresnel reflection losses, the plates would be brought into optical contact. In the following calculation this arrangement is the limiting case of $r_d = 0$, where r_d is the plate spacing. Consistent with the narrow distance, each field is assumed to undergo multiple reflections in the gap, resulting in a Fabry-Perot transmission coefficient. Within each plate, only the first forward pass is regarded as having contributed significantly to the nonlinear effect. The justification lies in the quadratic dependence of the nonlinear intensity on the fundamental, and in the relatively

low reflectivities resulting from the use of index matching fluids (see van der Ziel 1976).

The component of the polarization invariant under twinning was seen in Eq. (8.5) to be along the propagation direction. The remaining (sign changing) component was given in Eq. (8.6) and, since it is perpendicular to the propagation direction, it is also the radiating part. Accordingly (and dropping the superscript 3) the radiated wave of Eq. (9.7) becomes

$$\vec{e}(u) = \vec{e}(0) - 2\bar{p}_- N_n e^{i\Delta k r_0} \quad (10.1a)$$

where

$$N_n = \frac{1}{2} \left[1 - (-1)^n e^{i\Delta k (r_n - r_0)} + 2 \sum_{j=1}^n (-1)^j e^{i\Delta k (r_j - r_0)} \right] \quad (10.1b)$$

As was shown in the preceding section, in the case of ideal spacing

$$N_n = n \quad (10.2a)$$

for

$$\Delta k (r_j - r_0) = j\pi \quad (10.2b)$$

In general, though, N_n acts as an effective number of ideal domains, usually less than n , and is independent of the coordinate system.

The Fabry-Perot transmission \mathcal{T} (Born and Wolf 1980, Eq. 1.6.58) relates the field amplitudes and phases just before and just after the gap:

$$\mathcal{T} = \frac{T e^{i\delta/2}}{1 - R e^{i\delta}} = \sqrt{\mathcal{T}_{FP}} e^{i\frac{\delta}{2}} e^{i\phi} \quad (10.3a)$$

where

$$T = \frac{4n^0n}{(n^0+n)^2} ; R = 1 - T \quad (10.3b)$$

are the normal power transmissivity and reflectivity respectively, δ is the double reflection phase lag

$$\delta = 2k^0r_d = 4\pi n^0 \frac{r_d}{\lambda} \quad (10.3c)$$

T_{FP} is the Fabry-Perot intensity transmission and ϕ is given by

$$\phi = \arctan \left(\frac{R \sin \delta}{1 - R \cos \delta} \right) \quad (10.3d)$$

As an example, the radiated field after the second twinned plate but just before the second gap is

$$\vec{e}(2n) = \vec{e}(n) T_3 + [(\pm 1) T_1^2 e^{i\delta k r_n}] (-2\vec{P}_- N_n) \quad (10.4)$$

The subscripts on the Fabry-Perot transmissions indicate the frequency. The sign of the term in square brackets is to be chosen according to the value of the phase mismatch after one plate traversal. If the plate thickness is close to an odd multiple of the coherence length the second term of Eq. (10.4) will nearly cancel the nonlinear gain over the first plate unless the minus sign is chosen. Conversely, the plus sign is to be employed for plates approaching an even multiple of l_c in thickness. The method of implementing the sign change, as

seen in general terms from Eq. (2.12), consists of rotating every other plate 180° about the twin axis.

For the j^{th} plate, Eq. (10.4) becomes

$$\vec{e}(jn) = \vec{e}[(j-1)n] \mathcal{T}_3 + [(\pm 1) \mathcal{T}_1^2 e^{i\Delta k r_n}]^{j-1} (-2\vec{p}_- N_n) \quad (10.5)$$

To solve this difference equation, both sides are multiplied by \mathcal{T}_3^{m-j} and summed over j , leading to the cancellation of the intermediate fields:

$$\vec{e}(mn) = (-2\vec{p}_- N_n) \sum_{j=1}^m [(\pm 1) \mathcal{T}_1^2 e^{i\Delta k r_n}]^{j-1} \mathcal{T}_3^{m-j}$$

where $\vec{e}(0) = 0$. With a little rearrangement and the summation of the geometric series, the nonlinear field becomes

$$\vec{e}(mn) = -2\vec{p}_- N_n \mathcal{T}_3^{m-1} \frac{1 - [(\pm 1) \frac{\mathcal{T}_1^2}{\mathcal{T}_3} e^{i\Delta k r_n}]^m}{1 - (\pm 1) \frac{\mathcal{T}_1^2}{\mathcal{T}_3} e^{i\Delta k r_n}} \quad (10.6a)$$

$$\cong -2\vec{p}_- N_n M_m \quad (10.6b)$$

As in Eq. (10.1), M_m is an effective number of plates. Ideal stacking is obtained with optical contacting and with plate thickness an integral number of coherence lengths:

$$\vec{e}(mn) = -2\vec{p}_- N_n m \quad (10.7)$$

It should be noted that without the internal QPM due to twinning, only odd multiples of the coherence length would be allowed.

Expressed in terms of the intensity transmission

coefficients, Eq. (10.6) reads

$$M_m = \int_3^{m-1} \frac{1 - \left[(\pm 1) \sqrt{\frac{\sqrt{1FP}^2}}{\sqrt{3FP}} e^{i(\Delta k r_n + \Delta \frac{d}{2} + \Delta \phi)} \right]^m}{1 - (\pm 1) \sqrt{\frac{\sqrt{1FP}^2}}{\sqrt{3FP}} e^{i(\Delta k r_n + \Delta \frac{d}{2} + \Delta \phi)}} \quad (10.8)$$

In the limit of small plate separation ($r_d \ll \lambda$) Eq. (10.3d) may be approximated by

$$\phi \approx \frac{R}{T} d \quad (10.9)$$

which allows a simple expression for the phase occurring in Eq.

$$\begin{aligned} (10.8) \quad \Delta k r_n + \Delta \frac{d}{2} + \Delta \phi &\approx \Delta k r_n + \Delta d \left(\frac{1}{2} + \frac{R}{T} \right) \\ &= \Delta k r_n + 2\Delta k^0 r_d \left(\frac{1}{T} - \frac{1}{2} \right) \\ &= \Delta k r_n + \Delta k^0 r_d \left(\frac{2}{T} - 1 \right) \end{aligned} \quad (10.10)$$

In addition, if the immersion medium is nearly dispersionless, the only significant contribution to Eq. (10.10) will be that of the first term, due to the momentum mismatch within each plate.

To calculate the output of the stack, the multiplicative constants of Eqs. (9.2) and (A1.12) must be restored in Eq.

$$\begin{aligned} (10.7): \quad \vec{E}^3(mn) &= -\frac{8\pi}{n_3} \frac{e_c}{\lambda_3} d_{1k} \vec{P}_- N_n M_m \\ &= \vec{E}^3(e_c) N_n M_m \end{aligned} \quad (10.11)$$

where the field after a coherence length is defined in Eq. (A1.13). Also from Appendix A1 (Eq. (A1.16a)) but including the input and output Fresnel transmissions

$$I_3(m\lambda) = \frac{Cn_3}{8\pi} |\hat{U} \cdot \vec{E}^3(m\lambda)|^2 T_1^2 T_3^2$$

$$= I_3(l_c) N_n^2 M_m^2 T_1^2 T_3^2 \quad (10.12)$$

where the intensity from a coherence length plate can be found in Eq. (A1.18), and the square of M_m is

$$M_m^2 = \int_{3FP}^{m-1} \left\{ \frac{\left[1 - (\pm 1) \left(\frac{\sqrt{\sigma_{1FP}^2}}{\sqrt{\sigma_{3FP}}} \right)^{\frac{m-1}{2}} \right]^2 + 4 (\pm 1)^m \left(\frac{\sqrt{\sigma_{1FP}^2}}{\sqrt{\sigma_{3FP}}} \right)^{\frac{m-1}{2}} \sin m \left(\frac{\Delta k r_n + \Delta \frac{d}{2} + \Delta \phi}{2} \right)}{\left[1 - (\pm 1) \left(\frac{\sqrt{\sigma_{1FP}^2}}{\sqrt{\sigma_{3FP}}} \right)^{\frac{1}{2}} \right]^2 + 4 (\pm 1) \left(\frac{\sqrt{\sigma_{1FP}^2}}{\sqrt{\sigma_{3FP}}} \right)^{\frac{1}{2}} \sin \left(\frac{\Delta k r_n + \Delta \frac{d}{2} + \Delta \phi}{2} \right)} \right\} \quad (10.13)$$

The factorization of the stack effects (M_m) from the twin effects (N_n) in Eq. (10.12) is very convenient for practical applications. For example, the effects of the immersion medium, plate thickness and spacing may be evaluated without any regard for the twin spacing distribution or fundamental polarization. Figures 10.1a and b show M_m^2 versus m for various plate thicknesses in optical contact, and for various coherence length plate spacings, respectively. In the former picture, the thickness r_n is listed in dimensionless form as the phase angle

$$\psi = 180^\circ \frac{r_n d}{l_c}$$

The sinusoidal variation is analogous to the Maker fringes (Maker, Terhune, Nisenoff and Savage 1962) and is strictly

periodic. The oscillation in Fig. (10.1b) is not periodic and represents a generalization of the Maker effect to include Fabry-Perot multiple reflection losses. The curves are calculated for CdTe plates immersed in carbon disulphide liquid where the coherence length is 29um, and illustrate the sensitivity of the result to departures from optical contacting. A similar treatment has been given (Szilagyi, Hordvik and Schlossberg 1976) in the case of simple Fresnel reflection losses.

II.11 Experiments

The nonlinear intensity I_3 (Eq. (10.12)) resulting from the use of a stack of twinned plates was verified experimentally in the case frequency doubling. The successful completion of the experiment involved the following steps: crystal measurement, selection, design fabrication and orientation, the design and fabrication of an immersion cell, the use of a laser facility and data analysis.

The nonlinear material consisted of six CdTe plates, with two twin planes delineating three domains in each plate. Each domain was approximately 1_c in thickness. The six elements were obtained by dicing and polishing a wider area plate with the same twin configuration selected to maximize the effective number of ideal domains N_n of Eq. (10.1b). The CdTe material and fabrication were provided by II-VI, Inc..

The evaluation of N_n was programmed to be performed graphically by a Tektronix 4051 microcomputer using the Argand method (Wynne and Bloembergen 1969, and Dewey and Hocker 1975). The domain thicknesses were measured on a Nikon travelling microscope by viewing an obliquely illuminated surface lapped at an angle to the twin normals. The choice of this method was dictated by the need to produce sufficient contrast between adjacent domains. In retrospect, however, the grain revealing etch of Section III.3.3 would have considerably improved the contrast and simplified the measurement.

Figures 11.1a and b show the Argand plots for the parent crystal and the fabricated plates, respectively. The selected domains are identified in Fig. 11.1a as "#13", "#14" and "#15". Each plate was 598 μm thick. The resulting stack was characterized by $N_n = 2.88$ and $M_m = 2.83$, where the low value of M_m resulted from the significant departure of element thickness from the ideal value of $558 \mu\text{m} = 3 l_c'$ though close enough to require that every other plate be rotated by 180° about the stack normal (as per discussion following Eq. (10.4)).

The immersion cell, shown schematically in Fig. 11.2, featured a brass body made in an MIT machine shop. Viton gaskets were chosen for their resistance to the carbon disulphide index matching liquid. The ZnSe entrance and exit windows, supplied by II-VI, Inc., were aligned in such a way that the CO_2 laser beam incident at the Brewster angle for the ZnSe-air interface would then refract in a direction coaxial with the body of the cell and normal to the twinned plates. Inside the cell the stack was gently spring loaded onto a teflon lined, V-grooved jig. After mounting the stack, immersion fluid was injected into the cell through a reclosable intake hole under the protection of a fume hood.

With refractive indices of 2.4, 1.6 and 2.7 for ZnSe, CS_2 and CdTe respectively, the fundamental intensity is reduced by a factor of 0.46 inside the cell primarily due to the bending and widening of the beam. Conversely, the SH beam produced by the stack is intensified by a factor of 2.1 upon exiting the

cell. The conversion efficiency in the CS_2 is only a factor of 1.035 greater than the externally measured value.

To execute the experiment, time was reserved on a CO_2 TEA laser operated at Harvard University by J. Black under the direction of E. Yablonovich. Typical characteristics of the laser were as follows: TEM_{00} beam of 0.036 cm^2 area, with an output of 150 mJ in each 0.5 nsec pulse, repetition rate 0.3 Hz, peak power about 300 MW. After reflection from a NaCl beam splitter, a reference portion of the output was monitored by a Au:Ge detector in a side-looking Dewar. Interpretation of the readings was made possible by prior calibration against a Scientech energy meter. The fundamental intensity could be varied by changing the number of CaF_2 attenuator plates in the optical train. The second harmonic was separated from the fundamental by means of an interference filter, and measured with a calibrated P1-51 pyroelectric detector by Molelectron.

As expected, the SH intensity was accurately proportional to the square of the fundamental intensity. The experimental conversion efficiency inside the cell but outside the stack was $0.9(+0.4)\%$ at a fundamental intensity of 64 MW/cm^2 . The theoretical result of Eq. (10.12) predicts an efficiency of 1.2% for this configuration. The values used in the calculation are

$$N_n = 2.88$$

$$M_m = 2.83$$

$$\tilde{I}_1 = 64 \text{ MW/cm}^2$$

$$d_{\text{eff}} = \sqrt{\frac{2}{3}} d_{14}$$

$$d_{14} = 6 \times 10^{-11} \text{ m/V} \quad (\text{Dewey 1977})$$

(11.1)

$$T_1 \sim T_3 \approx 0.80$$

The agreement between experiment and theory is seen to be good. Under more favorable conditions ($N_n = 2.97$, $M_m = 6$ and $\bar{I}_1 = 100 \text{ MW/cm}^2$) the efficiency would have been almost 10% (9.4%).

Another cell design was also tested experimentally. The motivation was the diminished fundamental intensity in the Brewster cell resulting from beam bending. The second design featured normal incidence antireflection coated ZnSe windows. A nickel-copper bellows spring (supplied by Servometer Corp.) played the dual role of compressing the windows against the CdTe stack, and of sealing the immersion liquid inside the cell. In spite of a number of attractive characteristics, this design was plagued by mechanical problems involving bellows uniformity and optical component flatness. Transmission measurements revealed that optical contacting was not achieved, with inter-plate cumulative CS_2 optical path lengths between 10 and 30 μm . In addition, the uneven mechanical pressure damaged the plate surfaces, creating further obstacles to optical contacting.

The CdTe stack had been repolished for the normal incidence cell, bringing the plates to a thickness of 544 μm , or 14 μm less than the nearest coherence length multiple. It is likely that this characteristic was also a contributing

factor to the lack of success of this cell, as may be seen from the following considerations.

The wave number mismatch is defined in Eq. (A1.10).

Normal dispersion in CdTe ($n_1 = 2.67$, $n_2 = 2.69$) results in a negative value of k , whereas for CS_2 anomalous dispersion ($n_1 = 1.623$, $n_2 = 1.535$) yields a positive momentum mismatch. Examination of the phase factor in Eq. (10.8) reveals that for plates thicker than the nearest multiple of the coherence length, a beneficial cancellation of the phase mismatch will occur when the plates have a small but finite separation. Conversely, for plates thinner than the nearest multiple of l_c (such as the $544 \mu m$ thickness used in the second design), the interplate dephasing acts to the detriment of the conversion efficiency.

II.12 Conclusions

The results of this chapter will now be summarized in decreasing order of generality.

For second order nonlinear optics (NLO) in any crystal class, the new form of the susceptibility (Section 3 and Appendix A2) constitute a symmetrical and practical way of displaying the tensor elements and it permits the use of the well developed mathematical apparatus of quadratic and bilinear forms.

For quasi-phase-matching (QPM), the nonlinear polarization is decomposed in invariant and sign changing parts (Section 2), and the cumulative effects of twin sequences and of stacked plates (Sections 9 and 10) are given in crystal-class independent fashion.

Specifically in the $\bar{4}3m$ class, the new form of the susceptibility leads to explicit algebraic and trigonometric (Sections 4 and 5) decompositions of the nonlinear polarization into invariant and quasi-phase-matchable (sign-changing) parts under the twinning operation. For (1,1,1) propagation, the magnitude of the radiating polarization is found to be independent of the azimuthal angle of the fundamental. Furthermore, for selected azimuthal angles the radiated field is polarized normally to the linearly polarized fundamental, enabling convenient separation of the fields by means of Brewster windows.

The use of elliptically polarized waves is also treated

in this crystal class (Appendix A3). For equal fundamental intensities propagating along a (1,1,1) direction, circularly polarized light is shown to be twice as efficient as linearly polarized light. In frequency mixing, if at least one of the waves is circularly polarized, the QPM output is also circularly polarized, and vanishes if the two input waves have opposite helicity.

The 1% theoretical efficiency of frequency-doubling the CO₂ laser was verified experimentally in a stack of six CdTe plates contained in a Brewster angle cell with carbon disulphide as index matching medium.

It is concluded that quasi-phase-matching is already possible in judiciously selected twinned materials and that high efficiency mixing and doubling devices could be obtained from crystals with sufficient numbers of suitably spaced twins. Accordingly, there is great incentive to embark upon an investigative program into the nature and mechanisms of growth twinning.

II.A1 Idealized SHG intensity in coherence-length plate (cgs)

The major purpose of the following derivation is to record the definitions used in the text.

Maxwell's curl equations in a nonconducting ($\sigma=0$), nonmagnetic ($\mu=1$), uncharged ($\vec{\nabla} \cdot \vec{E} = 0$) medium

$$\vec{\nabla} \times \vec{H} = \frac{1}{c} \frac{\partial \vec{D}}{\partial t} \quad (\text{A1.1a})$$

and

$$\vec{\nabla} \times \vec{E} = -\frac{1}{c} \frac{\partial \vec{B}}{\partial t} \quad (\text{A1.1b})$$

may be combined into a wave equation with a nonlinear source term

$$\nabla^2 \vec{E} - \frac{\epsilon}{c^2} \frac{\partial^2 \vec{E}}{\partial t^2} = \frac{4\pi}{c^2} \frac{\partial^2 \vec{P}^{NL}}{\partial t^2} \quad (\text{A1.2})$$

where the nonlinear polarization obeys

$$\vec{D} = \epsilon \vec{E} + 4\pi \vec{P}^{NL} \quad (\text{A1.3})$$

For SHG, the fields are assumed to consist of only two Fourier components, the fundamental and the second harmonic. The parametric (also called small signal) approximation consists of neglecting the presence of higher order harmonics and combination frequencies as well as the influence of the developing SH onto the pump field. In general the boundary conditions require the nonlinear wave to start with a nonzero value equal to the nonlinear reflected wave. This initial value may be neglected when (Bloembergen 1965, Ch. 4.1)

$$\left(\frac{2\epsilon_2}{\epsilon_2 - \epsilon_1}\right)^2 \gg 1 \quad (\text{A1.4})$$

Since this value is proportional to the square of the ratio of the coherence length to the fundamental wavelength, the inequality holds in most instances of practical interest. For doubling of 10.6 μm in CdTe this value is about 143000, which amply justifies the approximation.

The small ratio of wavelength to coherence length also justifies the so-called slow envelope approximation, where

$$\nabla^2 \vec{E} \approx \frac{1}{2} e^{i\psi} (2i\vec{k} \cdot \nabla - k^2) \vec{E}(\vec{r}) + c.c. \quad (\text{A1.5})$$

Here $\vec{E}(\vec{r})$ is the slowly varying amplitude of the harmonic wave

$$\vec{E}(\vec{r}, t) = \frac{1}{2} \vec{E}(\vec{r}) e^{i\psi} + c.c. \quad (\text{A1.6a})$$

with

$$\psi = \vec{k} \cdot \vec{r} - \omega t \quad (\text{A1.6b})$$

and

$$k^2 = \epsilon \frac{\omega^2}{c^2} \equiv \epsilon k_0^2 \quad (\text{A1.6c})$$

With these approximations the left-hand side of the wave equation (2) becomes

$$\nabla^2 \vec{E} - \frac{\epsilon}{c^2} \frac{\partial^2 \vec{E}}{\partial t^2} = \frac{1}{2} e^{i\psi} (2i\vec{k} \cdot \nabla) \vec{E}(\vec{r}) + c.c. \quad (\text{A1.7a})$$

and the right-hand side

$$\frac{4\pi}{c^2} \frac{\partial^2 \vec{P}^{NL}}{\partial t^2} = -4\pi \frac{\omega^2}{c^2} \vec{P}^{NL} \quad (\text{A1.7b})$$

The phases ψ_S and ψ_T of the source (polarization) and total (radiated) waves at the SH are

$$\psi_S = 2\vec{k}_1 \cdot \vec{r} - 2\omega t \quad (\text{A1.8a})$$

$$\psi_T = \vec{k}_3 \cdot \vec{r} - 2\omega t \quad (\text{A1.8b})$$

Equating complex coefficients at the same frequency in Eqs.

$$\begin{aligned} (7) \quad 2i(\vec{k}_3 \cdot \vec{\nabla}) \vec{E}^3(\vec{r}) e^{i\vec{k}_3 \cdot \vec{r}} &= -4\pi \left(\frac{\omega_3}{c}\right)^2 \vec{P}^3(\vec{r}) e^{2i\vec{k}_1 \cdot \vec{r}} \\ \text{or} \\ \vec{k}_3 \cdot \vec{\nabla} \vec{E}^3(\vec{r}) &= 2\pi i \left(\frac{k_3}{n_3}\right)^2 \vec{P}^3(\vec{r}) e^{i\Delta\vec{k} \cdot \vec{r}} \end{aligned} \quad (\text{A1.9})$$

where the NL superscript has been replaced by the identification of the "third wave" (second order nonlinear optics corresponds in general to three-wave interactions), and the wave-vector mismatch is

$$\Delta\vec{k} = 2\vec{k}_1 - \vec{k}_3 \quad (\text{A1.10})$$

For collinear mixing or doubling, the scalar products in Eq. (9) become ordinary products:

$$\frac{\partial}{\partial r} \vec{E}(r) = 2\pi i \frac{k_3}{n_3^2} \vec{P}^3(r) e^{i\Delta k r} \quad (\text{A1.11})$$

Eq. (11) identifies the constant a of Eq. (1.1)

$$a = 2\pi i \frac{k_3}{n_3^2} = \frac{4\pi^2 i}{n_3 \lambda_3} \quad (\text{A1.12})$$

In the small signal approximation the depletion of the pump wave is neglected. The integration of Eq. (11) is then

simply

$$\vec{E}^3(r) - \vec{E}^3(0) = \frac{2\pi k_3}{n_3^2 \Delta k} \vec{P}^3 \left(e^{i\Delta k r} - 1 \right) \quad (\text{A1.13})$$

and after a coherence length

$$\vec{E}^3(l_c) = -\delta\pi \left(\frac{l_c}{n_3 \lambda_3} \right) \vec{P}^3 \quad (\text{A1.14})$$

where the initial value was neglected as previously noted, and

where

$$\Delta k l_c \equiv \pi \quad (\text{A1.15})$$

The useful nonlinear intensity may arise out of the component of the radiated wave along a given unit vector \hat{u}_0

$$I_3 = \frac{cn_3}{\delta\pi} |\hat{u}_0 \cdot \vec{E}^3|^2 \quad (\text{A1.16a})$$

$$= \frac{\delta\pi c}{n_3} \left(\frac{l_c}{\lambda_3} \right)^2 |\hat{u}_0 \cdot \vec{P}^3|^2 \quad (\text{A1.16b})$$

Defining the effective susceptibility d_{eff} as

$$\hat{u}_0 \cdot \vec{P}^3 \equiv d_{\text{eff}} |\vec{E}|^2 \quad (\text{A1.17})$$

and expressing in terms of the fundamental intensity (without reflection losses) Eq. (16b) becomes

$$I_3(l_c) = \frac{\delta\pi c}{n_3} \left(\frac{l_c}{\lambda_3} \right)^2 d_{\text{eff}}^2 I_1^2 \left(\frac{\delta\pi}{cn_1} \right)^2$$

or

$$I_3(l_c) = \frac{(\delta\pi)^3}{cn_3 n_1^2} \left(\frac{l_c}{\lambda_3} \right)^2 d_{\text{eff}}^2 I_1^2 \quad (\text{cgs}) \quad (\text{A1.18a})$$

The conversion from mks to cgs units obtains by replacing ϵ_0 * d_{eff} by d_{eff} and ϵ_0 by $\frac{1}{4}\pi$ or

$$I_3(\ell_c) = \frac{\rho}{\epsilon_0 c n_3 n_1^2} \left(\frac{\ell_c}{\lambda_3} \right)^2 d_{\text{eff}}^2 I_1^2 \quad (\text{mks}) \quad (\text{A1.18b})$$

For SFG or DFG we must replace I_1^2 by $4I_1 I_2$. No reference has been made so far to the crystal class. In the $\bar{4}3m$ system, d_{eff} is most generally calculated in the "natural" coordinate system of Section 7. With a fundamental amplitude as in Eq. (7.14a), Table 7.1 enables the immediate evaluation of Eq.

(17):

$$\hat{u}_0 \cdot \vec{P} = d_{14} \hat{u}_0 \cdot \vec{P} \left(\frac{E^+}{|E|} \hat{e}_+ + \frac{E^-}{|E|} \hat{e}_- + \frac{E_{||}}{|E|} \hat{a} \right) |E|^2 \quad (\text{A1.19})$$

i.e.

$$\begin{aligned} \frac{d_{\text{eff}}}{d_{14}} &= \hat{u}_0 \cdot \left[\bar{P}(\hat{e}_+) (E^+)^2 + \bar{P}(\hat{e}_-) (E^-)^2 + \bar{P}(\hat{a}) E_{||}^2 + \right. \\ &\quad \left. + 2\bar{P}(\hat{e}_+, \hat{e}_-) E^+ E^- + 2\bar{P}(\hat{e}_+, \hat{a}) (E^+) E_{||} + 2\bar{P}(\hat{e}_-, \hat{a}) (E^-) E_{||} \right] \frac{1}{|E|^2} \\ &= \frac{2}{\sqrt{3}} \left\{ \hat{u}_0 \cdot \hat{e}_- \left[\frac{(E^+)^2 - (E^-) E_{||}}{|E|^2} \right] + \hat{u}_0 \cdot \hat{e}_+ \left[\frac{(E^-)^2 - (E^+) E_{||}}{|E|^2} \right] + \hat{u}_0 \cdot \hat{a} \left[\frac{E_{||}^2 - (E^+) (E^-)}{|E|^2} \right] \right\} \quad (\text{A1.20}) \end{aligned}$$

For (111) propagation $\vec{E}_{||} = \hat{u} \cdot \vec{a} = 0$, and

$$\frac{d_{\text{eff}}}{d_{14}} = \frac{2}{\sqrt{3}} \hat{u}_0 \cdot \left[\frac{(a+b)^2 e^{2i\varphi} \hat{e}_+ + (a-b)^2 e^{-2i\varphi} \hat{e}_-}{(a+b)^2 + (a-b)^2} \right] \quad (\text{A1.21a})$$

where we used the field components of Eq. (8.4). Another form is

$$\frac{d_{\text{eff}}}{d_{14}} = \sqrt{\frac{2}{3}} \hat{u}_0 \cdot \left[\hat{u}(-2\varphi) + i \frac{2ab}{a^2+b^2} \hat{u} \left(-2\varphi + \frac{\pi}{2}\right) \right] \quad (\text{A1.21b})$$

Eqs. (21a or b) should be employed when the useful radiated wave is elliptically or linearly polarized, respectively.

II.A2 Nonlinear susceptibilities in new matrix form

The second harmonic coefficients appear below in the new form described in Section 3. They are arranged in 3 X 3 matrices after reprocessing the corresponding 3 X 6 matrices in Table 18.1 of Singh 1971 (with the exception of the 4mm class which was corrected using Table III of Kurz, Jerphagnon and Choy 1979).

The triclinic system (class 1 - C₁) provides a good example of the procedure used to obtain the listing below. In the 3 X 6 form, the susceptibility is given by

$$\text{Class 1 - C}_1 \quad \begin{pmatrix} d_{11} & d_{12} & d_{13} & d_{14} & d_{15} & d_{16} \\ d_{21} & d_{22} & d_{23} & d_{24} & d_{25} & d_{26} \\ d_{31} & d_{32} & d_{33} & d_{34} & d_{35} & d_{36} \end{pmatrix}$$

Recalling Eq. (3.2a), the nonlinear susceptibility is rewritten as follows:

$$\text{Class 1 - C}_1 \quad \begin{pmatrix} \hat{i}_j d_{j_1} & \hat{i}_j d_{j_6} & \hat{i}_j d_{j_5} \\ \hat{i}_j d_{j_6} & \hat{i}_j d_{j_2} & \hat{i}_j d_{j_4} \\ \hat{i}_j d_{j_5} & \hat{i}_j d_{j_4} & \hat{i}_j d_{j_3} \end{pmatrix}$$

Since this is a symmetric matrix, only the upper diagonal elements need be listed, the rest obtaining by transposition.

Monoclinic System

$$\begin{matrix} m - C_s \\ (m \perp Z) \end{matrix} \quad \begin{pmatrix} \hat{i}_1 d_{11} + \hat{i}_2 d_{21} & \hat{i}_1 d_{16} + \hat{i}_2 d_{26} & \hat{i}_3 d_{35} \\ & \hat{i}_1 d_{12} + \hat{i}_2 d_{22} & \hat{i}_3 d_{34} \\ & & \hat{i}_1 d_{13} + \hat{i}_2 d_{23} \end{pmatrix}$$

$$\frac{m - C_s}{(m \perp Y)} \text{ IRE convention} \begin{pmatrix} \hat{i}_1 d_{11} + \hat{i}_3 d_{31} & \hat{i}_2 d_{26} & \hat{i}_1 d_{15} + \hat{i}_3 d_{35} \\ & \hat{i}_1 d_{12} + \hat{i}_3 d_{32} & \hat{i}_2 d_{24} \\ & & \hat{i}_1 d_{13} + \hat{i}_3 d_{33} \end{pmatrix}$$

$$\frac{2 - C_2}{(2 \parallel Z)} \begin{pmatrix} \hat{i}_3 d_{31} & \hat{i}_3 d_{36} & \hat{i}_1 d_{15} + \hat{i}_2 d_{25} \\ & \hat{i}_3 d_{32} & \hat{i}_1 d_{14} + \hat{i}_2 d_{24} \\ & & \hat{i}_3 d_{33} \end{pmatrix}$$

$$\frac{2 - C_2}{(2 \parallel Y)} \text{ IRE convention} \begin{pmatrix} \hat{i}_2 d_{21} & \hat{i}_1 d_{16} + \hat{i}_3 d_{36} & \hat{i}_2 d_{25} \\ & \hat{i}_2 d_{22} & \hat{i}_1 d_{14} + \hat{i}_3 d_{34} \\ & & \hat{i}_2 d_{23} \end{pmatrix}$$

Orthorhombic System

$$\frac{mm2 - C_{2v}}{} \begin{pmatrix} \hat{i}_3 d_{31} & 0 & \hat{i}_1 d_{15} \\ & \hat{i}_3 d_{32} & \hat{i}_2 d_{24} \\ & & \hat{i}_3 d_{33} \end{pmatrix}$$

$$\frac{222 - D_2}{{} } \begin{pmatrix} 0 & \hat{i}_3 d_{36} & \hat{i}_2 d_{25} \\ & 0 & \hat{i}_1 d_{14} \\ & & 0 \end{pmatrix}$$

Tetragonal System

$$\underline{4 - C_4} \quad \begin{pmatrix} \hat{i}_3 d_{31} & 0 & \hat{i}_1 d_{15} - \hat{i}_2 d_{14} \\ & \hat{i}_3 d_{31} & \hat{i}_1 d_{14} + \hat{i}_2 d_{15} \\ & & \hat{i}_3 d_{33} \end{pmatrix}$$

$$\underline{\bar{4} - S_4} \quad \begin{pmatrix} \hat{i}_3 d_{31} & \hat{i}_3 d_{36} & \hat{i}_1 d_{15} + \hat{i}_2 d_{14} \\ & -\hat{i}_3 d_{31} & \hat{i}_1 d_{14} - \hat{i}_2 d_{15} \\ & & 0 \end{pmatrix}$$

$$\underline{4mm - C_{4v}} \quad \begin{pmatrix} \hat{i}_3 d_{31} & 0 & \hat{i}_1 d_{15} \\ & \hat{i}_3 d_{31} & \hat{i}_2 d_{15} \\ & & \hat{i}_3 d_{33} \end{pmatrix}$$

$$\underline{\bar{4}2m - D_{2d}} \quad \begin{pmatrix} 0 & \hat{i}_3 d_{36} & \hat{i}_2 d_{14} \\ & 0 & \hat{i}_1 d_{14} \\ & & 0 \end{pmatrix}$$

$$\underline{422 - D_4} \quad d_{14} \begin{pmatrix} 0 & 0 & -\hat{i}_2 \\ & 0 & \hat{i}_1 \\ & & 0 \end{pmatrix}$$

Trigonal System

$$\frac{3 - C_3}{\text{IRE convention}} \begin{pmatrix} \hat{i}_1 d_{11} - \hat{i}_2 d_{22} + \hat{i}_3 d_{31} & -\hat{i}_1 d_{22} - \hat{i}_2 d_{11} & \hat{i}_1 d_{15} - \hat{i}_2 d_{14} \\ & -\hat{i}_1 d_{11} + \hat{i}_2 d_{22} + \hat{i}_3 d_{31} & \hat{i}_1 d_{14} + \hat{i}_2 d_{15} \\ & & \hat{i}_3 d_{33} \end{pmatrix}$$

$$\frac{3m - C_{3v}}{(m \perp X)} \begin{pmatrix} -\hat{i}_2 d_{22} + \hat{i}_3 d_{31} & -\hat{i}_1 d_{22} & \hat{i}_1 d_{15} \\ & \hat{i}_2 d_{22} + \hat{i}_3 d_{31} & \hat{i}_2 d_{15} \\ & & \hat{i}_3 d_{33} \end{pmatrix}$$

IRE convention

$$\frac{3m - C_{3v}}{(m \perp Y)} \begin{pmatrix} \hat{i}_1 d_{11} + \hat{i}_3 d_{31} & -\hat{i}_2 d_{11} & \hat{i}_1 d_{15} \\ & -\hat{i}_1 d_{11} + \hat{i}_3 d_{31} & \hat{i}_2 d_{15} \\ & & \hat{i}_3 d_{33} \end{pmatrix}$$

$$\frac{32 - D_3}{\text{IRE convention}} \begin{pmatrix} \hat{i}_1 d_{11} & -\hat{i}_2 d_{11} & -\hat{i}_2 d_{14} \\ & -\hat{i}_1 d_{11} & \hat{i}_1 d_{14} \\ & & 0 \end{pmatrix}$$

Hexagonal System

$$\frac{\bar{6} - C_{3h}}{\text{IRE convention}} \begin{pmatrix} \hat{i}_1 d_{11} - \hat{i}_2 d_{22} & -\hat{i}_1 d_{22} - \hat{i}_2 d_{11} & 0 \\ & -\hat{i}_1 d_{11} + \hat{i}_2 d_{22} & 0 \\ & & 0 \end{pmatrix}$$

$\frac{6 - C_6}{\text{IRE convention}}$ same as $4 - C_4$

$$\frac{6m2 - D_{3h}}{(m \perp X)} \begin{pmatrix} -\hat{i}_2 & -\hat{i}_1 & 0 \\ & \hat{i}_2 & 0 \\ & & 0 \end{pmatrix}$$

IRE convention

$$\frac{\bar{6}m2-D_{3h}}{(m \perp Y)} \quad d_{11} \quad \begin{pmatrix} \hat{i}_1 & -\hat{i}_2 & 0 \\ & -\hat{i}_1 & 0 \\ & & 0 \end{pmatrix}$$

$$\frac{6mm - C_{6v}}{} \quad \text{same as } 4mm - C_{4v}$$

$$\frac{622 - D_6}{} \quad \text{same as } 422 - D_4$$

Cubic System

$$\frac{23 - T}{} \quad d_{14} \quad \begin{pmatrix} 0 & \hat{i}_3 & \hat{i}_2 \\ & 0 & \hat{i}_1 \\ & & 0 \end{pmatrix}$$

$$\frac{\bar{4}3m - T_d}{} \quad d_{14} \quad \begin{pmatrix} 0 & \hat{i}_3 & \hat{i}_2 \\ & 0 & \hat{i}_1 \\ & & 0 \end{pmatrix}$$

$$\frac{432 - O}{} \quad \text{All elements vanish.}$$

II.A3 Mixing of elliptically polarized light

In Section 7 a procedure was given to evaluate the nonlinear polarization by reference to Table 7.1, when the relevant fields are decomposed in the natural coordinate system (e.g. Eq. (7.14a)). Following that procedure, the mixing of elliptically polarized light will now be treated generally and the effective nonlinear susceptibility given for (1,1,1) propagation. Without loss of generality, the evaluation may be restricted to sum frequency generation (SFG). The difference frequency case obtains by complex conjugation of one of the field amplitudes.

The field envelopes \vec{E} and \vec{H}

$$\begin{aligned}\vec{E} &\equiv E_{\parallel} \hat{a} + E^+ \hat{e}_+ + E^- \hat{e}_- \\ \vec{H} &\equiv H_{\parallel} \hat{a} + H^+ \hat{e}_+ + H^- \hat{e}_-\end{aligned}\tag{A3.1}$$

produce a nonlinear polarization

$$\begin{aligned}\frac{1}{2} \vec{P}^M(\vec{E}, \vec{H}) &= \vec{P}(\hat{a}) E_{\parallel} H_{\parallel} + \vec{P}(\hat{e}_+) E^+ H^+ + \vec{P}(\hat{e}_-) E^- H^- + \\ &+ \vec{P}(\hat{a}, \hat{e}_+) (E_{\parallel} H^+ + E^+ H_{\parallel}) + \vec{P}(\hat{a}, \hat{e}_-) (E_{\parallel} H^- + E^- H_{\parallel}) + \vec{P}(\hat{e}_+, \hat{e}_-) (E^+ H^- + E^- H^+) \\ &= \frac{2}{\sqrt{3}} \left\{ \hat{a} \left[E_{\parallel} H_{\parallel} - \frac{(E^+ H^- + E^- H^+)}{2} \right] + \hat{e}_+ \left[E^- H^- - \frac{(E_{\parallel} H^+ + E^+ H_{\parallel})}{2} \right] + \hat{e}_- \left[E^+ H^+ - \frac{(E_{\parallel} H^- + E^- H_{\parallel})}{2} \right] \right\}\end{aligned}\tag{A3.2}$$

where we have used the distributivity property of the bilinear form \vec{P} , its symmetry with respect to the exchange of fields in the \vec{E}^M system (Giordmaine 1965), and Table 7.1. The sign changing part of Eq. (A3.2) is obtained according to Eq. (6.2b):

$$\frac{1}{2} \vec{P}^M(\vec{E}, \vec{H}) = \frac{2}{\sqrt{3}} \left[\hat{E}_+(E^-)(H^+) + \hat{E}_-(E^+)(H^+) \right] \quad (\text{A3.3})$$

(compare to Eq. (7.20a)).

Two interesting conclusions may be drawn from this result. Firstly, if one of the mixing fields is circularly polarized (e.g. $H^+ = 0$) the quasi-phase-matched output must also be circularly polarized (in the opposite sense). Secondly, if the input fields are both circularly polarized but of opposite handedness, the quasi-phase-matched output vanishes identically.

For (1,1,1) collinear propagation the mixing fields are

$$\vec{E} = \frac{a-b}{\sqrt{2}} e^{-i\varphi_e} \hat{E}_+ + \frac{a+b}{\sqrt{2}} e^{i\varphi_e} \hat{E}_- \quad (\text{A3.4a})$$

$$\vec{H} = \frac{c-d}{\sqrt{2}} e^{-i\varphi_h} \hat{E}_+ + \frac{c+d}{\sqrt{2}} e^{i\varphi_h} \hat{E}_- \quad (\text{A3.4b})$$

(following the development of Section 8). Substitution in Eq. (A3.3) and use of the effective susceptibility d_{eff}

$$\hat{u}_0 \cdot \vec{P}^M \equiv d_{\text{eff}} |\vec{E}| |\vec{H}| \quad (\text{A3.5})$$

yields

$$\frac{1}{2} \frac{d_{\text{eff}}}{d_{14}} = \frac{2}{\sqrt{3}} \left\{ \frac{(a+b)(c+d) e^{i(\varphi_e + \varphi_h)} \hat{u}_0 \cdot \hat{E}_+ + (a-b)(c-d) e^{-i(\varphi_e + \varphi_h)} \hat{u}_0 \cdot \hat{E}_-}{\sqrt{[(a-b)^2 + (a+b)^2][(c-d)^2 + (c+d)^2]}} \right\} \quad (\text{A3.6a})$$

Paralleling the SHG treatment of Appendix A1, this form is most useful when the desired output is circularly polarized. Otherwise, the following form is recommended

$$\frac{1}{2} \frac{d_{\text{eff}}}{d_{14}} = \sqrt{\frac{2}{3}} \left[\frac{(ac+bd)\hat{u}_0 \cdot \hat{u}(-\psi_e - \psi_h) + i(bc+ad)\hat{u}_0 \cdot \hat{u}(-\psi_e - \psi_h + \frac{\pi}{2})}{\sqrt{(a^2+b^2)(c^2+d^2)}} \right] \quad (\text{A3.6b})$$

As in the SHG case, circularly polarized input waves result in a larger effective susceptibility.

References

Armstrong, J.A., Bloembergen, N., Ducuing, J. and Pershan, P.S.

Interactions between light waves in a nonlinear dielectric
Phys. Rev. 127, 1918 (1962)

Bloembergen, N.

Nonlinear Optics

Benjamin, Reading, MA 1965

Born, M. and Wolf, E.

Principles of Optics

6th Edition, Pergamon, Oxford 1980

Byer, R.L. and Herbst, R.L.

Parametric oscillation and mixing

in "Nonlinear Infrared Generation", Y.-R. Shen, ed.,

Springer-Verlag, Berlin 1977

Dewey, Jr., C.F.

Nonlinear optical effects in rotationally-twinned crystals: an
evaluation of CdTe, ZnTe and ZnSe

Rev. Phys. Appl. 12, 4051 (1977)

Dewey, Jr., C.F. and Hocker, L.O.

Enhanced nonlinear optical effects in rotationally twinned
crystals

Appl. Phys. Lett. 26, 442 (1975)

Franken, P.A. and Ward, J.F.

Optical harmonics and nonlinear phenomena

Rev. Mod. Phys. 35, 23 (1963)

Giordmaine, J.A.

Nonlinear optical properties of liquids

Phys. Rev. 138, A1599 (1965)

Hocker, L.O. and Dewey, Jr., C.F.

Enhancement of second-harmonic generation in zinc selenide by
crystal defects

Appl. Phys. Lett. 28, 267 (1976)

Kurz, S.K., Jerphagnon, J. and Choy, M.M.

Nonlinear dielectric susceptibilities

in Landolt-Boernstein Numerical Data, Vol. 11, K.-H. Hellwege
and A.M. Hellwege, eds., Springer-Verlag 1979

- Maker, P.D., Terhune, R.W., Nissenoff, M. and Savage, C.M.
Effects of dispersion and focusing on the production of
optical harmonics
Phys. Rev. Lett. 8, 21 (1962)
- McMullen, J.D.
Optical parametric interactions in isotropic materials using a
phase-corrected stack of nonlinear dielectric plates
J. Appl. Phys. 46, 3076 (1975)
- Messiah, A.
Quantum Mechanics
Wiley, New York 1966
- Okada, M., Takizawa, K. and Ieiri, S.
Second harmonic generation by periodic laminar structure of
nonlinear optical crystal
Opt. Comm. 18, 331 (1976)
- Piltch, M.S., Cantrell, C.D. and Sze, R.C.
Infrared second-harmonic generation in nonbirefringent cadmium
telluride
J. Appl. Phys. 47, 3514 (1976)
- Schiff, L.I.
Quantum Mechanics
3^d Edition, McGraw-Hill, New York 1968
- Simon, H.J. and Bloembergen, N.
Second-harmonic light generation in crystals with natural
optical activity
Phys. Rev. 171, 1104 (1968)
- Singh, S.
Nonlinear optical materials
in Handbook of Lasers, R.J. Pressley, ed., CRC, Cleveland 1971
- Szilagyi, A. and Dewey, Jr., C.F.
Efficient infrared frequency doubling in rotationally twinned
CdTe
in Proc. 2nd Int. Conf. on IR Physics, E. Affolter and F.
Kneubühl, eds., Zürich 1979
- Szilagyi, A., Hordvik, A. and Schlossberg, H.R.
A quasi-phase-matching technique for efficient optical mixing
and frequency doubling
J. Appl. Phys. 47, 2025 (1976)
- Szilagyi, A., Hordvik, A. and Schlossberg, H.R.

Apparatus for producing efficient second harmonic generation
and frequency mixing
U.S. Patent 4,016,427, April 5, 1977

Thompson, D.E., McMullen, J.D. and Anderson, D.B.
Second harmonic generation in GaAs "stack of plates" using
high power CO₂ laser radiation
Appl. Phys. Lett. 29, 113 (1976)

Wynne, J.J. and Bloembergen, N.
Measurement of the lowest-order nonlinear susceptibility in
III-V semiconductors by second-harmonic generation with a CO₂
laser
Phys. Rev. 188, 1211 (1969)

Yacoby, Y., Aggarwal, R.L. and Lax, B.
Phase matching by periodic variation of nonlinear coefficients
J. Appl. Phys. 44, 3181 (1973)

van der Ziel, J.P.
Effect of Fabry-Perot interference on second harmonic
generation in a GaAs plate
J. Quant. Electr. QE-12, 407 (1976)

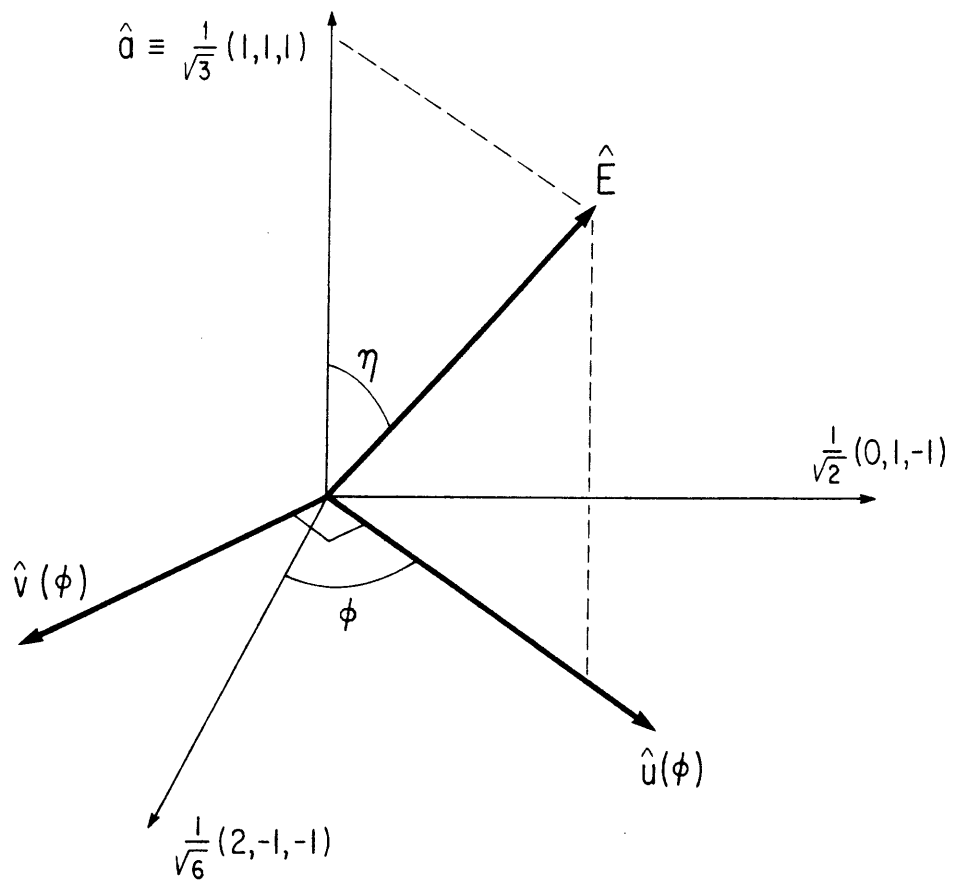


Fig. II.5.1 Crystal coordinate system and angle definitions

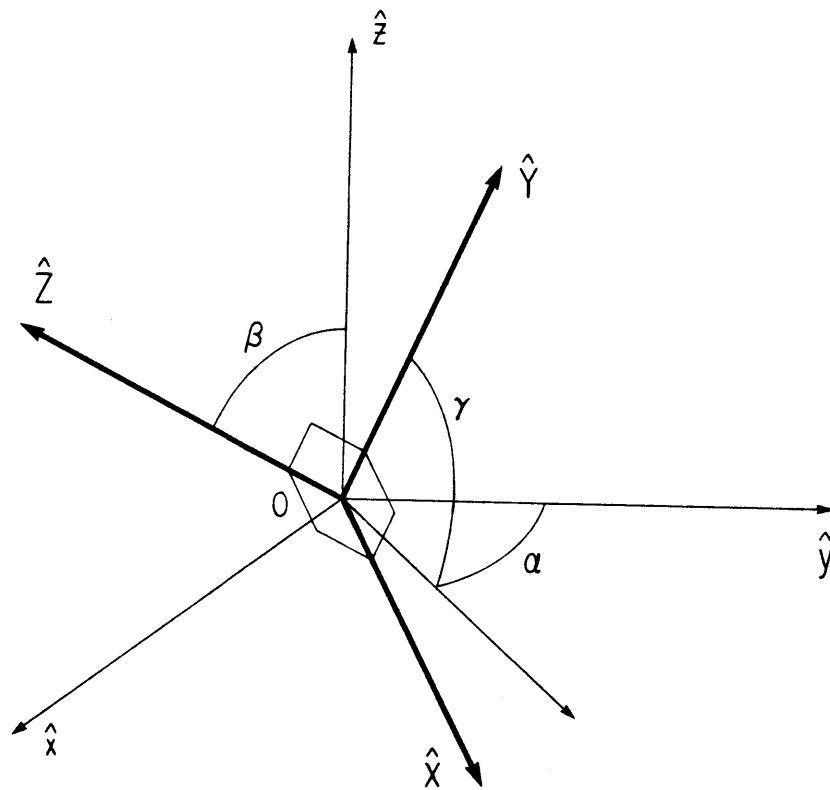


Fig. II.7.1 Euler angles (after Messiah 1966, Fig. XIII.1)

$$\vec{E}^{(1)}(r,t) = a \hat{u}(\phi) \cos(k_1 r - \omega t)$$

$$\vec{p}_{\text{rad}}^{\text{NL}}(r,t) = a^2 \sqrt{\frac{2}{3}} \hat{u}(-2\phi) \cos(2k_1 r - 2\omega t)$$

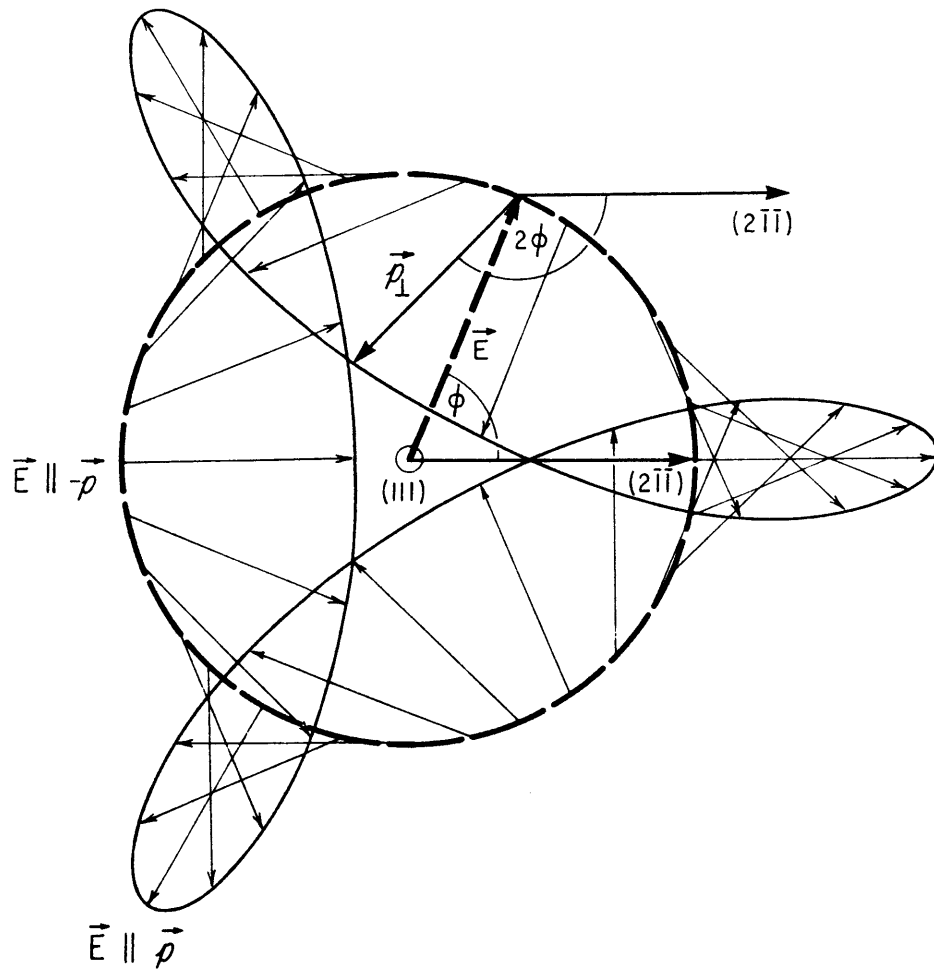


Fig. II.8.1 Relation between the fundamental (\vec{E}) and second harmonic (\vec{p}) polarizations for (111) propagation

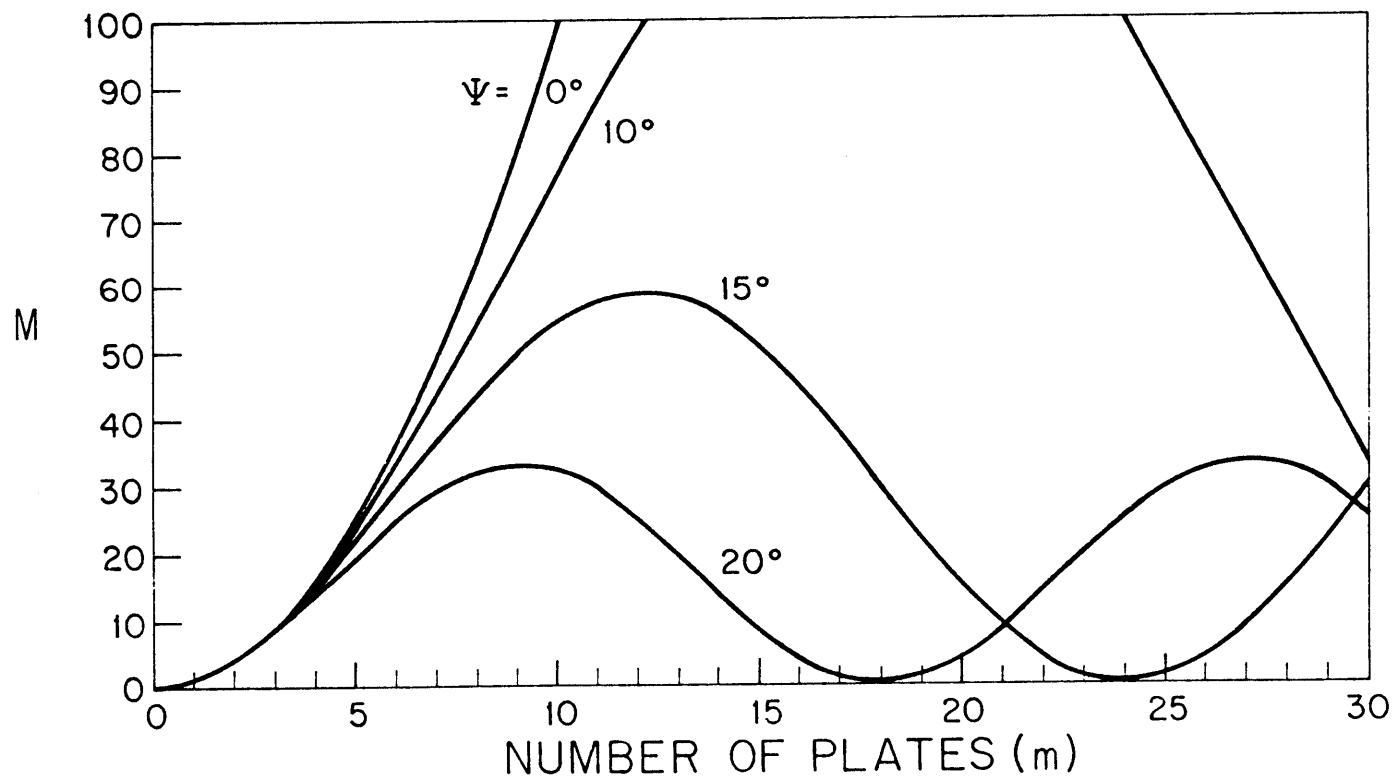


Fig. II.10.1a Effective number (M) of ideal plates vs. the actual number of optically contacted plates for various phase angles $\psi = 180^\circ \frac{r_d}{l_c}$

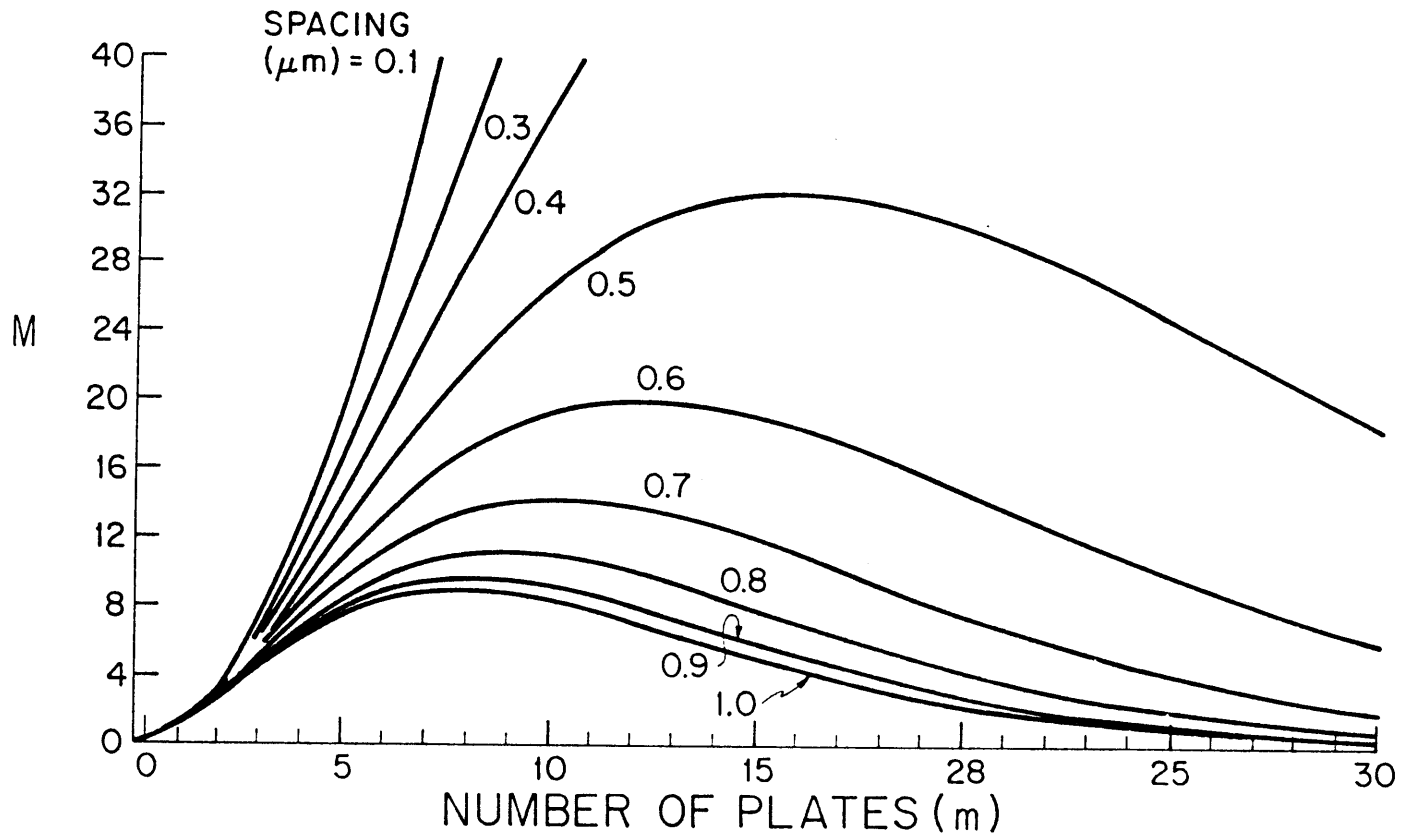


Fig. II.10.1b Effective number (M) of ideal plates vs. the actual number of coherence-length plates immersed in medium with $l_c = 29 \mu\text{m}$ for various spacings

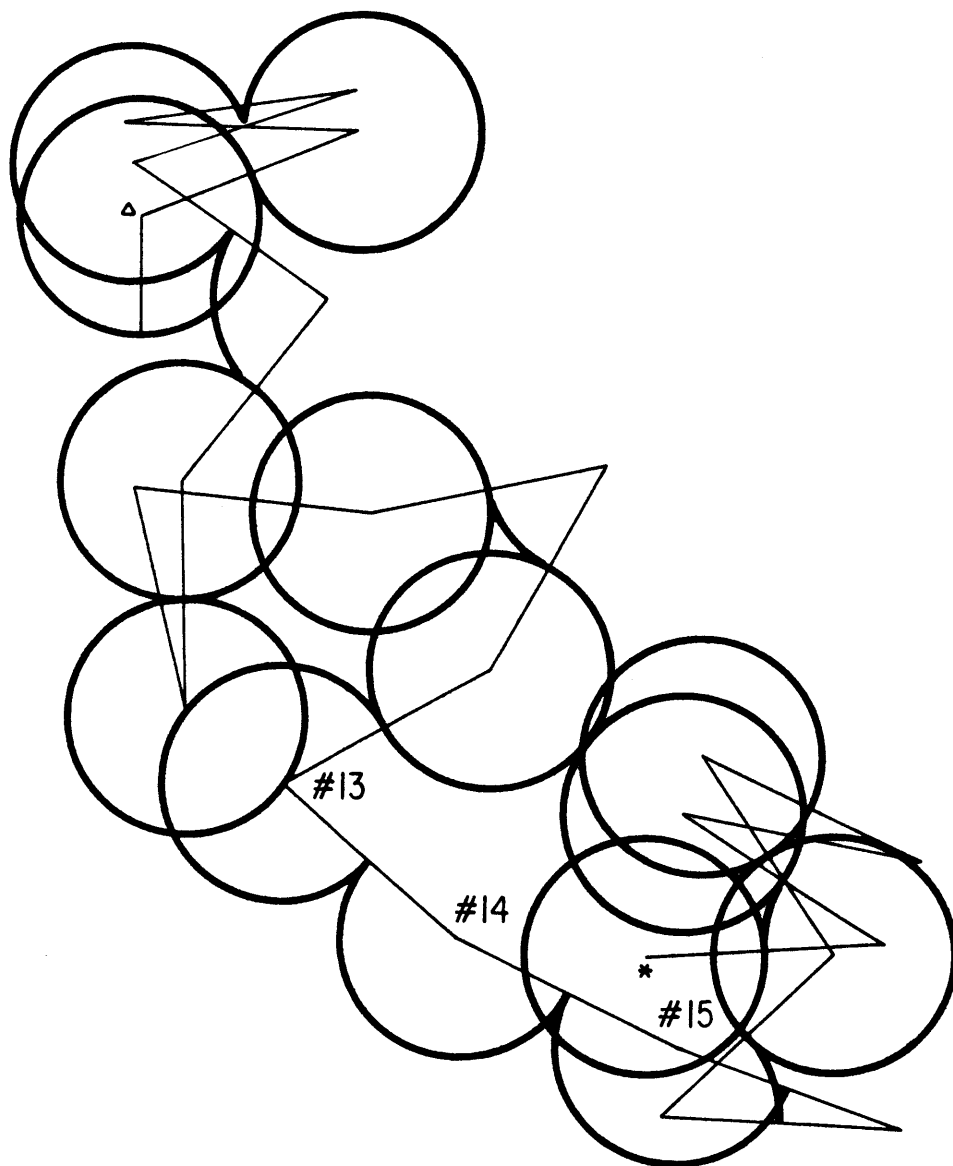


Fig. II.11.1a Argand plot of SH field in twinned crystal

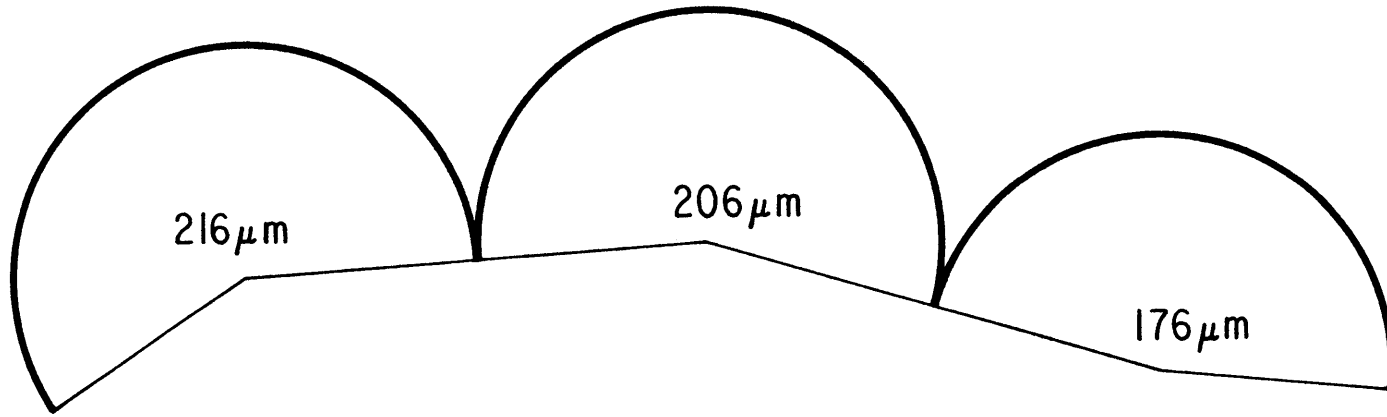


Fig. II.11.1b Argand plot for portion of the crystal selected for experiment

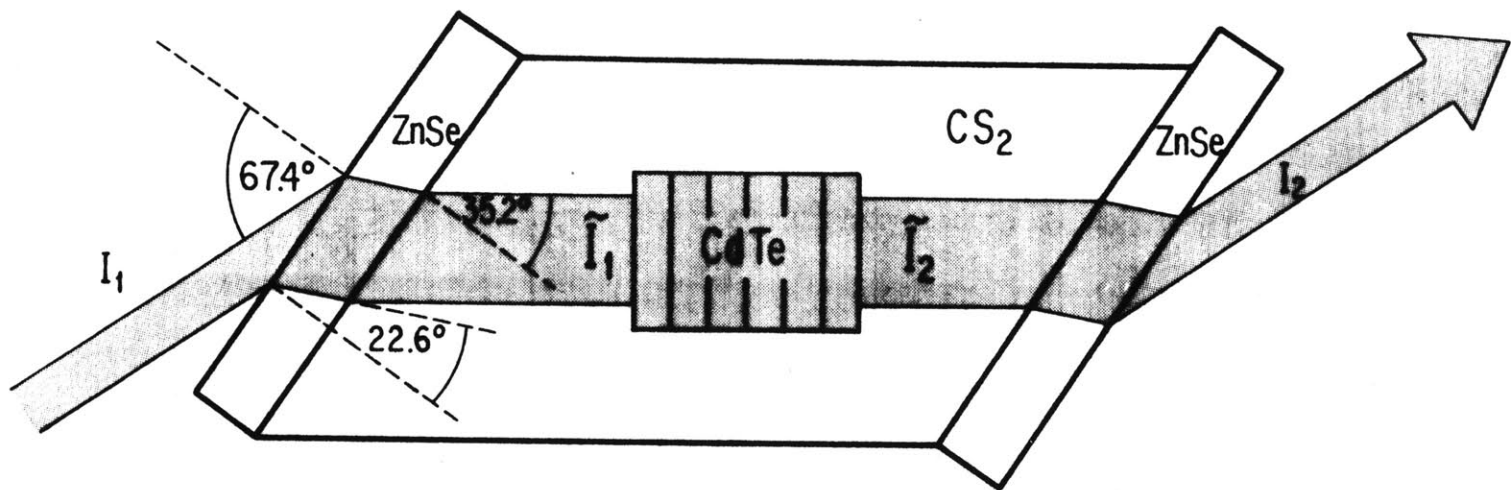


Fig. II.11.2 Brewster angle immersion cell (schematic)

Table II.7.1

\vec{A}	\vec{B}	$\vec{p}_{ }(\vec{A}, \vec{B})$	$\vec{p}_{\perp}(\vec{A}, \vec{B})$
\hat{a}	\hat{a}	$\frac{2}{\sqrt{3}} \hat{a}$	0
\hat{a} $\hat{\epsilon}_{\pm}$	$\hat{\epsilon}_{\pm}$ \hat{a}	0	$\frac{1}{\sqrt{3}} \epsilon_{\pm}$
$\hat{\epsilon}_{\pm}$	$\hat{\epsilon}_{\pm}$	0	$\frac{2}{\sqrt{3}} \hat{\epsilon}_{\pm}$
$\hat{\epsilon}_{\pm}$	$\hat{\epsilon}_{\mp}$	$\frac{1}{\sqrt{3}} \hat{a}$	0

CHAPTER III

Growth Twinning

III.1 Introduction

The primary stimulus for the study of growth twinning derives from the need for single crystals encountered by the electronics industry. Many applications of semiconducting materials including IC chips, substrates, detectors, electro-optic modulators, etc., rely for high performance on a monocrystalline matrix. In the more mature elemental semiconductors the requirement is consistently met. The situation is not as good in the case of the compound semiconductors, where twinning is still widely perceived as one of the major problems in crystal growth.

The other point of view, as seen in Chapter II, is that controlled twinning can be an asset in the production of efficient and economical frequency doublers and mixers. The materials of interest here are the noncentrosymmetric semiconductors of high nonlinear optical susceptibility, such as CdTe.

Following a review of published work relating to growth twinning we proceed in Section 3 to describe growth experiments on CdTe. The main experimental observations are then combined with others extracted from the literature and summarized in Section 4. The understanding thus derived and organized forms the basis for a model of the elemental semiconductor growth interface presented in Section 5. The intrinsic anisotropy featured in this model is then discussed and applied in Sections 6 and 7 to a variety of phenomena

including preferential etching, faceting and solitary and lamellar twinning. The restriction to elemental semiconductors is lifted in Section 8 where the dangling bond model of the interface is refined to include a polarity parameter. The model successfully accounts for a series of phenomena even though the analysis is not carried out in as much detail as in Sections 5 - 7. For the case of materials whose melts are not highly dissociated or metallic (such as CdTe), a clustering model of twinning is presented in Section 9, leading to provocative predictions for crystal growth. Sections 10 and 11 end the chapter with conclusions and proposals for further research respectively.

It should be noted that no completeness is claimed in the citation of published work. Also, due to space and time limitations, many related subjects had to fall outside the scope of the present research. For example no discussions of mechanical twinning, segregation phenomena and heat transfer (except indirectly, through the effect of a given interface morphology) have been included. It is hoped that these limitations will not materially detract from the usefulness of the ideas presented below.

III.2 Literature review

The crystallography and morphology of twinning in general and in the tetrahedrally coordinated semiconductors have been the subject of a number of early reviews: Aminoff and Broome 1931, Cahn 1954, Hartman 1956. Other works on the crystallography of twinning by Slawson 1950, Ellis 1950, Ellis and Treuting 1951, Ellis and Fageant 1954, Haasen 1957, Holt 1964 have all helped establish its pervasiveness and main characteristics.

For diamond and zincblende, growth twins were found to have octahedral habit (i.e. possess {111} composition planes). The twin operation could be described as a mirror parallel to the composition plane for the elemental semiconductors, but the operation which also remains valid for compound semiconductors crystalizing in the sphalerite (or zincblende) structure is a rotation of 180° about the (111) axis normal to the composition plane. Microscopically, twinning can be described as a stacking defect. Normal cubic stacking in a (111) direction is described as "staggered" because of the occurrence of three progressively offset double layers in each repeat distance along this direction. Denoting the position of each layer as A, B or C according to the amount of the offset, regular stacking could be symbolized by ...ABCABCABC.... Twinning corresponds to a reversal of the offset direction, as in ...ABCABACBA.... The immediate vicinity of the twin plane (...ABA...) is said to be stacked

in the "eclipsed" configuration, and may be regarded as the thinnest recognizable portion of the hexagonally packed wurtzite structure. Twin planes have very low specific energies (see e.g. Gottschalk, Patzer and Alexander 1978 and Hall and Vandersande 1978 for the closely related stacking fault energies) of the order of 10 ergs/cm^2 or 10 meV per bond crossed by the twin plane. This is due to the lack of a difference in coordination up to the second nearest neighbors for distances and up to the nearest neighbors for bond angles.

One of the common features of crystal growth in the conventional (111) direction is the presence of oblique twins (Wilkes 1959, Hulme and Mullin 1962, Steinemann and Zimmerli 1963, Vere, Cole and Williams 1983). Solitary as well as lamellar twins are commonly initiated at the edge of the crystal (three-phase boundary, or confining walls) and typically cross the entire boule at an angle of 19.5° from the growth axis (Billig 1954-'55, Mueller and Jacobson 1961, Vere, Cole and Williams 1983). The lamellar type is also commonly generated in the middle of the solid-melt interface (e.g. Hulme and Mullin 1962) when they must be accompanied by high energy grain boundaries.

Another type of twinning is at the center of the attention in dendritic, web and ribbon growth (e.g. Faust 1967, Seidensticker 1977, Dermatis, Faust and John 1965, respectively). In each case, the reason for the interest lies in the ability of centrally located twin lamellae to propagate unidirectionally and thereby generate extended (and sometimes

highly perfect) crystal structures.

A variety of possible causes have been cited for growth twinning in diamond-like semiconductors, including:

- i) - interface and seed orientation
- ii) - interface morphology and thermal environment
- iii) - stoichiometry and impurities
- iv) - growth rate and undercooling
- v) - faceting and - in the compound semiconductors - polarity.

i). A theoretical appraisal of the propensity to twinning was given by Billig (Billig 1954). It held that the likelihood of twinning increased with the degree of alignment of the resulting $\{111\}$ planes to the growth axis. Consequently, he found that a (100) seed was most likely to cause twinning.

A descending hierarchy of seed orientations vs. effectiveness in single crystal growth was given by Faust and John 1962 as (100)>(110)>(111) for elemental semiconductors (changed to (110)>(100)>(111) with molecular melts) and as (111)Sb, (211)>(311)>(100)>(110), (111)In by Hulme and Mullin 1962 for InSb.

It should be noted that much of the early work does not separate the effect of the seed orientation from the shape of the solid - melt interface.

ii). Planar interfaces have been found to be desirable for monocrystalline growth (Bolling, Tiller and Rutter 1956, Grabmaier and Grabmaier 1972, Nygren 1973). While studying

the dependence of twinning on seed orientation Steinemann and Zimmerli 1963 have also found increased twinning accompanying curved interfaces, but the dependence on seed orientation nearly disappeared when the boule diameter diverged by 45° or more.

The thermal environment is implicitly reflected in the interface morphology. In addition the crystal growth itself influences the thermal environment by means of the heat transferred and generated in the process. The very important issues relating to these mutual interactions fall largely outside of the scope of the present work.

iii). The chemical composition of the melt can influence the growth of crystals in more than one way. Impurities and departures from stoichiometry affect the position of the liquidus, hence the growth temperature. They also affect the energy and kinetics of lattice defects. For example, Bolling, Tiller and Rutter 1956 who found twin densities in Ge increase with the concentration of Ga dopant, also found decreased liquid-solid interfacial energy. Billig 1957 speculated that twinning in dendrites may be due to the incorporation of impurities. In GaAs, twinning on the As surface could be diminished or suppressed by raising the ambient temperature and with it the As partial pressure (Steinemann and Zimmerli 1963). It is not clear whether these authors were able to discriminate between the concentration effects and the possible attendant changes in interface morphology. Another indication that this is not at all a simple issue ensues from

the observation by Mueller and Jacobson 1961 of a lack of dependence of InSb growth on impurities, although some of the discrepancies might be explainable by the incompatibility of the various experimental set-ups.

iv). Information relating to the dependence of twinning on growth rate is scarce. However, Bolling, Tiller and Rutter 1956 reported an inverse relation between twinning frequency and the ratio (G/R) of the thermal gradient and the growth rate. Assuming that the kinetic undercooling (or supersaturation, for solution growth) just ahead of the solidification front increases with the growth rate, then a similar dependence on the latter can be inferred from Buerger's work, over ten years earlier (Buerger 1945). A calculation of twinning probability as a function of supersaturation, undercooling and twin plane energy was performed by Däweritz 1972 for the elemental and II-VI semiconductors, assuming an accidental (see below) type mechanism.

v). One consequence of the directional nature of covalent bonding in the tetrahedrally coordinated materials is the strong anisotropy of growth kinetics. Particularly substantial nucleation barriers must be surmounted for growth in (111) directions, resulting in increased lag (undercooling) behind the freezing point isotherm. The resultant flattening of the solid-melt interface is commonly termed faceting, and has been shown to be more pronounced in materials with higher entropy of fusion (e.g. Jackson PSSC 1967). The related

technologically important anisotropic segregation of impurities or dopants falls outside the scope of this thesis.

A number of authors have made the connection between the dependence of twinning on undercooling and faceting. For example, Wilkes 1959, Hulme and Mullin 1962, Mullin 1962 have all pointed out the apparent connection between peripheral facet formation and twinning. Unfortunately, more often than not reliable interface morphology data was not available, and when it was, it did not support the idea of an $\{111\}$ oblique facet as the site for oblique twin nucleation. Further discussion of faceting appears below in Section III.6 for the diamond lattice and in Section III.8 for the polar semiconductors.

We can summarize the types of mechanisms which have been invoked to explain growth twinning as belonging to one of two general categories:

- a). thermally determined or constrained twinning.
- b). growth accident or random twinning

The former, arguing for the alignment of a favorable crystalline axis with the local thermal gradient, will be developed and applied in Sections 5 through 8 as the preferred mechanism, under the name of the Dangling Bond Model. The latter will find an example in the Clustering Model of Section III.9.

III.3 Experimental program

3.1 Description of system

For this phase of the study we used a vertical resistive heating furnace made by Marshall Products Co., Columbus, Ohio (Fig. 3.1), with maximum ratings of 1315°C, 25 V, 48 Amps. Due to the age of this furnace, a 22 V ceiling is observed for safety. A water cooled stainless steel shaft (manually or automatically movable) supports the growth assembly (Fig. 3.2). The latter is wholly enclosed in a quartz process tube and allows the use of either vacuum or an inert gas (Ar) atmosphere to protect the graphite extension rods and crucible holder from oxidation as well as insulating the work environment in case of ampoule failure. Up to five thermocouples may be used simultaneously to monitor the interior of the process tube.

Furnace temperature regulation is accomplished manually or automatically using a Leeds and Northrop C.A.T. Controller. Furnace temperature is monitored by a platinum - 10% rhodium vs. platinum thermocouple, referred to an Ice Point Reference Standard by Joseph Kaye and Co., Inc., Cambridge, MA. The same ice point system is used for the Chromel - Alumel thermocouples used inside the process tube.

3.2 Processing steps

For the actual growth we used "ultra pure" (99.99 %) polycrystalline CdTe pieces, manufactured by Alpha Products,

Thiokol / Ventron Division, Danvers, MA, and by II-VI, Inc., of Saxonburg, PA, at the rate of about 50 grams per experiment. Before loading, the charges were etched in a 5% bromine - methanol solution, gradually diluted to electronic grade methanol, boiled in this methanol, boiled in de-ionized water and dried in an evacuated dessicator. Ampoules were made and sealed by Wilfred Doucette from 16 mm I.D., 2mm wall tubes, supplied by Quartz Plus, Inc., Watertown, MA. Two types of treatment of the inner ampoule walls were tried: sandblasting followed by soaking in Aqua Regia, and etching in a dilute HF solution (starting with 10 H₂O : 1 HF and ending with 3 H₂O : 1 HF by volume). No conclusion can be drawn about the relative merits of these methods although etching appears to be intrinsically cleaner.

Typically a loaded ampoule was connected to a vacuum system via a graded seal, a cold trap and a three way stopcock. The remaining passage through the latter was used to repeatedly (three to five times) flush the ampoule with high purity argon (99.999%). The vacuum was usually supplied by a 4" Varian 3305 mobile high vacuum diffusion pump (courtesy of Dergao Lin). After evacuation the ampoules were sealed by shrinking around a solid quartz plug covering the CdTe charge. Following the growth, extraction of the boules was usually accomplished by ampoule dissolution in concentrated HF (48 %) which does not appear to adversely affect CdTe.

3.3 Characterization

The characterization means employed fall broadly in four categories, depending on the kind of probe used:

a. Non-destructive

i). Photons

ii). Electrons

b. Destructive

iii). Chemical etch followed by (i) or (ii)
(surface)

iv). Chemical analysis (bulk)

In order of decreasing wavelength (i) includes:

- Infrared photography: unfortunately, no IR viewer responding beyond 2 μm was available.

- Macro and micro-photography in the visible range. Using a Polaroid MP-3 Land Camera and a Leica Tessovar 35 mm set-up (courtesy of Prof. A. F. Witt) a variety of features were recorded, including external morphology, phase separation lines, voids due to bubble formation, ridges or grooves corresponding to grain boundaries or lamellar twins. Except for the external shape, these and smaller features were seen in greater detail on the Reichert optical microscope, especially using the Nomarsky interference attachment.

- X-rays. Laue back-reflection on a Norelco machine was used to reveal the crystallinity of samples by the sharpness and position of diffraction spots.

Included in (ii) are:

- SEM. Two different machines were used an AMR 1000A and a Cambridge SEM. Back-scattering and secondary electron

emission modes were used to show micro-morphological surface detail. X-ray dispersive analysis gives major elemental constituents and X-ray elemental maps show phase separation and interface breakdown configurations.

- TEM. (courtesy of James Nakos). This method has revealed dislocation loops, micro-precipitates and other assorted microscopic imperfections. In electron diffraction mode, Kikuchi lines were used to ascertain a relatively high degree of crystalline perfection.

A grain-revealing etch (iii) was used very successfully in conjunction with (i) and (ii). The composition is 1 HF : 3 HNO₃ : 4 (2% by weight aqueous AgNO₃ solution) (Mullin and Straughan, 1977) and is used for 10 to 30 sec.

- Macro and micro-photography. This etch produces strikingly sharp contrast between adjacent grains and was repeatedly recorded on the MP-3 camera. On polished or fractured surfaces, triangular dislocation pits are revealed.

- TV image analysis. Using a Hamamatsu C1000 Vidicon measurement system connected to a MINC-23 computer, lamellar twin spacing data was acquired from enlarged prints of etched material.

- SEM. Etched samples have clearly shown that differently oriented microfacets are responsible for the observed contrast across a twin or grain boundary.

The chemical analyses (iv) (courtesy of Walter Correia of the Strnad Spectrographic Laboratory) performed by emission and absorption spectroscopy have given bulk stoichiometry and

impurity information complementary to that obtained by X-ray dispersive analysis.

3.4 Highlights of growth experiments

The following four pieces of work are discussed below:

- i). Boric oxide encapsulation
- ii). Curved ampoule
- iii). No wetting run
- iv). Single crystal run

i). A sealed, vertical Bridgman charge was successfully encapsulated with B_2O_3 . The encapsulant was interspersed among the CdTe charge pieces. The growth assembly was lowered from the hot zone at $3 \mu\text{m}/\text{sec}$. Despite the failure of the quartz ampoule due to the build-up of thermal stresses during the last stages of cooling, the CdTe boule was not damaged and revealed (Fig. 3.3a) a smooth, shiny convex "meniscus" (last to freeze portion). The portion of encapsulant adjacent to the smooth, concave crystal-glass interface appeared cloudy but became clear about one centimeter higher (away from the interface). This observation was made just before the ampoule failed. Spectrochemical analysis (see 3(iv) above) of B_2O_3 samples taken from near and away from the interface showed low Cd concentrations of .07% and .04% respectively. X-ray Laue back reflection from "meniscus" of boule shows a concentric ring pattern similar to powder diffraction (Fig. 3.3b). Under 1000X SEM magnification (Fig. 3.3c) and after the grain revealing etch (section 3(iii) above), this "meniscus" appears

as a jagged, cracked, almost glassy surface. In X-ray dispersive mode (Fig. 3.3d) the composition of the surface is seen to be almost pure tellurium, apparently segregated as excess in the last to freeze portion. But 2 mm below the top the material is ordinary twinned CdTe (Fig. 3.3e after etching). At higher magnification (1100X) the reason for the contrast across the twin boundaries is seen to be the preferential etching of microfacets on a scale of several microns (Fig. 3.3f), sufficiently large to give specular reflection in different directions from one domain to the next. The same boule in as-grown (before etching) condition displayed (Fig. 3.3g) a pattern of ridges and grooves on its vertical surface apparently associated with lamellar twinning.

ii). Observing twin configurations over a number of growth runs, a pattern began to emerge suggesting a dependence of twin plane nucleation on the configuration of the "three-phase" (solid-melt-wall) region. To further study this dependence, an asymmetric ampoule was designed and a suitably shaped graphite mandrel (Fig. 3.4a) machined for it. The quartz ampoule was then moulded over this mandrel by Wilfred Doucette. The asymmetry would ensure that whatever the exact mechanism of twinning, it start acting predominantly on one side of the ampoule, with the twins subsequently propagating across the boule. The growth run succeeded. Figures 3.4b and c, show one major family of lamellar twins (with etching contrast) initiated at a grain boundary, and extending through most of the boule except near the top where the ampoule

curvature was different in order to accommodate a larger, relatively loosely packed charge. The experiment demonstrates the determining influence the thermal field has on twinning. Note that the unusual geometry was also responsible for stressful cooling, hence the abundance of thermally induced cracks.

iii). Wetting of the quartz ampoule by the CdTe charge was avoided in a growth experiment, without sandblasting the wall or covering it with pyrolytic graphite. The following precautions were taken for the charge preparation:

- The charge consisted of longitudinally cut cylinders from an earlier run, resulting in a reduced surface to volume ratio, and unused volume in the sealed ampoule.

- Prior to this experiment charges were etched in a 2% bromine in methanol solution. Beginning with this run, a 5% solution has been employed.

- Before sealing, the ampoule was evacuated to 1.5×10^{-6} torr.

A feature of this experiment whose utility has not been proven was a cylindrical nickel shield around the ampoule support structure, extending up into the furnace to about 1/3 of the height of the ampoule. The idea was to decrease the amount of lateral heat transfer between the furnace and the growing solid in order to decrease the presumed concavity of the solid melt interface.

Another feature which may have interfered with the one above, was an attempt to study the dependence of twinning on

the growth rate. This was done by repeatedly and suddenly changing the lowering rate. The result unfortunately is inconclusive. The etched longitudinal section in Fig. 3.5 shows a large number of nearly parallel grain boundaries originating about half way up a large single matrix. It is entirely conceivable that in the absence of this feature, the experiment would have yielded a (nearly) single crystal.

iv). Figure 3.6a shows an etched nearly single crystal grown in the same system. Due to the fact that the charge was prepared before that of the experiment described above, it used the old bromine - methanol etch concentration. Consequently, in spite of using the same quality of vacuum before sealing, this boule once again wetted the ampoule and had to be extracted by means of dissolution in HF. Among the factors probably contributing to the good crystallinity:

- Relatively low pulling rate: $0.5 \mu\text{m}/\text{sec} = 1.8 \text{ mm}/\text{hr.}$
- Axial gradient of $16 \text{ deg}/\text{cm} \pm 7\%$, determined by using two thermocouples near the top and bottom of ampoule.
- The use of the same nickel shield as in the 4/15 run.

I would also cite as a favorable circumstance the use of precast (previously grown in same size ampoule) material whose last to freeze portion had been removed. For this run, the amount of excess tellurium segregated on the "meniscus" was reduced to a small frozen droplet barely visible in the above figure.

To document the crystallinity of this boule, Fig. 3.6b

(courtesy of James Nakos) shows a TEM electron diffraction pattern of sharp spots and distinct Kikuchi lines.

III.4 Summary of observations and propositions

From the experiments and the literature previously discussed there emerged the following consistent pattern of observations applicable to the tetrahedrally coordinated semiconductors.

Morphology of twinning:

- Twins are the most common type of grain boundary (G.B.)
- Among them the oblique type dominates
- Oblique twins persist over long distances (stabilizing effect)

- Solitary twins are initiated at an external surface
- Lamellar twin "patches" may be externally or internally bounded

- Within a "patch" twin spacing appears nearly periodic
- Internal lamellar "patches" emerge from G.B.'s
- Single lamellae can originate at the center of the interface

Other observations:

- Growing crystals will twin so as to align an "easy" growth direction with $\vec{v} T$

- $TPE \sim SFE \ll GBE$

- During crystal growth the atoms in each layer will have had an enormous number of opportunities to test various configurations before arriving to the final position (see Appendix A1 for an estimate of the sticking probability).

Consideration of these observations has led to the

adoption of the following propositions as the basis of the models of growth twinning in subsequent sections:

i) - A single crystal will grow to reduce the kinetic undercooling ahead of the solid - melt interface.

There are two avenues for reducing the kinetic undercooling:

1 - increase growth rate; limited for a given pull rate by the subsequent reduction in driving force, resulting in some steady state balance.

2 - expose a new crystallographic surface to the melt, with a higher density of dangling bonds or (see section III.11) a smaller nucleation barrier.

ii) - A defective crystal will tend to eliminate growth defects such as high energy G.B.'s .

If the geometry is such that a high energy grain boundary can be replaced by a coherent twin (section III.7) this will happen at least temporarily. In the long run the growth kinetics before and after the twinning operation must also be included in the balance.

In Sangster's terms (Sangster 1962), crystal growth in these materials is largely (but see the next paragraph) constrained by the applied thermal field. Moreover, at each point on the solidification front the crystal has an additional discrete degree of freedom with five values, namely the choice between the current orientation or twinning about one of four tetrahedral directions. This local degree of freedom may be suppressed when crystallography requires that it

be accompanied by a high energy boundary. Conversely, when the driving force is sufficiently high, the exercise of this freedom will lead to polycrystalline breakdown, in some cases long before any breakdown associated with the presence of impurities and phase separation.

The properties of the crystalline lattice are also manifested in anisotropic kinetics of growth, of which faceting on {111} planes (Lewis 1975) is a particularly pervasive example (see Section III.2). It is precisely this anisotropy which activates the twinning degree of freedom.

As a first approximation we propose that the microscopic growth rate is a monotonically increasing (perhaps linear) function of the density of dangling bonds.

III.5 Dangling bond model of the growth interface

The calculation of the density of dangling bonds as a function of interface orientation (in effect a γ plot) depends on the following simplifying assumptions:

- i) - all bonds sp^3 hybridized
- ii) - no surface relaxation or reconstruction
- iii) - no polar effects
- iv) - all orientations decomposed into $\{111\}$ and $\{100\}$ type steps

We are therefore limiting the calculation to a tetrahedrally coordinated semiconductor-vacuum interface at 0°K .

The calculation begins by considering a family of interfaces whose normals lie in the zone of (are perpendicular to) a (110) type axis. Figure 5.1a gives a perspective drawing of the first coordination tetrahedron, while 5.1b shows the same projected onto the $(\bar{1}10)$ plane whose positive normal points into the paper.

A typical interface normal in the $(\bar{1}10)$ zone is of the form (iik) . In the six angular ranges of Fig. 5.2 such an interface is made up of only two kinds of steps, except at the extremes of these ranges where the interface is smooth and made up of only one kind of step. The drawing indicates schematically the number of dangling bonds each step contributes. It is seen that in the ranges II and II' there are only single bond contributions because only $\{111\}$ type steps are present. In the four type I ranges $\{001\}$ steps are

also found, each contributing two dangling bonds.

We now calculate the periodic area of the interface as the vector sum of the appropriate number of steps of each kind. In region I with n steps of type $\{\bar{1}\bar{1}1\}$ and m steps of $\{001\}$ type in each repeat distance, we obtain an area \bar{A}

$$\frac{\bar{A}}{d^2} = n \frac{\sqrt{3}}{2} \left[\frac{1}{\sqrt{3}} (1\bar{1}\bar{1}) \right] + m (001) \quad (5.1)$$

where we have used the widths of a $\{\bar{1}\bar{1}1\}$ step ($\sqrt{3}d/2$), of a $\{001\}$ step (d), and the depth of the layer (d), all obtained from the values shown in Figs. 5.1.

Equation 5.1 can be immediately simplified to

$$\bar{A} = \frac{d^2}{2} (\bar{n}, \bar{n}, 2m+n) \equiv |\bar{A}| \hat{n} \quad (5.2)$$

which is obviously of the (iik) type, as required. Since each $\{001\}$ step contributes 2 dangling bonds while each $\{\bar{1}\bar{1}1\}$ step contributes 1 bond, the density of dangling bonds \mathcal{N} is

simply
$$\mathcal{N} = \frac{2m+n}{\frac{d^2}{2} |(\bar{n}, \bar{n}, 2m+n)|} = \frac{2}{d^2} \frac{\bar{A} \cdot (001)}{|\bar{A}|}$$

or

$$\mathcal{N} = \frac{2}{d^2} \hat{n} \cdot (001) \quad (5.3a)$$

where \hat{n} is the unit interface normal. Symmetry will dictate the same result for region I' while in regions I'' and I''' we obtain

$$\mathcal{N} = \frac{2}{d^2} \hat{n} \cdot (00\bar{1}) \quad (5.3b)$$

The argument is much the same for region II. With m $\{111\}$ steps and n $\{1\bar{1}\bar{1}\}$ steps the area is

$$\frac{\bar{A}}{d^2} = \frac{1}{2} (m+n, m+n, m-n) \quad (5.4)$$

Since each step contributes only one bond, the density \mathcal{N} is

$$\mathcal{N} = \frac{m+n}{|\bar{A}|} = \frac{2}{d^2} \frac{\bar{A} \cdot (110)}{|\bar{A}|} = \frac{2}{d^2} \frac{1}{\sqrt{2}} \hat{n} \cdot \left[\frac{1}{\sqrt{2}} (110) \right] \quad (5.5)$$

However we must recall that the (110) zone is but one of six

such zones (disregarding overall sign) and that the symmetry of the lattice will require the same functional form around axes of high symmetry such as (111). It therefore makes much better sense to rewrite Eq. (5.5) as

$$\mathcal{N} = \frac{2}{d^2} \hat{n} \cdot (100) = \frac{2}{d^2} \hat{n} \cdot (010) \quad (5.6)$$

We are thus led to the conclusion that the entire angular dependence can be written as

$$\mathcal{N} = \frac{2}{d^2} \hat{n} \cdot (\pm \hat{x}_i) \quad (5.7)$$

where $\pm \hat{x}_i$ is the closest of the cubic directions.

This remarkably simple result was checked by repeating the process for interface normals in the (001) zone. Inasmuch as the details shed no new light on the subject, they will not be repeated here.

As a three dimensional object, this function may best be visualized by imagining 6 interpenetrating spheres of diameter $2/d^2$ whose centers lie on the face centers of a cube of edge $2/d^2$. Figures 5.3a, b, and c show cross sections of this function perpendicular to the (001), $(\bar{1}10)$ and (111) directions respectively. Another way to visualize this function is as constant density contours in a stereographic projection (Figs. 5.4a and b).

When interpreted as a solid-vacuum interfacial energy with each dangling bond carrying a fraction of the appropriate latent heat per atom, this result is entirely consistent with the work of Herring who in 1951 showed that such γ plots have to be composed of sections of spheres (Herring 1951).

For the diamond lattice Mackenzie and Nicholas 1962 have

previously calculated the number of bonds of various kinds cut by a plane of varying orientation. Unfortunately, due to the occurrence of singly bonded atoms at such an "unstepped" surface, their result is not directly related to the present work.

In connection with the above results, it is worth noting that high index directions correspond with highly corrugated "hill and valley" structures. Nevertheless the contribution to the dangling bond density is no more than that given by the individual steps. There remains some leeway in the arrangement of steps in such a direction: all the steps of one kind could be bunched together giving a deeply grooved surface, or the two kinds of steps could be interspersed resulting in a smoother interface. In the absence of step-step interaction energies we cannot derive the choice. But common sense dictates that given the latitude, the crystal will conform as closely as possible to the melt isotherm, which leads to the choice of the smoother interface (of the same average density of dangling bonds and repeat distance).

We have seen at the beginning of this section that the calculation assumes a temperature of 0°K. There is good reason to suspect however that even at the melting point enough features of the density of bonds remain to preserve the usefulness of the model. External morphological aspects of melt grown crystals often include clear anisotropies such as faceting, dendritic growth or growth twinning which, as we will see in the next three sections, provide ample

justification for this approach.

III.6 Supporting evidence and applications of the dangling bond model

A striking confirmation of the density of dangling bonds calculation can be found in the etching of spherical crystals of elemental semiconductors. In such experiments, the ultimate shape is expected to consist of facets with the fastest etch rate. Figure 6.1 shows the result obtained by Lee on a silicon sphere (Lee 1969). The fastest directions are of the (001) type with the rate gradually decreasing towards the octahedral directions. The etch rate can clearly be correlated with the density of dangling bonds shown in Fig. 5.4a. A similar result was obtained by Ellis with germanium spheres. Even though he was able to obtain other forms with various concentrated etches, in the limit of low dilution all of his etchants yielded cubic forms (Ellis 1954). A direct correlation between etch rate and bond density in Ge was also noted by Gatos and Lavine 1965.

The idea of "easy" and "difficult" growth directions in an {111} plane was convincingly explained by Billig 1955 and Barber and Heasell 1965 in terms of the initiation of new rows of atoms at {111} steps. In terms of the density of dangling bonds the explanation is automatic with reference to Fig. 5.4b. The lateral growth of steps may be thought of as the slight deviation of the interface orientation from the (111) direction (i.e. a vicinal surface). The lateral growth rate is seen to change continuously with the direction of tilt.

Deviations toward a (001) type lobe corresponds to steps advancing in an "easy direction. Conversely, the difficult directions result from tilting toward the nearest octahedral directions. The influence of a proximal (001) type axis on the growth of {111} steps was also recognized by Miller and Witt 1975.

Another way to see the anisotropy of growth kinetics is to look at interface demarcation studies of twinned crystals. As will also be shown below, after an oblique twinning operation the dangling bond density will increase, resulting in transiently higher growth rate and a cusp in the interface at the twin boundary (Fig. 6.2). Such cusps were in fact seen by Witt and Gatos 1967 and by Miller and Witt 1975 in twinned InSb.

Faceting on {111} planes is well known in tetrahedrally coordinated semiconductors. It may be understood kinetically as follows. Assume that the growth rate is proportional to \mathcal{N} .

For an interface normal $\hat{n}(\theta)$ making an angle θ with the {111} direction (\hat{n}_0), the axial component is proportional to $(\hat{n} \cdot \hat{x})(\hat{n} \cdot \hat{n}_0)$. The function f defined as the ratio of this component to the (111) rate is

$$f(\theta) = \frac{[\hat{n}(\theta) \cdot \hat{x}][\hat{n}(\theta) \cdot \hat{n}_0]}{\hat{n}_0 \cdot \hat{x}} = \frac{\cos(\theta_0 - \theta) \cos \theta}{\cos \theta_0} \quad (6.1)$$

This function has a maximum of $(1 + \sqrt{3})/2 = 1.37$ at $\theta = \theta_0/2 = 27.4^\circ$ and equals 1 at the two extremes 0° and 54.7° . The result: for equal undercooling, all interfaces of orientation intermediate between (111) and (100) will tend to grow faster and catch up to the {111} facet. The process is

self-limiting: the closer the orientation the smaller the rate difference. (N.B.: Naturally the undercooling will not be the same at different points of the interface, but will rather be determined self-consistently by the combined effects of the applied thermal field, the imposed pull rate and the lattice anisotropy. Nevertheless, a qualitative understanding may be gained from the present considerations.) For $\theta > \theta_0/2$ the effect is also diminished since f is approaching unity. At θ_0 the axial rate of that interface is precisely equal to that at the center of the facet. Thus the angle of tilt would tend to decrease if initially less than 54.7° and increase if the reverse were true, leading to a potentially abrupt change in interface tilt beyond this angle. In that case an external "facet" would form appearing as a flattened outside surface and suggestive of the action of a so-called "divergent" facet. Of course, to have the actual divergent facet be a part of the local solid-melt interface would require an angle of tilt of 109.5° , which, with the exception of unusually severe "shouldering", would not be achieved.

Tilting now toward the "difficult" (011) direction (which, projected in the {111} plane would point along the $(\bar{2}11)$ direction), the function f becomes

$$f(\theta) = \frac{[\hat{n}(\theta) \cdot \frac{1}{\sqrt{2}}(011)] [\hat{n}(\theta) \cdot \hat{n}_0]}{\hat{n}_0 \cdot \frac{1}{\sqrt{2}}(011)} = \frac{\cos(\theta_1 - \theta) \cos(\theta)}{\cos \theta_1} \quad (6.2)$$

This function has a $(\sqrt{2} + \sqrt{3})/2\sqrt{2}$ maximum at $\theta = \theta_1/2 = 17.6^\circ$. As before the angle of tilt will tend to decrease if initially less than 35.3° and increase if the reverse were true, resulting in the appearance of flattened exterior surfaces

suggestive of the action of the so-called "convergent" facets. To have the actual convergent {111} facets be part of the interface would require a tilt angle of 70.5° which is not often realized in practical melt growth.

If we now compare the axial component of the growth rate at diametrically opposed points on the solid-melt interface, we find that it is greater in the "easy" directions even after the second triplet of external "facets" sets in (for $\theta > 54.7^\circ$). Figures 6.3b, c and d show the qualitative external faceting behavior in pulling from the melt as a function of interface tilt at the periphery (angle θ in Fig. 6.3a). All three types of boule cross sections are seen experimentally in the elemental semiconductors. Facet formation in crystals with convex growth interfaces was previously pointed out by Mullin 1962.

A major application and the primary reason for this investigation is the exploration of growth twinning. We limit for now consideration to the solitary (or isolated) type.

For a {111} seeded crystal Fig. 5.4b showed the density of dangling bonds as a function of interface orientation. Because of {111} faceting (discussed above) a major portion of the interface is in fact coincident with a {111} surface. With this orientation it is obvious that twinning on this facet would not at all increase the density of dangling bonds and it is therefore an inappropriate response to undercooling (recall that the twinning operation is conveniently represented as a 180° rotation around the {111} axis, hence the

term rotational twinning). On the other hand, an oblique twin will definitely increase this density as can be seen from the composite of Fig. 6.4, where the rotation axis was chosen to be $(\bar{1}11)=(1\bar{1}\bar{1})$. Note that in this figure for each orientation only the highest density surface is shown, whether that be of the original or of the twinned crystal. After the rotation the nearest (100) type lobe to the original growth direction is the $(\bar{1}00)'$ which is located at $1/3(122)$ in the unrotated system, as can be seen from Appendix A2. The new \mathcal{N} relative to the original one is

$$\frac{\mathcal{N}'}{\mathcal{N}} = \frac{2 \frac{1}{\sqrt{3}}(111) \cdot \frac{1}{3}(122)}{2 \frac{1}{\sqrt{3}}(111) \cdot (100)} = \frac{5}{3} \quad (6.3)$$

Thus if the microscopic rate were proportional to \mathcal{N} and to the kinetic undercooling, the latter would diminish by 40%.

If the twin plane energy is negligible, we already have a kinetic explanation of oblique twinning at any growth rate. With a finite TPE, (111) growth will remain stable up to a growth rate threshold. At higher rates, kinetics once again wins out over energetics and the oblique twin is activated.

The crystallography of oblique twinning is such that it can only occur at the edge of the interface. Otherwise it would be accompanied by a high energy grain boundary which would require a far higher driving force to overcome. The relative stability of a (111) seeded crystal against twinning can then be understood as resulting from the rather low kinetic undercooling likely to be present near the curved periphery of the interface.

Consider now a (001) seeded crystal (Fig. 5.4a). There

are four potential twinning axes at 54.7° from the growth direction. One of these twinning operations is shown in Fig. 6.5. It is obvious that this is no more than a different view of the situation in Fig. 6.4. It is also apparent that no twinning operation can increase \mathcal{N} beyond its $2/d^2$ maximum at (001).

The prediction is then that there will be no twinning in a crystal whose solidification front coincided everywhere with a {001} type surface. The restriction can be relaxed to include the entire range of orientations where the bond density could not be surpassed by any twinning operation. This range is shown in Fig. 6.6 as an octogonal cap on a three dimensional multiply composite surface. A solid-melt interface with a normal in this range would never twin according to this model, regardless of growth rate or TPE. Moreover even neighboring orientations may not twin below a certain growth rate (directly related to the TPE).

Taking this analysis to its logical conclusion, we wish to find the most probable twinning operation for each interface orientation. Fig. 6.7 associates each interface orientation with the twinning axis yielding the highest dangling bond density, or with an unconditionally stable region. The active planes are shown in this stereographic projection as the zones of the corresponding twin axes. Note that in the neighborhood of the (111) axis, tilting the interface towards a "difficult" direction (which, as discussed above, leads to the formation of a "convergent" facet when θ

>35.3°) may result for $\theta < 35.3^\circ$ in an oblique twin of the type previously thought to occur by accidental 2-dimensional nucleation at a point on an actual oblique {111} facet near the 3 phase region.

It is now clear that most solitary oblique twins do originate at the edge of the growing crystals. But the misoriented 2-dimensional nucleation mechanism on a (111) oblique surface cannot be applicable without the actual occurrence of such an interface orientation. Moreover, as the preceding argument shows, kinetic (and energetic) considerations are sufficient to account for the morphology of solitary twinning in elemental semiconductors, rendering growth accidents unnecessary. This is not to say however that heterogeneities of a chemical, mechanical or thermal nature cannot lead to twinning. But it is one of the important results of this thesis that the intrinsic material is capable of twinning in the course of normal growth, without recourse to causes beyond operator's control.

III.7 Internal lamellar twinning

Under growth conditions more severe than those described in the preceding section, twin lamellae are found, originating away from the edge of the solidification front. One of the findings of the vertical Bridgman growth experiments in CdTe was that the twin spacing distribution did not appear to be random but fluctuated about a value locally determined by thermal conditions. Figures 7.1a and b illustrate the relative uniformity of the twin spacing in two views of the same crystal. The purpose of that run having been to precast a charge for another experiment, it was pulled at $5\mu\text{m}/\text{sec}$ (an order of magnitude faster than would have been the case for a regular run), hence the heavy twinning.

The model proposed here for this type of twinning relies on the assertion that two driving forces present in crystal growth operate sometimes at cross purposes. To illustrate this idea we now refer to Fig. 7.2a where a coherent twin boundary is shown advancing obliquely into the melt. Due to a lower density of dangling bonds, the grain on the right is faced with a higher kinetic undercooling. In order to lower it, the crystal may twin, while at the same time incurring the penalty of a developing high energy grain boundary (Fig. 7.2b). Eventually a near "steady" state is achieved where the undercooling force is small but where the high energy grain is continuing to advance (Fig. 7.2c). These are appropriate conditions under which a new twin plane can stop the high

energy boundary, at the same time leading to another transient in undercooling. Repeating this cycle would lead to an oscillatory effect observable as lamellar twinning.

Stacking considerations require that each of the twin domains bounded on one side by an incoherent planar defect be an integral multiple of three double layers in thickness (as also pointed out by Mendelson 1967). The smallest such domain is depicted in Fig. 7.3a as part of a lamellar configuration. Figures 7.3b and c show an example of this configuration in CdTe under 250X magnification using two types of surface preparation (courtesy of Brian Fabes). Note that in this example the $(1\bar{1}0)$ axis is tilted slightly with respect to the normal to the page resulting in a slightly changed apparent twin dihedral angles. Two possibilities arise (Figs. 7.4a and b) according to which of the two angles contains the local interface normal. The dangling bond diagram (Fig. 6.4) for twinned elemental semiconductors allows both possibilities under the following conditions:

i) - Acute angle (70.5°) toward the melt with interface normal some 60° away from the zone of the twin planes (Fig. 7.4a)

ii) - Obtuse angle (109.5°) toward the melt with interface normal nearly parallel to the zone of the twin planes (Fig. 7.4b)

In both cases an oscillation can only be sustained if the domain with the higher density of dangling bonds is also the one with the incoherent (or high energy) boundary with the

underlying grain.

The fact that in our experiments on CdTe only type (i) was observed may be indicative of the polarity of lattice and of the need to incorporate the results of the next section into the present argument.

III.8 Polar effects

The dangling bond model presented in Section III.5 above was restricted to tetrahedrally coordinated semiconductors. To generalize the model to the binary compounds we will allow opposite type of $\{111\}$ steps ($\{111\}_A = \{111\}, \{1\bar{1}\bar{1}\}, \{\bar{1}\bar{1}\bar{1}\}$, or $\{\bar{1}\bar{1}\bar{1}\}$, and $\{111\}_B = \{\bar{1}\bar{1}\bar{1}\}, \{\bar{1}\bar{1}\bar{1}\}, \{1\bar{1}\bar{1}\}$ or $\{1\bar{1}\bar{1}\}$, where the A surface terminates with atoms of groups II or III and the B surface with atoms of groups VI or V) to carry different effective numbers of dangling bonds. Specifically, we will endow B type steps with $1 + \xi$ dangling bonds while keeping the other contributions unchanged. To parallel the derivation of Section III.5 the calculation will differ only in regions I'', I''', II and II' of figure 5.2 in the following respects.

In region I'' the periodic area A

$$\frac{\bar{A}}{d^2} = n \frac{\sqrt{3}}{2} \left[\frac{1}{\sqrt{3}} (11\bar{1}) + m (00\bar{1}) \right]$$

will contain $2m+n(1+\xi)$ dangling bonds with a density

$$\begin{aligned} \mathcal{N} &= \frac{2}{d^2} \frac{2m+n+\xi n}{(n, n, 2m+n)} = \frac{2}{d^2} \left[\hat{n} \cdot (00\bar{1}) + \frac{\xi}{2} \hat{n} \cdot (110) \right] = \frac{2}{d^2} \hat{n} \cdot \left(\frac{\xi}{2}, \frac{\xi}{2}, \bar{1} \right) \\ &= \frac{2}{d^2} \left[\hat{n} \cdot (00\bar{1}) \left(1 - \frac{\xi}{2}\right) + \frac{\sqrt{3}}{2} \xi \hat{n} \cdot \frac{1}{\sqrt{3}} (1\bar{1}\bar{1}) \right] \end{aligned} \quad (8.1a)$$

Similarly, in region I'''

$$\begin{aligned} \mathcal{N} &= \frac{2}{d^2} \left[\hat{n} \cdot (00\bar{1}) \left(1 - \frac{\xi}{2}\right) + \frac{\sqrt{3}}{2} \xi \hat{n} \cdot \frac{1}{\sqrt{3}} (\bar{1}\bar{1}\bar{1}) \right] \\ &= \frac{2}{d^2} \hat{n} \cdot \left(\frac{\xi}{2}, \frac{\xi}{2}, \bar{1} \right) \end{aligned} \quad (8.1b)$$

In region II of Fig 5.2, Eq. 5.5 will be modified to

$$\mathcal{N} = \frac{m+n(1+\xi)}{\frac{d^2}{2} |(m+n, m+n, m-n)|} = \frac{2}{d^2} \left[\hat{n} \cdot (010) \left(1 - \frac{\xi}{2}\right) + \frac{\sqrt{3}}{2} \xi \hat{n} \cdot \frac{1}{\sqrt{3}} (11\bar{1}) \right] = \frac{2}{d^2} \hat{n} \cdot \left(\frac{\xi}{2}, 1, \frac{\xi}{2} \right) \quad (8.2a)$$

$$= \frac{2}{d^2} \left[\hat{n} \cdot (100) \left(1 - \frac{\epsilon}{2}\right) + \frac{\sqrt{3}}{2} \epsilon \hat{n} \cdot \frac{1}{\sqrt{3}} (11\bar{1}) \right] = \frac{2}{d^2} \hat{n} \cdot \left(1 \frac{\epsilon}{2} \frac{\epsilon}{2}\right) \quad (8.2b)$$

The three dimensional appearance of this modified function may be visualized by imagining the unmodified version and then splitting each of the (001) type lobes into two partially overlapping spheres in such a way so as to increase the density of bonds in the B direction. Instead of six we now have a 12-lobed function. When ϵ is small the effect is that of having each (001) lobe slightly elongated toward the B directions. When ϵ is large (say, of order unity) then the split halves will tend to merge in groups of three around the B directions. This is the situation depicted in Fig. 8.1 where ϵ was chosen to be unity. It is seen that \mathcal{N} is already greater in a B direction than in a (001) direction. In fact it can be shown that that will be the case for any value of ϵ greater than ϵ_0 , where

$$\epsilon_0 = \frac{2}{1+\sqrt{3}} \approx .732 \quad (8.3)$$

So for etching of spheres we expect the ultimate form to be progressively more tetrahedral as ϵ increases. Such shapes, with fast etching B faces have been reported in GaAs (Richards 1960) and in InSb (Gatos and Lavine JPCS 1960). In addition Gatos and Lavine (op. cit.) found other features which lend credence to the present model: i) - the appearance of three faces in the vicinity of the B directions and ii) - the presence of four sets of six converging facets, strongly reminiscent of the six lobes surrounding the A faces in Fig. 8.1. They also report that B faces and (100) faces had about

the same etch rate in their modified CP-4 etchant.

With regard to growth anisotropy, the predictions in the polar case are again different. Growing on a B face should definitely be easier than on an A face. Experimentally this is nearly universally known to be the case (Prof. A. F. Witt, private communication). It should be noted however that some of the early work had reported greater faceting and more difficult nucleation on B faces (e.g. Hulme and Mullin SSE 1962, Steinemann and Zimmerli SSE 1963, Barber and Heasell 1965). One other paper (Seidensticker and Hamilton JPCS 1963) in attempting to reconcile the idea of a B face with a large nucleation barrier with their own experimental findings, arrives at the notion of a "noble" B face which grows fast. Such reports are at variance with the currently accepted view of polarity effects in crystal growth, as well as the model presented above.

A study of stability against twinning in the polar semiconductors along the lines of Fig. 6.7, while currently in progress, has not yet been completed. Nevertheless, qualitative features are already apparent in Fig. 8.1. For sufficiently large ξ , twinning on an A plane will not decrease the kinetic undercooling during B growth, hence it will not happen. On the other hand, A growth can always lead to B twinning regardless of ξ . The experimental evidence for this statement is abundant. Notably, Hulme and Mullin SSE 1962 (who, as mentioned above, felt that faceting on B faces was more pronounced than on the A faces) listed seed

orientations for InSb in order of decreasing suitability for monocrystalline growth. The sequence $[111]$, $[211]$; $[311]$; $[100]$; $[110]$, $[\bar{1}\bar{1}\bar{1}]$ (note their use of the opposite sign convention) they found experimentally is entirely consistent with a decreasing dangling bond density as shown in Fig. 8.1.

Another feature suggested by Fig. 8.1 is the possibility of 90° twins (perpendicular to the growth axis) for B seeded crystals with little or no deviation from the intended alignment. Such an occurrence has been reported in InSb by Witt, Gatos, Lichtensteiger, Lavine and Herman 1975 in the form of rotational (lamellar) bands. With a slight amount of interface curvature, vicinal surfaces corresponding to the "difficult" growth directions could be exposed. Rotational twinning might then interchange the "easy" with the "difficult" directions, the event recurring after the consummation of the undercooling transient.

It should be emphasized that nothing in this model provides a value for ϵ . Ideally, further theoretical work would make it expressible in terms of the ionicity or the charge distribution of the compound. In practice, it may simply be left as a free parameter to be determined experimentally. Furthermore the interpretation of \mathcal{N} as a density of dangling bonds may be called into question when ϵ is different from zero. But, as we have seen in this section, the presence of the extra electrons on B faces does appear to behave as though more bonds were present.

III.9 Clustering model

During the course of the investigation into growth twinning mechanisms, some attention was paid to the possibility of a "twin nucleus" originating in certain types of melt and then arriving at an advancing interface at some mean rate. Such events would be more likely in the more highly associated melts, i.e. those retaining a relatively high fraction of covalent bonding in the form of clusters or random networks.

The stability of small clusters was determined by computing the average number of dangling bonds per atom. The process was simplified by imposing tetrahedral bonding and disregarding polar effects. Table 1 lists this average for clusters of up to 8 atoms. The remarkable finding is that the smallest cluster where this average falls below the threshold value of 2 is the 8-atom cluster of Fig. 9.1. This cluster can be readily seen to be the smallest stable portion of the wurtzite lattice - or, what is the same thing - of a twin plane in the sphalerite lattice.

No. atoms	Distinct topologies	Dangling bonds	Per atom
1	1	4	4
2	1	6	3
3	1	8	~2.67
4	2	10	2.5
5	3	10	2.4
6	1	12	2
	3	14	~2.33
7	1	14	2
	6	16	~2.29
8	==> 1	==> 14	==> 1.75
	4	16	2
	7	18	2.25

Consideration of Fig. 9.2 will evidence the fact that the most energetically favored position of an 8 atom cluster on an undercooled {111} surface is such that a twin plane will be initiated obliquely. There is some bond angle distortion and anomalous 3 atom coordination at the junction but that will occur regardless of the twin mechanism. Depending on which of the two types of oblique twins (Fig. 9.3) the cluster initiates, the result may be a single lamella or a more complicated structure such as given in Fig. 7.3.

Potential consequences of a clustering mechanism can be seen from the following argument.

The total number N_8 of 8 atom clusters is obtained from a time and space integral of the appropriate nucleation rate

$$N_8 = \iint dt dV \frac{\partial^2 N_8}{\partial t \partial V}$$

If we assume that the clustering effectively takes place only in the undercooled region of the melt, of thickness

$$f = \frac{\Delta T_y}{G}$$

the integral becomes

$$N_g = \int \frac{dz dA}{R(z)} \frac{\partial^2 N_g}{\partial t \partial V} \approx \int V \overline{\frac{\partial^2 N_g}{\partial t \partial V}} \left[\frac{1}{V} \int \frac{dV}{R(z)} \right]$$

The result can be estimated by assuming a nearly constant growth rate so that

$$(\bar{R})^{-1} \approx (\overline{R^{-1}}) \approx R^{-1}$$

and

$$N_g = \frac{V \Delta T_u}{G R} \frac{\partial^2 N_g}{\partial t \partial V}$$

For single crystal growth we require that this quantity be less than 1, i.e.

$$GR > V \Delta T_u \frac{\partial^2 N_g}{\partial t \partial V} \quad (9.1)$$

This requirement on G and R is plotted in Fig. 9.4 together with the constitutional supercooling criterion to yield a region where single crystal growth is allowed. The existence of a minimal thermal gradient below which sustained monocrystalline growth is not possible is a novel feature, not previously disclosed by other theories.

Other limitations in (G,R) space may also exist, related to such factors as thermal stresses in the growing solid and thermal stability of the confining walls.

Experimental evidence for this type of twinning mechanism is limited. Iseler 1980 has reported the existence of a minimal G for monocrystalline InP grown by LEC. He also noted that the value of G_{\min} is increased by the addition of various dopants, which can readily be understood in terms of the clustering model.

Searching for materials where this mechanism may be applicable is simplified by tabulating the volume change on melting. A small value of $\Delta V/V_s$ implies a small change in

the average coordination number, i.e. retention to a greater degree of covalent bonding. As can be seen from Table 9.2 (processed from data in Glazov et al. RJPC 1969) CdTe differs sharply from the other semiconductors listed. Not only is the change on melting smaller in magnitude but it also has the opposite sign. Of the other materials, the one with the next smallest change on melting (Ge) is still better than an order of magnitude higher than that of CdTe.

TABLE III.9.2

Material	$\frac{\Delta V}{V_s} \%$
Si	-9.1
Ge	-4.5
AlSb	-11.4
GaSb	-8.7
InSb	-11.1
GaAs	-9.6
InAs	-6.6
CdTe	+0.35

A more precise definition of the state of the melt is the average coordination number n . In Appendix A3 a polynomial relationship is developed between the filling factor ff and n .

Given the experimentally determined interparticle separation

b_{melt} and melt density, the filling factor ff_{melt} can be expressed as

$$ff_{melt} = \frac{\pi}{3} \frac{N_A \rho_m b_m^3}{M} \quad (9.2)$$

Then the value of n may be read off the graph in Fig. 9.5.

For example, in the case of InSb, Glazov and collaborators have

reported $\rho_{melt} = 6.48 \text{ g/cc}$ (Glazov et al. RJPC 1969) and $b_{melt} = 3.15 \text{ \AA}$ (Glazov et al. book 1969). The molar mass M was given by Sirota 1968 as 236.57 g/mole. Using Eq. 9.2 we

find $ff_{\text{melt}} = .540$ and from Fig. 9.5 we read $n \approx 6.2$. This is consistent with the rocksalt coordination of 6 listed by Glazov (Glazov et al. book 1969).

This approach can thus be used to deduce the average coordination number in the melt, and should be useful in an assessment of the validity of the clustering model of growth twinning.

III.10 Conclusions

The dangling bond model has led to the unified explanation of a variety of phenomena. It therefore appears that in most cases twinning occurs deterministically as a result of the interplay between the applied thermal field and the anisotropy of the growth interface. The degree of uncertainty associated with the spatial and temporal position of new twinning events should be no greater than the uncertainty (i.e. fluctuations) in the configuration of the thermal field itself.

Considering the motive force behind this thesis (see Section 1) the most important feature of the dangling bond model is its ability to explain much of the phenomenology of growth twinning. A diagram of stability against growth twinning is explicitly given for elemental semiconductors (Fig. 6.7). The polar case is equally promising but more qualitatively treated in Section 8. The lamellar model of Section 7 gives hope to the goal of the eventual achievement of regular rotational twinning. Thus we can indeed look forward to the use of the nonlinear optics concepts presented in Chapter II in building efficient and inexpensive frequency doubling and mixing devices.

Other successes of the dangling bond model include the qualitative explanation of faceting and preferential etching of the tetrahedrally coordinated semiconductors. Although not discussed above, a preliminary study showed that the

morphology of dendrites, ribbons, webs, whiskers, needles and plates also lend themselves to an understanding in the same terms.

While constrained twinning has been shown to be the prevalent type, accidental twinning remains a possibility. In semiconductors with highly associated melts such as CdTe, the clustering model of Section 9 may provide an alternate explanation. In addition to the preferred occurrence of oblique twins, the model predicts the existence of a region in G-R space outside of which monocrystalline growth cannot take place. In particular, there exists a minimal thermal gradient below which no single crystals will result, regardless of the pull rate.

III.11 Future research

To further check the above models a number of experiments suggest themselves. In most of these, use of the interface demarcation technique developed at M.I.T by Professors Witt and Gatos and collaborators (Witt and Gatos JES 1967 and 1968, Singh, Witt and Gatos 1968, Lichtensteiger, Witt and Gatos 1971) will be indispensable. For example, a study of threshold effects in oblique twinning for a given orientation should yield results from which the corresponding threshold for another orientation could be calculated.

Bridgman experiments with twinned seeds should provide verification for the lamellar model of Section 7. In fact, an even simpler experiment would be an unseeded Bridgman run using a tilted ordinary quartz ampoule to create thermal asymmetry. The expectation is that a result similar to that of Fig. 3.4 would be obtained.

A different series of experiments should be done in a Czochralski system to measure the systematics of interface demarcation line angles with the growth axis in the vicinity of central facets and near the external surface. It is believed that such measurements could be used for a determination of the polarity parameter in the compound semiconductors. The same purpose would be served by etching monocrystalline spheres of various II-VI and III-V materials where this has not yet been done.

Much theoretical work remains to be done too. A high

priority should be given to developing the polar results to the extent achieved in Sections 5 - 7. Also of great interest would be the development of a microscopic growth rate theory incorporating the results of this chapter. A preliminary look in that direction has already indicated a possibility of interface instability and breakdown lying completely outside present morphological instability theories. Such instabilities could occur in arbitrarily pure materials of certain orientations under the influence of transient interface perturbations. For other orientations these perturbations could lead to the propagation of dispersionless growth waves (solitons) across the interface.

Finally, the influence of melt association on growth should be investigated. It is expected that significant clustering would influence not just the clustering model of Section 9 but also the dangling bond model of the growth interface.

A1 Estimate of sticking probability during growth from the melt

We compare the layer deposition rate $1/\tau_{\text{dep}}$ in normal growth to the collision rate $1/\tau_{\text{coll}}$ in the melt:

$$P = \frac{\tau_{\text{coll}}}{\tau_{\text{dep}}} \quad (1)$$

In the (111) direction the layer thickness is $4b/3$ so that

$$\tau_{\text{dep}} = 4b/3R \quad (2)$$

The collision time is

$$\tau_{\text{coll}} = \lambda/v_T \quad (3)$$

where λ is the mean-free-path and v_T is the thermal velocity.

We estimate these as follows:

$$\lambda = v_{\text{molec}} / \sigma \quad (4)$$

where

$v_{\text{molec}} = M/(N_A \rho_1)$ = molecular volume
and

$$\sigma = 4\pi b^2 = \text{collision cross section} \quad (5)$$

Also

$$v_T = \sqrt{(3RT/M)} \quad (6)$$

Combining Eqs. 1-6 and evaluating for CdTe

$$P \sim 2.5 \times 10^{(-10)} \quad (7)$$

The values used were

$M=240$ g/mol

$\rho_1=5.67$ g/cc

$b=2.81$ Å

T=1365 °K

III.A2 Twinning operations and low index directions

A general 3 X 3 rotation matrix $R(\hat{u}, \varphi)$ can be written

$$[R(\hat{u}, \varphi)]_{ij} = \delta_{ij} \cos \varphi + u_i u_j (1 - \cos \varphi) - \epsilon_{ijk} u_k \sin \varphi$$

(Professor R. Balluffi 3.33 course notes, Spring 1980, M.I.T.)

For twinning $\varphi = 180^\circ$ and

$$R(\hat{u}) = 2\hat{u}\hat{u}^t - \mathbf{1}$$

The matrices

$$R(\hat{u}_2, \hat{u}_1) \equiv R(\hat{u}_2') R(\hat{u}_1)$$

in Table 1 below express the coordinate transformation of a vector imbedded into the lattice after the latter has undergone two successive twinning operations. Note that

$$\hat{u}_2' = R(\hat{u}_1)\hat{u}_2 \Rightarrow R(\hat{u}_2') = R(\hat{u}_1)R(\hat{u}_2)R(\hat{u}_1)^t$$

i.e.

$$R(\hat{u}_2, \hat{u}_1) = R(\hat{u}_1)R(\hat{u}_2)$$

Also note that $R(\hat{u}) = R(-\hat{u})$.

The results for first and second order twinning operations onto the tetrahedral (previously published by Slawson 1950) and cubic directions are listed in Table 2.

III.A3 Filling factor versus coordination number

In a hard sphere approximation the filling factor ff (or packing fraction) is given by $ff = V_{at} / V$ where V_{at} is the spherical volume. For a binary compound of fairly closely matched components (i.e. where we can ignore differences of atomic radii) with mean nearest distance b , density ρ and molar mass M , its value may be obtained from

$$ff = \frac{\frac{4\pi}{3} (b/2)^3}{M / (2N_A \rho)} = \frac{\pi}{3} \frac{N_A \rho b^3}{M} \quad (1)$$

To obtain a relationship between ff and the coordination number n , we considered the exactly known data points of Table 1. The following cubic was found to be the lowest order polynomial fitting the data

$$ff = 0.0646 + 0.0321n + 0.0128n^2 - 0.000897n^3 \quad (2)$$

This function is displayed in Fig. 9.5.

In addition to the InSb example discussed in Section 9, we have found the following check of Eq. (2). The coordination number for an "ideal" RCP (random-close-packed structure) was independently calculated to be 13.397. Since the value was subsequently found in the literature (Nelson preprint), the derivation will not be presented here. Upon substitution in Eq. (2) we find the following filling factor for the RCP

$$ff \approx 0.632 \quad (3)$$

This is within 1% of the experimentally determined value of .63(7) (Scott 1960). Equation (2) makes also the as yet unverified prediction that there is a range of coordination

numbers $9 \leq n < 12$ of density higher than that of the FCC structure. The maximum packing density would be .773 at $n \approx 10.6$.

References

- Aminoff, J. and Broome, B.
Strukturtheoretische Studien über Zwillinge. I
Z. Krist. 80, 355 (1931)
- Barber, H.D. and Heasell, E.L.
Polarity effects in III-V semiconducting compounds
J. Phys. Chem. Solids 26, 1561 (1965)
- Billig, E.
Growth twins in crystals of low coordination number
J. Inst. Metals 83, 53 (1954)
- Billig, E.
Growth of mono-crystals of germanium from an undercooled melt
Proc. Roy. Soc. A229, 346 (1955)
- Billig, E. and Holmes, P.J.
Some speculations on the growth mechanism of dendrites
Acta Met. 5, 54 (1957)
- Bolling, G.F., Tiller, W.A. and Rutter, J.W.
Growth twins in germanium
Can. J. Phys. 34, 234 (1956)
- Buerger, M.J.
The genesis of twin crystals
Amer. Mineralogist 30, 469 (1945)
- Cahn, R.W.
Twinned crystals
Adv. in Physics 3, 363 (1954)
- Däweritz, L.
Warscheinlichkeit der Zwillingsbildung in dünnen Schichten von Halbleitersubstanzen mit Diamant und Zinkblendestruktur
Kristall und Technik 7, 167 (1972)
- De Nobel, D.
Phase equilibria and semiconducting properties of cadmium telluride
Philips Res. Repts. 14, 361 & 430 (1959)
- Dermatis, S.N., Faust, Jr., J.W. and John, H.F.
Growth and morphology of silicon ribbons
J. Electrochem. Soc. 112, 792 (1965)
- Donnelly, T.W.
Kinetic considerations in the genesis of growth twinning
Amer. Mineralogist 52, 1 (1967)

- Ellis, Jr., R.C.
Etching of single crystal germanium spheres
J. Appl. Phys. 25, 1497 (1954)
- Ellis, W.C.
Twin relationships in ingots of germanium
Trans. AIME 188, 886 (1950)
- Ellis, W.C. and Fageant, J.
Orientation relationships in cast germanium
Trans. AIME 200, 291 (1954)
- Ellis, W.C. and Treuting, R.G.
Atomic relationships in the cubic twinned state
Trans. AIME 191, 53 (1951)
- Faust, Jr., J.W.
Crystal growth utilizing the twin plane re-entrant edge mechanism
in Proc. Int. Conf. on Cryst. Growth, Boston 1966, H.S. Peiser, ed., Pergamon, 1967
- Faust, Jr., J.W. and John, H.F.
Growth facets on III-V intermetallic compounds
J. Phys. Chem. Solids 23, 1119 (1962)
- Gatos, H.C. and Lavine, M.C.
Chemical behavior of semiconductors: Etching characteristics
in Prog. in Semicond., Vol. 9, A.F. Gibson and R.E. Burgess, eds., CRC, Cleveland 1965
- Gatos, H.C. and Lavine, M.C.
Etching and inhibition of {111} surfaces of the III-V intermetallic compounds: InSb
J. Phys. Chem. Solids 14, 169 (1960)
- Glazov, V.M., Chizhevskaya, S.M. and Glagoleva, N.N.
Liquid semiconductors
Plenum, New York 1969
- Glazov, V.M., Chizhevskaya, S.N., Evgen'ev, S.B.
Thermal expansion of substances having a diamondlike structure and the volume changes accompanying their melting
Russian J. Phys. Chem. 43, 201 (1969)
- Gottschalk, H., Patzer, G. and Alexander, H.
Stacking fault energy and ionicity of III-V semiconducting compounds
Phys. Stat. Solidi A45, 207 (1978)
- Grabmeier, B.C. and Grabmeier, J.G.
Dislocation free GaAs by the liquid encapsulation technique
J. Cryst. Growth 13/14, 635 (1972)

- Haasen, P.
Twinning in indium antimonide
Trans. AIME 209, 30 (1957)
- Hall, E.L. and VanderSande, J.B.
On the nature of extended dislocations in deformed cadmium telluride
Phil. Mag. A37, 137 (1978)
- Hartman, P.
On the morphology of growth twins
Z. Krist. 107, 225 (1956)
- Herring, C.
Some theorems on the free energies of crystal surfaces
Phys. Rev. 82, 87 (1951)
- Holt, D.B.
Grain boundaries in the sphalerite structure
J. Phys. Chem. Solids 25, 1385 (1964)
- Hulme, K.F. and Mullin, J.B.
Indium antimonide - A review of its preparation, properties and device applications
Sol.-State Electr. 5, 221 (1962)
- Iseler, G.W.
Crystal growth of InP by the LEC technique
Sol. State Res. Repts., Lincoln Labs, MIT 3, 21 (1980)
- Jackson, K.A.
Current concepts in crystal growth from the melt
Prog. in Sol. State Chem. 4, 53 (1967)
- Lee, D.B.
Anisotropic etching of silicon
J. Appl. Phys. 40, 4569 (1969)
- Lewis, B.
Nucleation and growth theory
in Crystal Growth, B.R. Pamplin, ed., Pergamon, Oxford 1975
- Lichtensteiger, M., Witt, A.F. and Gatos, H.C.
Modulation of dopant segregation by electric currents in Czochralski-type crystal growth
J. Electrochem. Soc. 118, 1013 (1971)
- Mackenzie, J.K., and Nicholas, J.F.
Bonds broken at atomically flat surfaces
J. Phys. Chem. Solids 23, 195 (1962)

- Mendelson, S.
Microtwin and tri-pyramid formation in epitaxial silicon films
J. Appl. Phys. 38, 1573 (1967)
- Miller, D.C. and Witt, A.F.
Analysis of growth related strain in Czochralski grown indium antimonide using X-ray anomalous transmission topography
J. Cryst. Growth 29, 19 (1975)
- Mueller, R.K. and Jacobson, R.L.
Growth twins in indium antimonide
J. Appl. Phys. 32, 550 (1961)
- Mullin, J.B.
Segregation in indium antimonide
in Compound Semiconductors, Vol.1, R.K. Willardson and H.L. Goering, eds., Reinhold, New York 1962
- Mullin, J.B. and Straughan, B.W.
The melt-growth and characterization of cadmium telluride
Rev. Phys. Appl. 12, 105 (1977)
- Nelson, D.R.
Order, frustration, and defects in liquids and glasses
Preprint, 1983
- Nygren, S.F.
Liquid encapsulated Czochralski growth of 35 mm diameter single crystals of GaP
J. Cryst. Growth 19, 21 (1973)
- Richards, J.L.
Growth of gallium arsenide by horizontal zone melting
J. Appl. Phys. 31, 600 (1960)
- Sangster, R.C.
Model studies of crystal growth phenomena in the III-V semiconducting compounds
in Compound Semiconductors, Vol.1, R.K. Willardson and H.L. Goering, eds., Reinhold, New York 1962
- Seidensticker, R.G.
Dendritic web silicon for solar cell application
J. Cryst. Growth 39, 17 (1977)
- Seidensticker, R.G. and Hamilton, D.R.
The dendritic growth of InSb
J. Phys. Chem. Solids 24, 1585 (1963)
- Singh, R., Witt, A.F. and Gatos, H.C.
Application of Peltier effect for the determination of crystal growth rates
J. Electrochem. Soc. 115, 112 (1968)

- Sirota, N.N.
Heats of formation and temperatures and heats of fusion of
compounds AIII-BV
in Semiconductors and Semimetals, Vol.4, R.K. Willardson and
A.C. Beer, eds., Acad. Press, New York 1968
- Slawson, C.B.
Twinning in the diamond
Amer. Mineralogist 35, 193 (1950)
- Steinemann, A. and Zimmerli, U.
Growth peculiarities of gallium arsenide single crystals
Sol.-State Electr. 6, 597 (1963)
- Strauss, A.J.
The physical properties of cadmium telluride
Rev. Phys. Appl. 12, 167 (1977)
- Vere, A.W., Cole, S., and Williams, D.J.
The origin of twinning in CdTe
J. Electr. Mat. 12, 551 (1983)
- Wilkes, J.G.
The growth of 5kg single crystals of germanium
Proc. Inst. Elec. Engrs. B106, 866 (1959)
- Witt, A.F. and Gatos, H.C.
Determination of microscopic rates of growth in single
crystals
J. Electrochem. Soc. 114, 413 (1967)
- Witt, A.F. and Gatos, H.C.
Microscopic rates of growth in single crystals pulled from the
melt: indium antimonide
J. Electrochem. Soc. 115, 70 (1968)
- Witt, A.F. and Gatos, H.C.
Determination of microscopic rates of growth in single
crystals
J. Electrochem. Soc. 114, 413 (1967)
- Witt, A.F., Gatos, H.C., Lichtensteiger, M., Lavine, M.C. and
Herman, C.J.
Crystal growth and steady state segregation under zero
gravity: InSb
J. Electrochem. Soc. 122, 276 (1975)
- Zanio, K.
Cadmium telluride
in Semiconductors and Semimetals, Vol.13, R.K. Willardson and
A.C. Beer, eds.,
Acad. Press, New York 1978

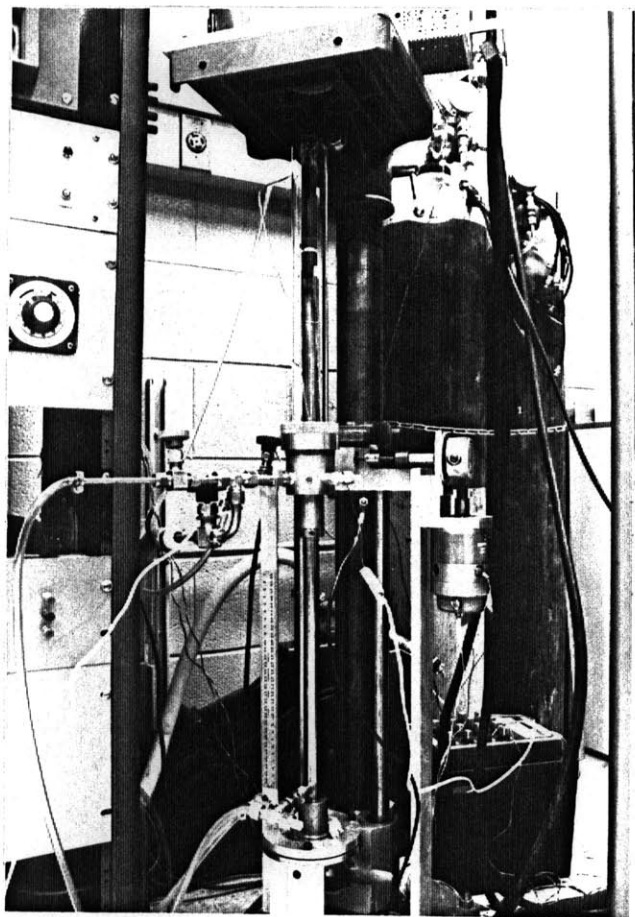


Fig. III.3.2 Growth assembly

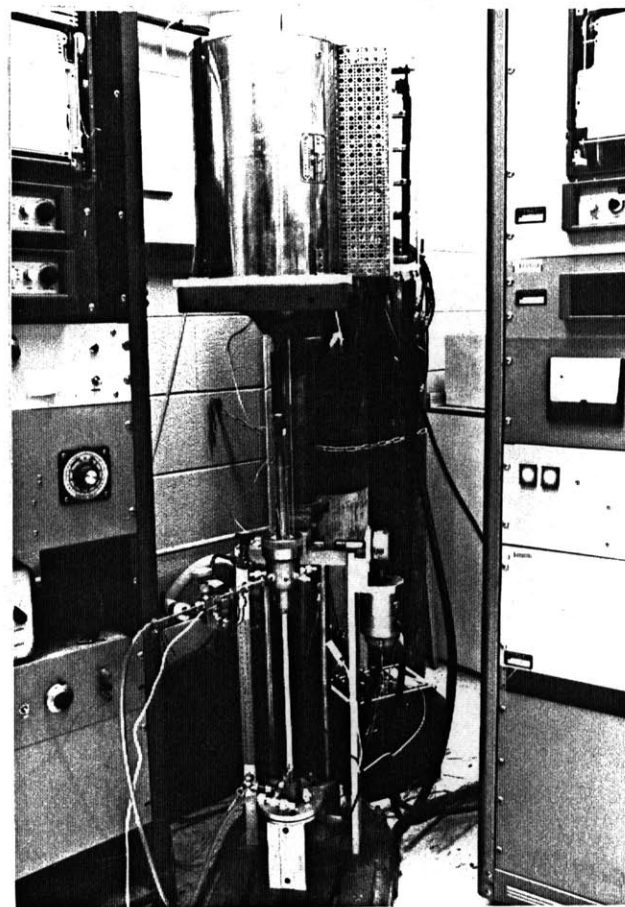
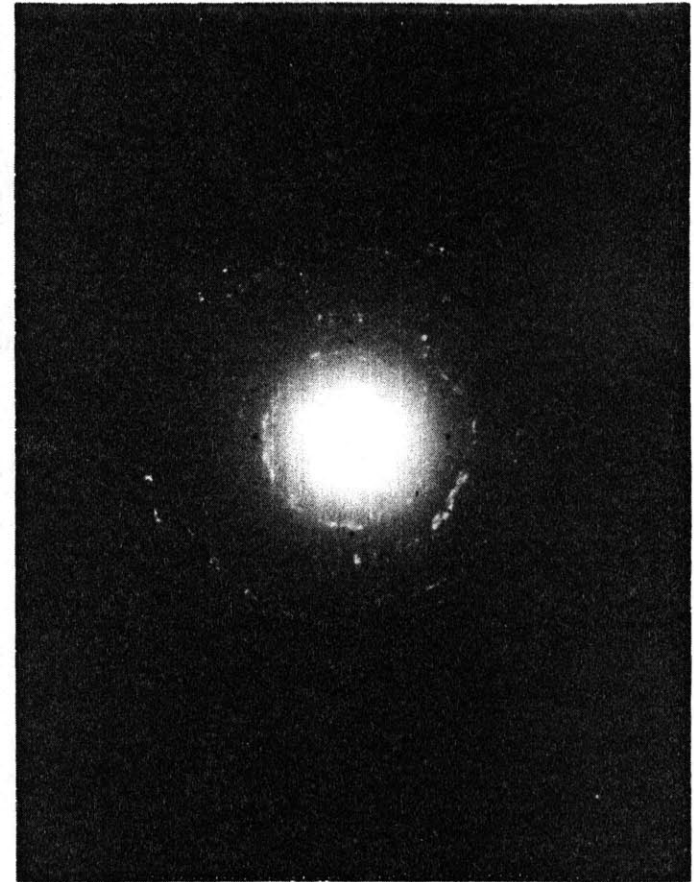


Fig. III.3.1 Vertical Bridgman crystal growth set-up

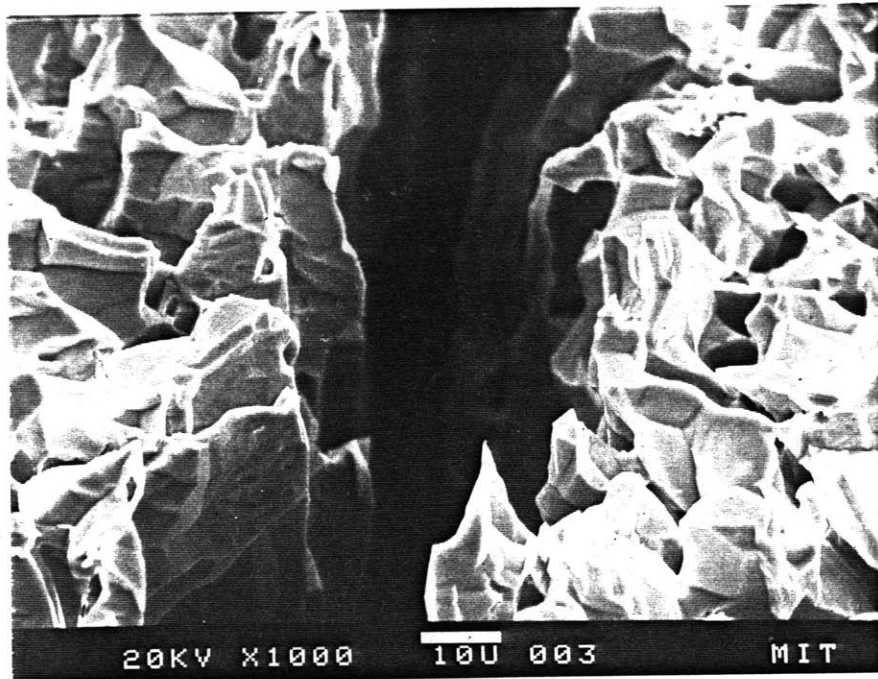


(a) Last-to-freeze region ("meniscus")



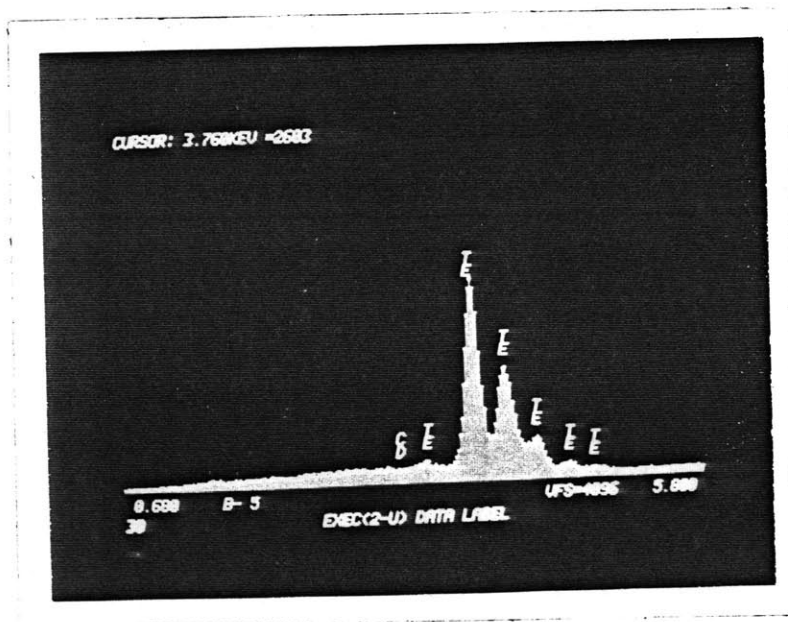
(b) Laue back-reflection from "meniscus"

Fig. III.3.3 CdTe crystal grown by the Liquid Encapsulated Bridgman method



(c)

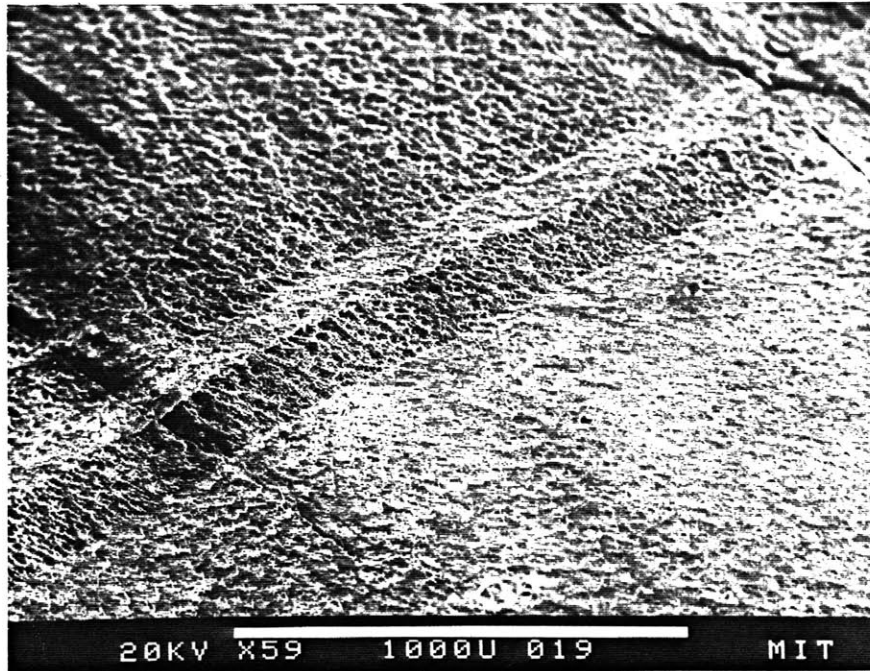
1000X SEM of etched "meniscus" showing crack



(d)

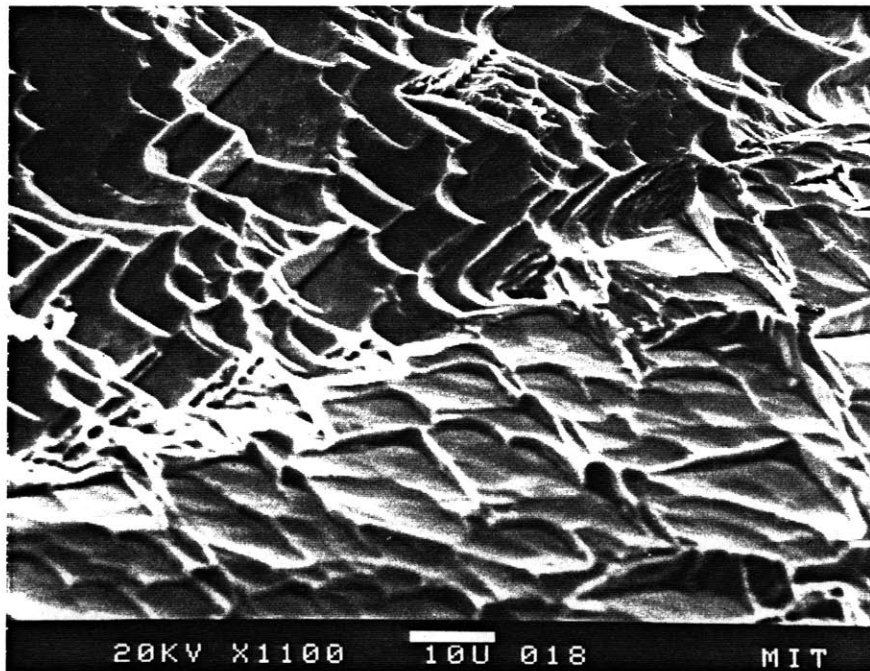
X-ray energy dispersive analysis of "meniscus" showing segregated tellurium

Fig. III.3.3(cont.)



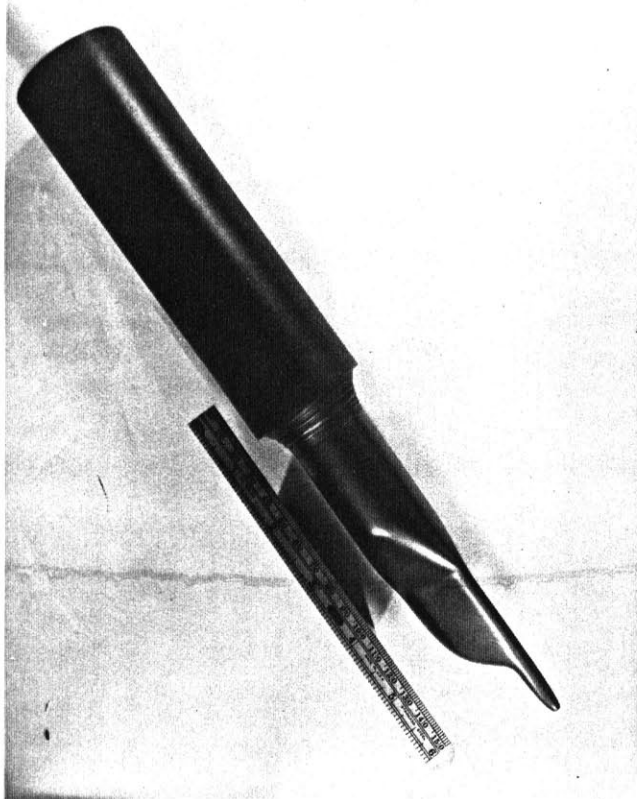
(e)

59X SEM of etched twinned CdTe boule 2mm below "meniscus"



(f)

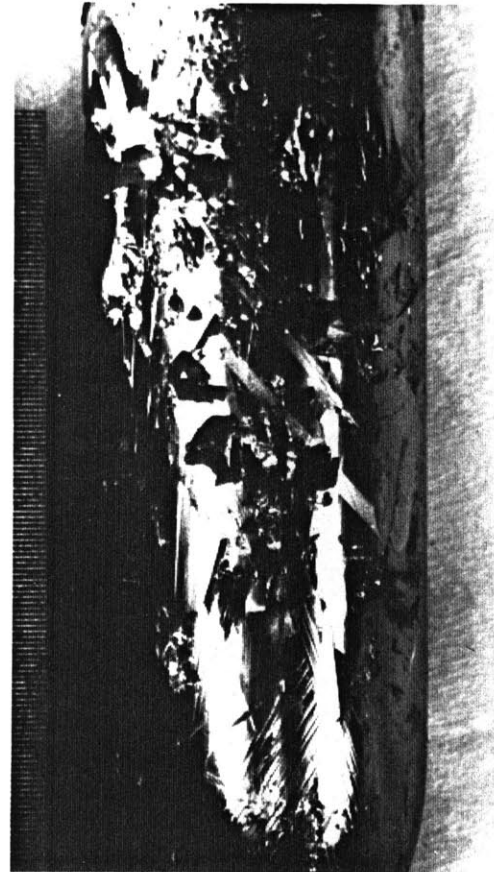
1100X SEM of etched twin boundary showing origin of visible grain contrast



(a)

Graphite mandrel

Fig. III.3.4



(g)

External grooving (scale divisions .01 in. apart)

Fig. III.3.3(concluded)

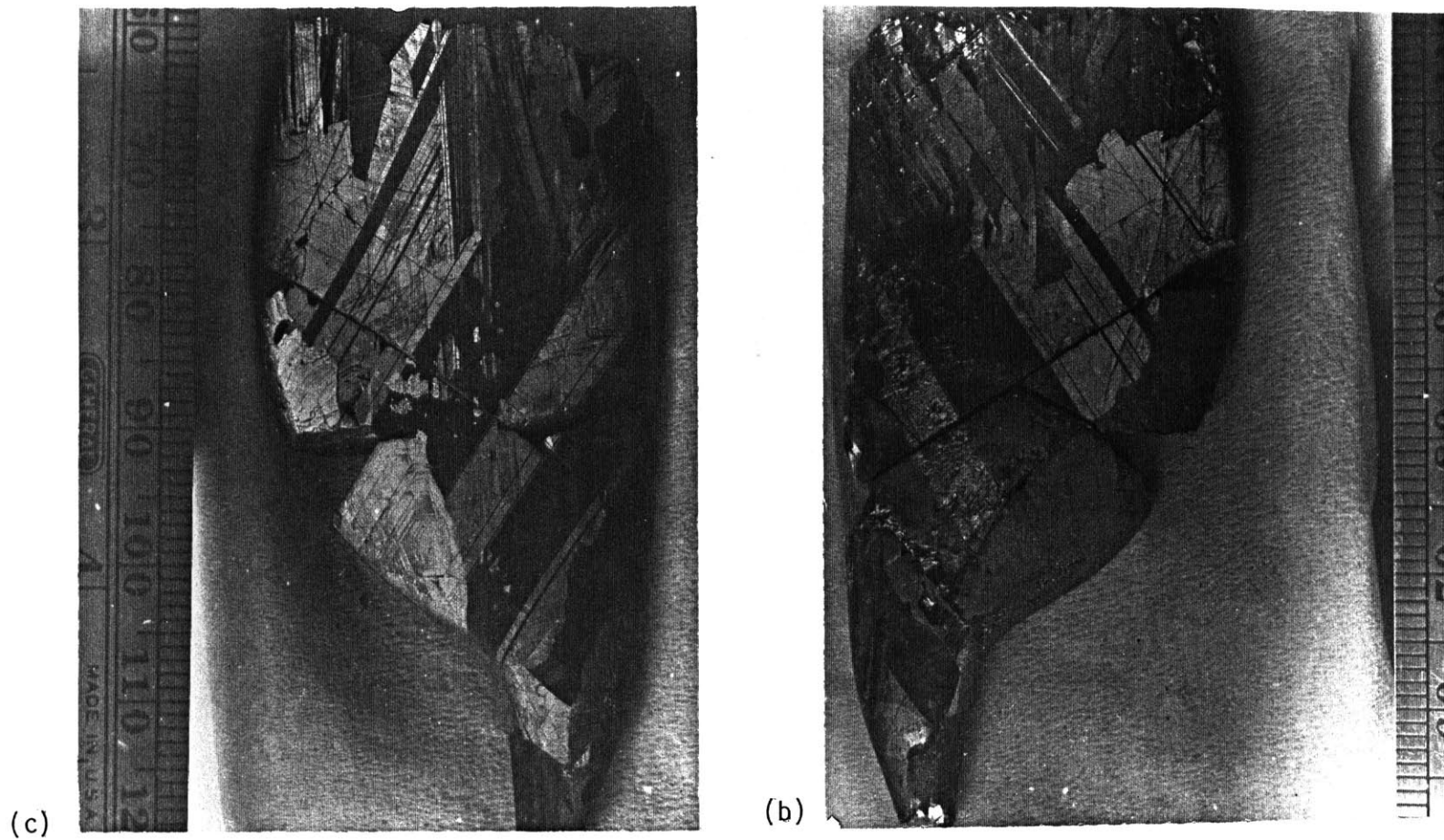


Fig. III.3.4 Etched CdTe boule viewed from opposite directions, showing preferential alignment of lamellar twins

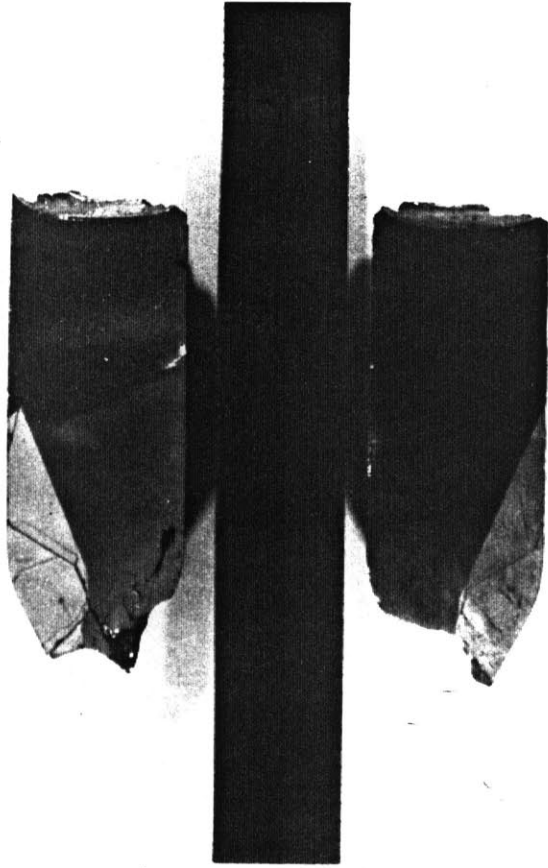


Fig. III.3.6a Etched axial cut through nearly single CdTe boule

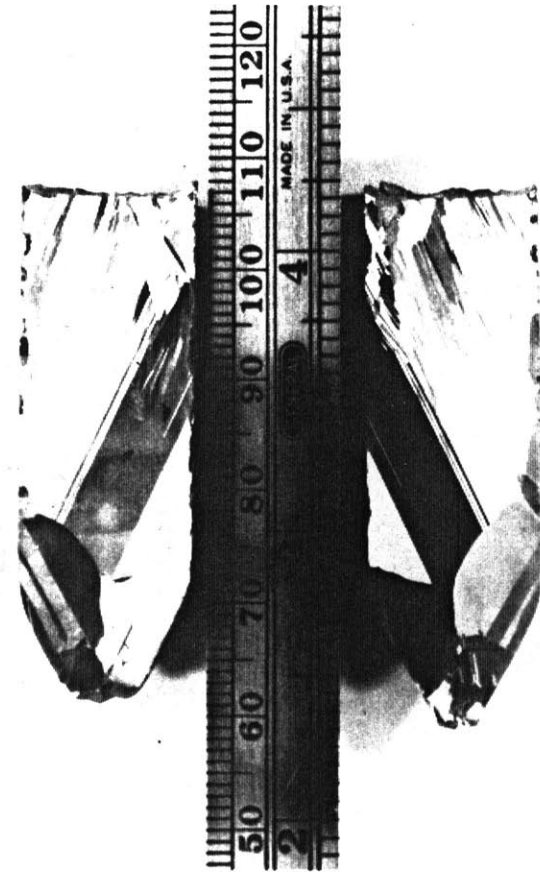


Fig. III.3.5 Etched axial cut through CdTe crystal. This boule did not wet the quartz ampoule

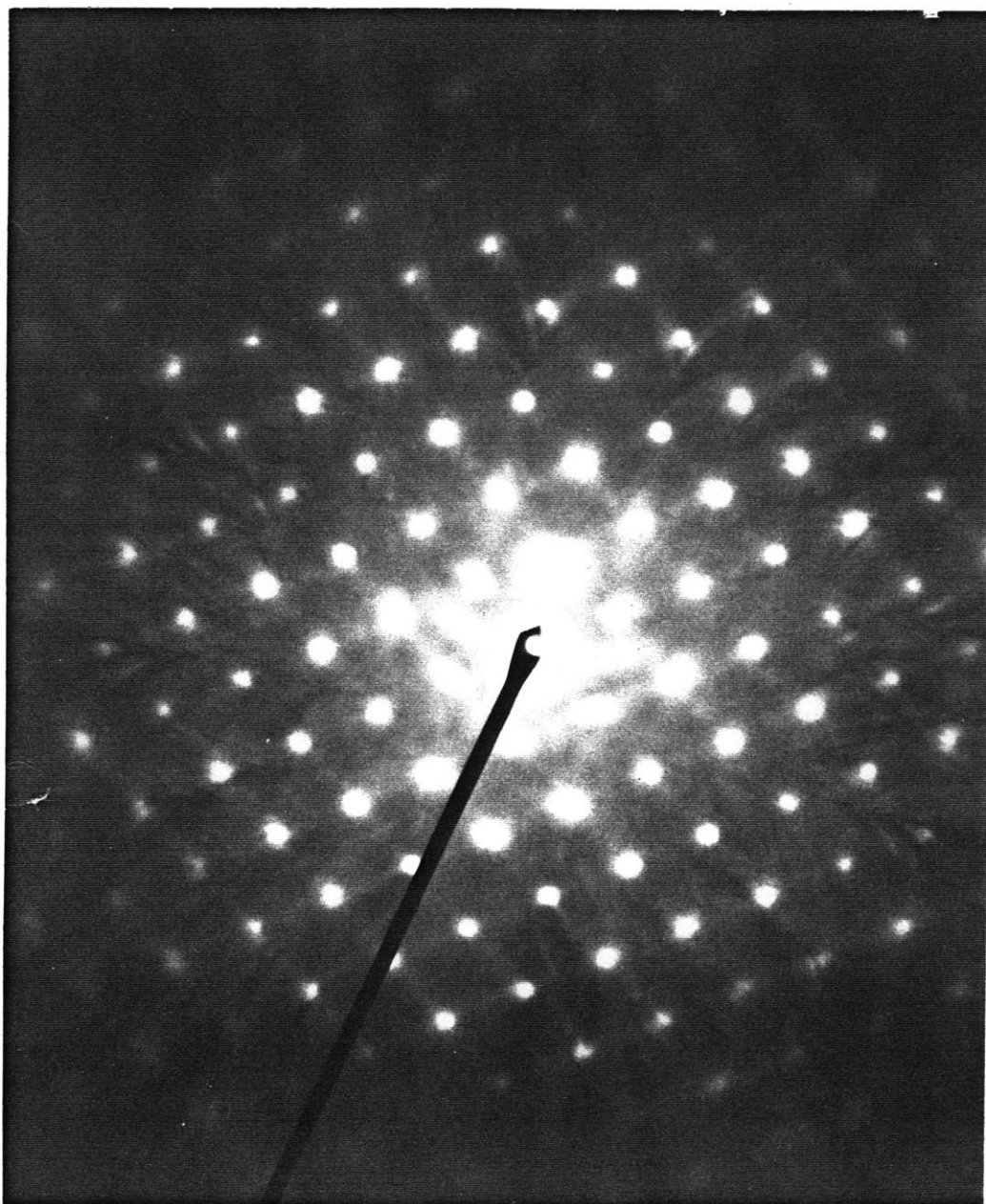


Fig. III.3.6b (110) pole TEM electron diffraction (courtesy J. Nakos)

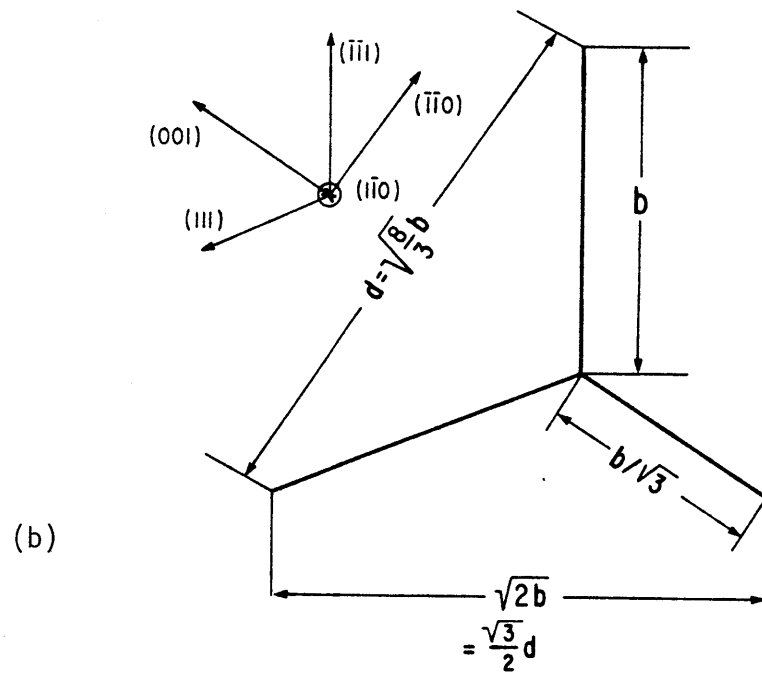
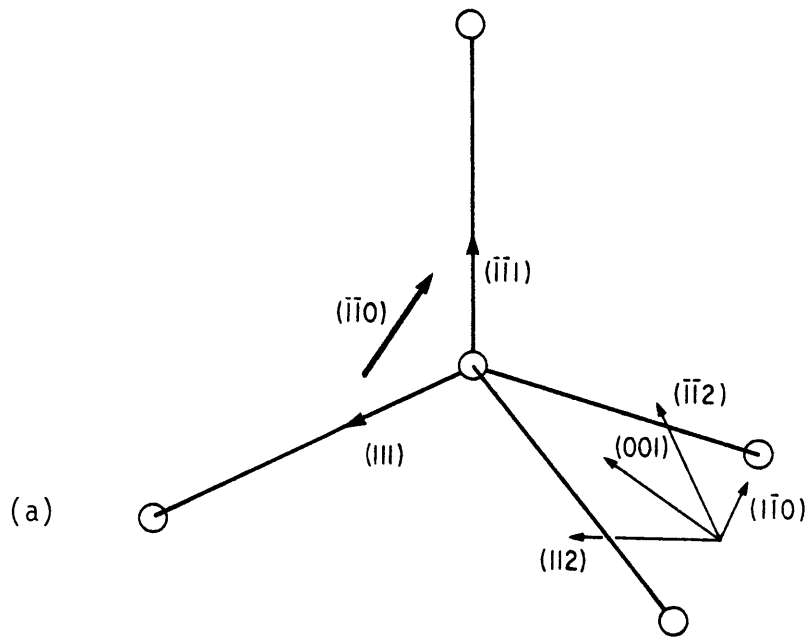


Fig. III.5.1a Nearest neighbor tetrahedral coordination showing important crystallographic directions

Fig. III.5.1b Projection of nearest neighbor tetrahedron onto the $(1\bar{1}0)$ plane

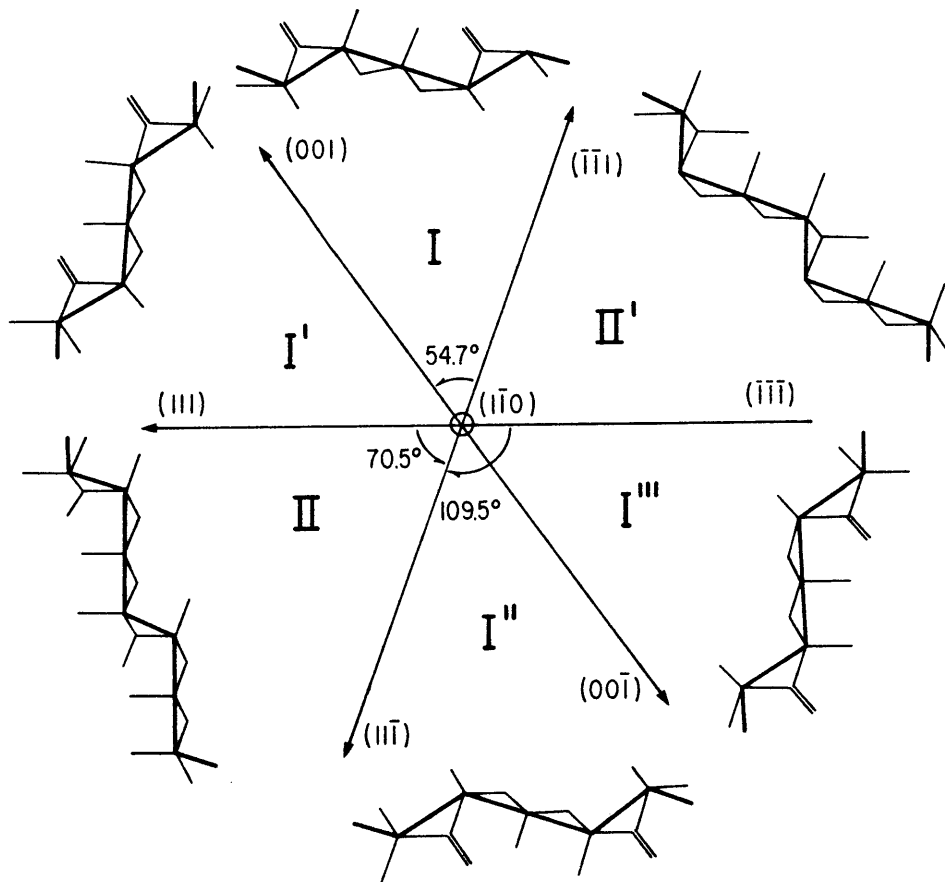
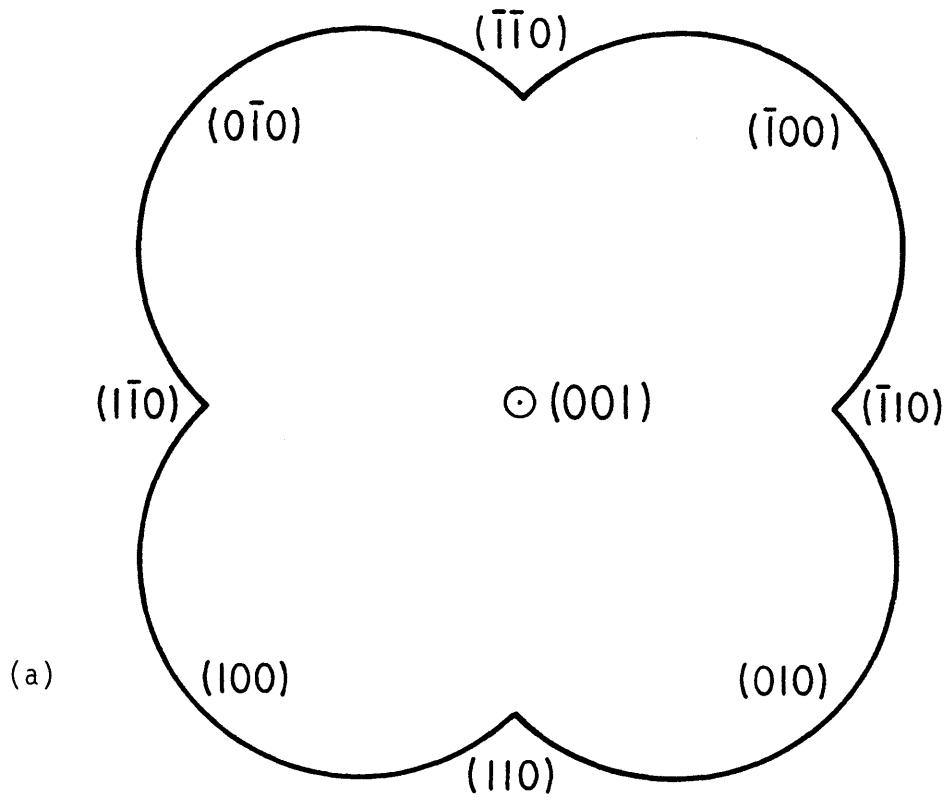


Fig. III.5.2 Typical dangling bond configurations of interfaces with normals in the $(1\bar{1}0)$ zone



Normals in the (001) zone

Fig. III.5.3 Density of dangling bonds vs. interface orientation (polar plots)

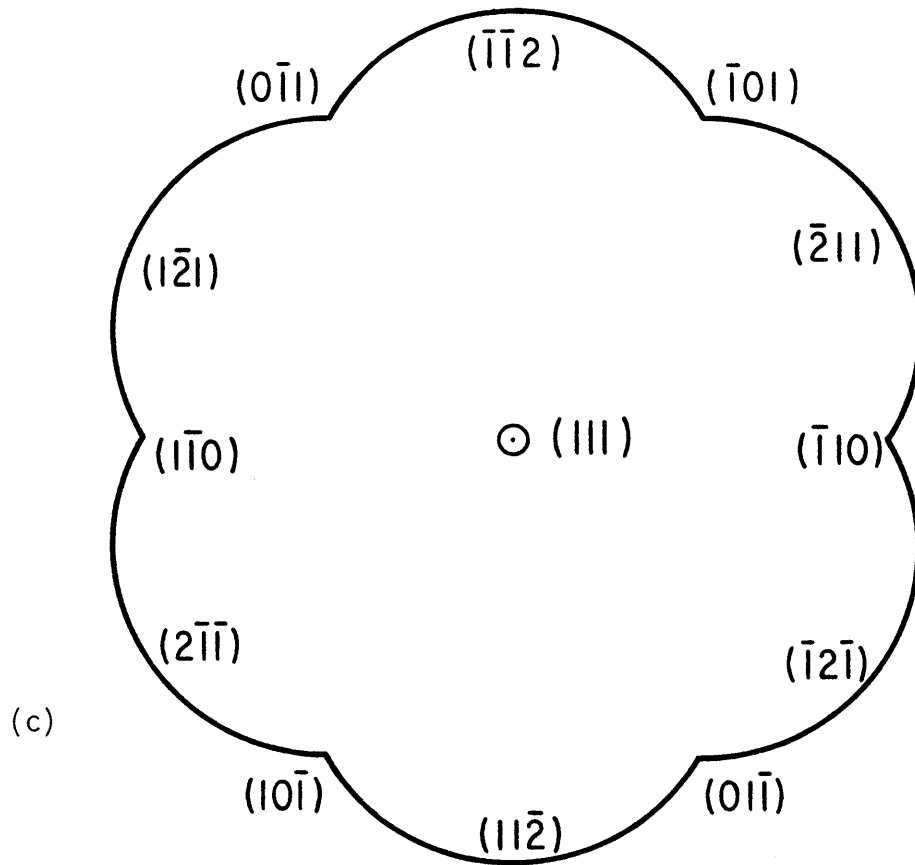


Fig. III.5.3 (concluded)

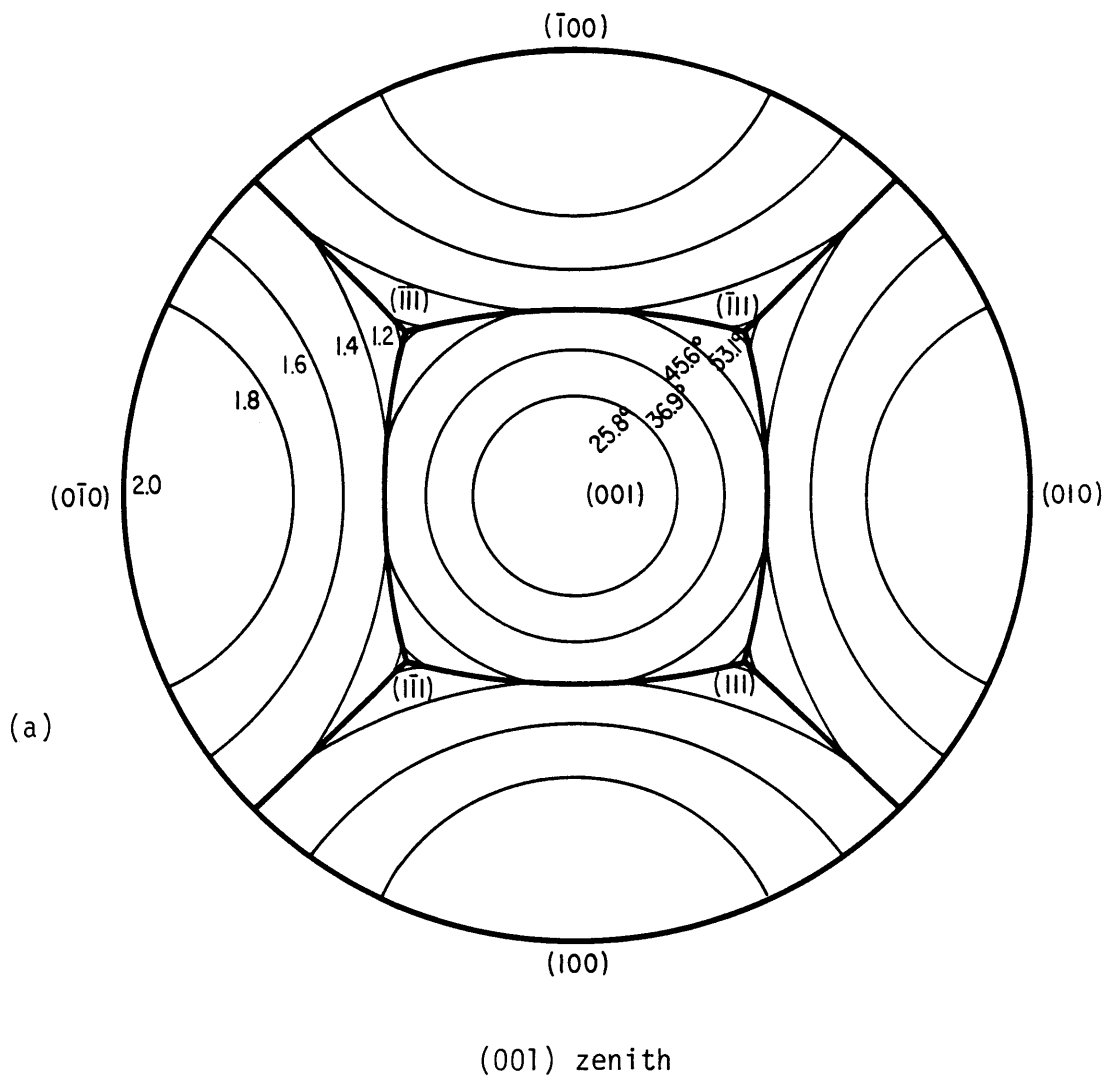


Fig. III.5.4 Constant density of dangling bonds contours in stereographic projection

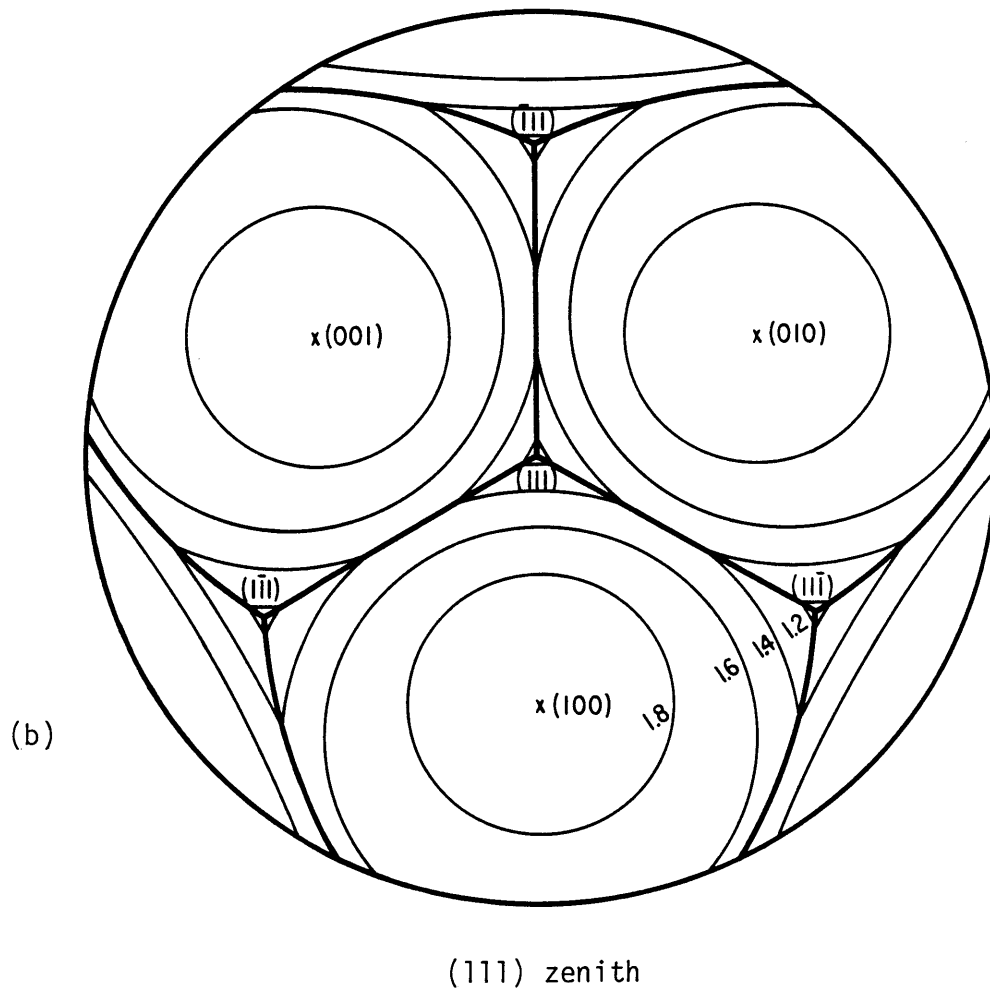


Fig. III.5.4 (concluded)

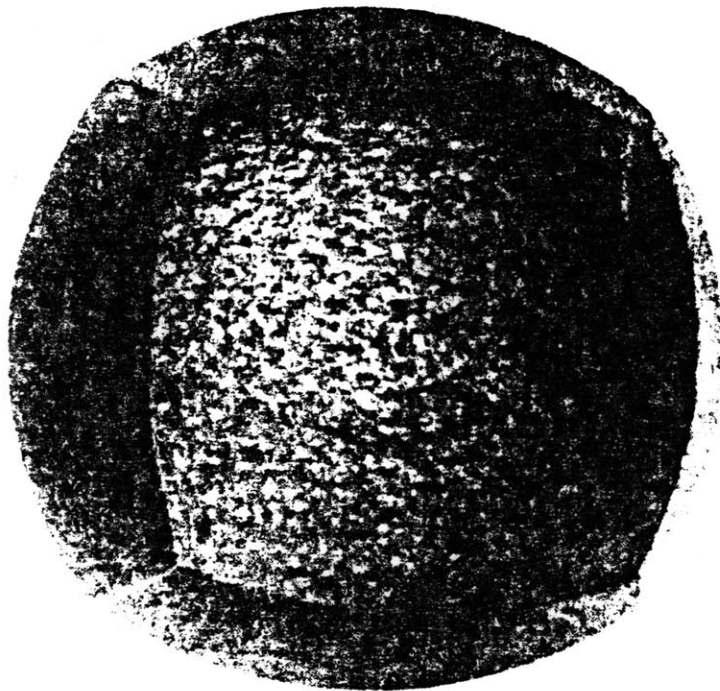


Fig. III.6.1 Etched Si single crystal (from Lee 1969)

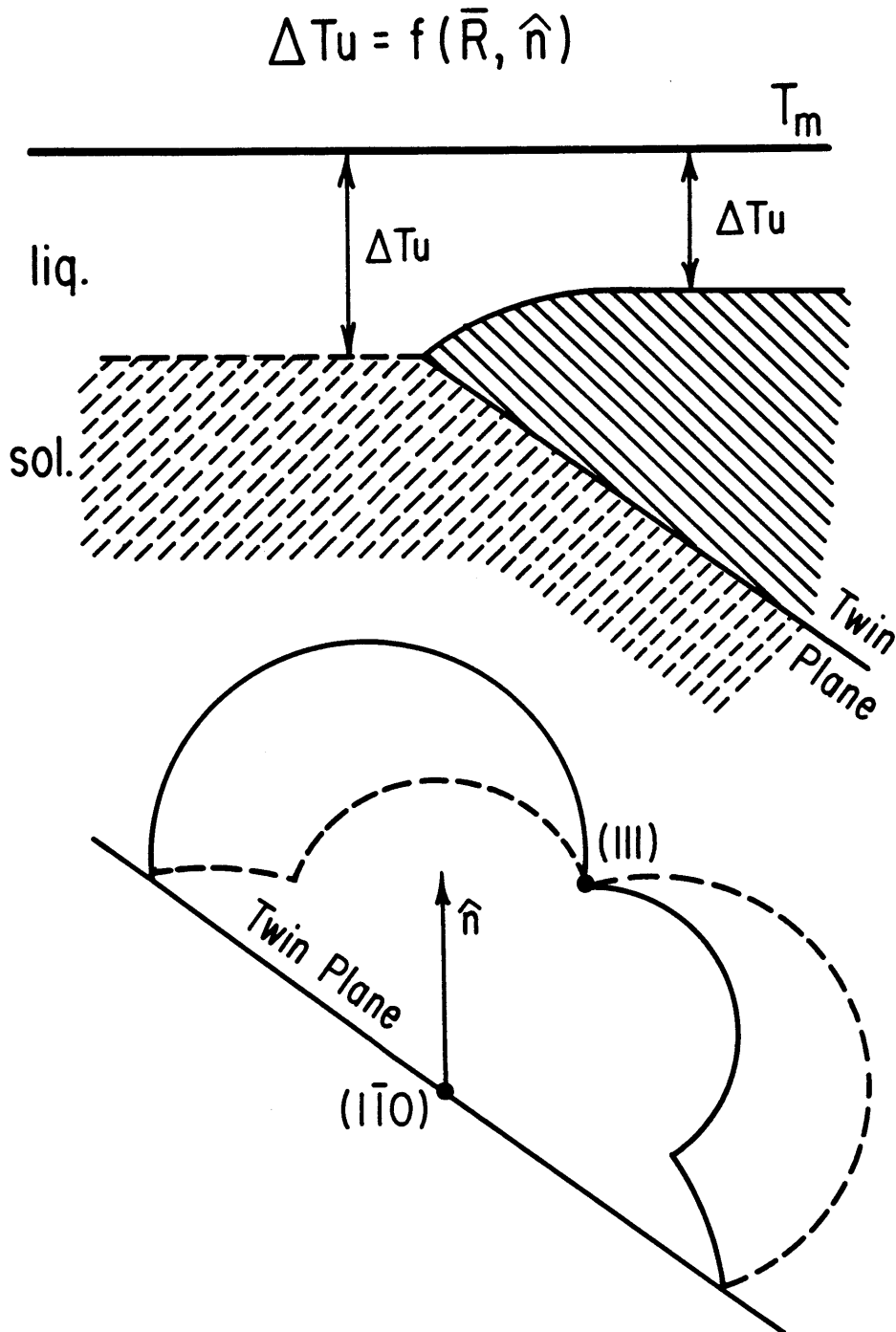
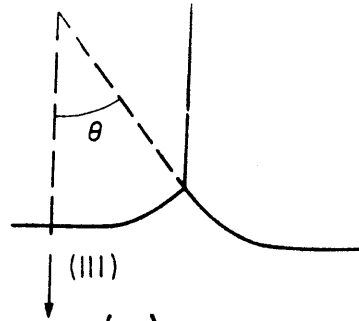
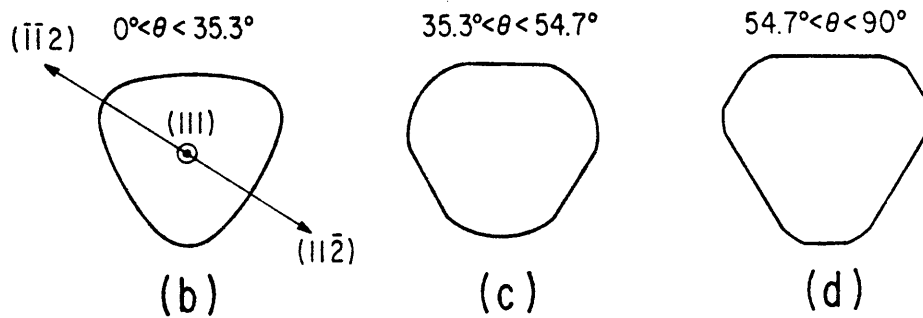


Fig. III.6.2 Cusp at advancing interface, due to anisotropic growth kinetics. The density of dangling bonds for the two grains is shown in a polar plot. The kinetic undercooling is indicated qualitatively



(a) Definition of interface curvature



Sequence of boule cross sections as a function of interface curvature

Fig. III.6.3 Qualitative external faceting behavior in elemental semiconductors

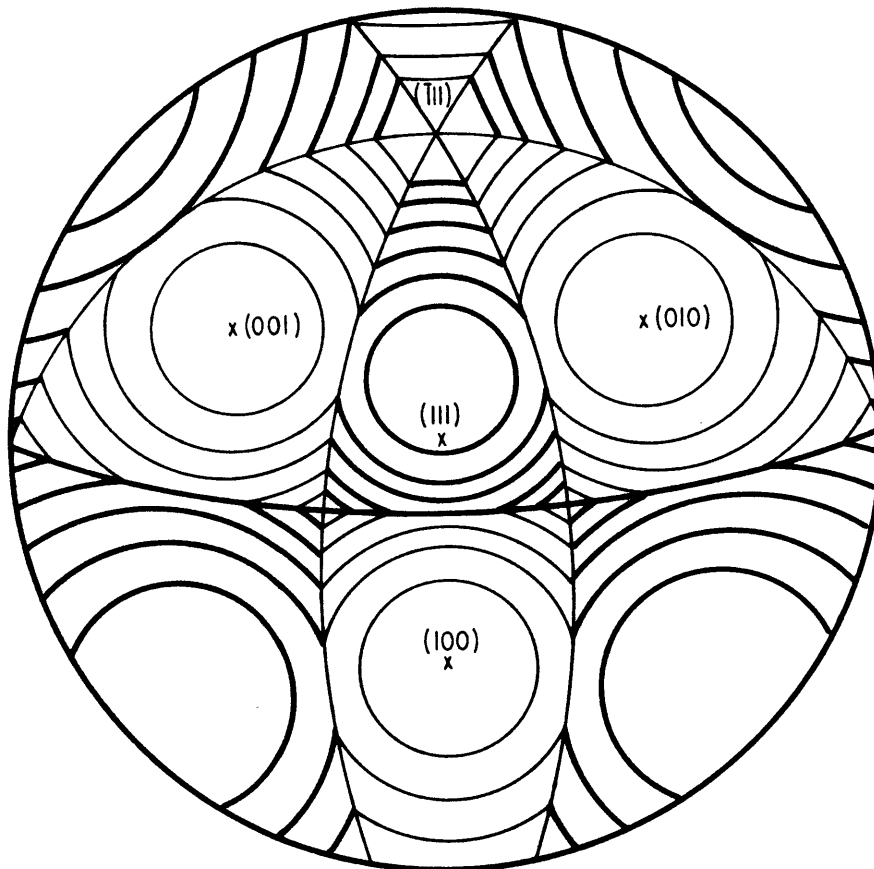


Fig. III.6.4 Effect of oblique $(\bar{1}\bar{1}\bar{1})$ twinning on the density of dangling bonds for a (111) seeded crystal. The composite curves select from the two crystal orientations the one with the higher density of dangling bonds

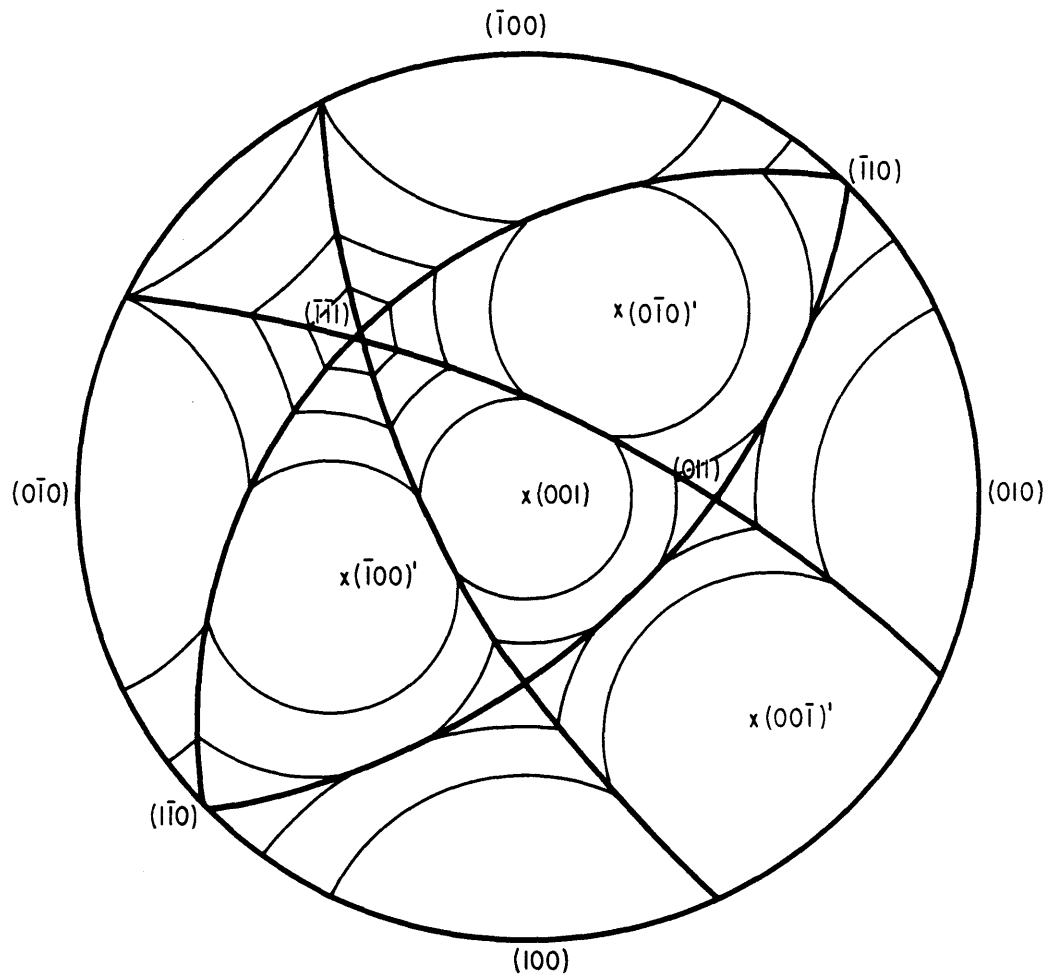


Fig. III.6.5 Effect of twinning on the density of dangling bonds for a (001) seeded crystal

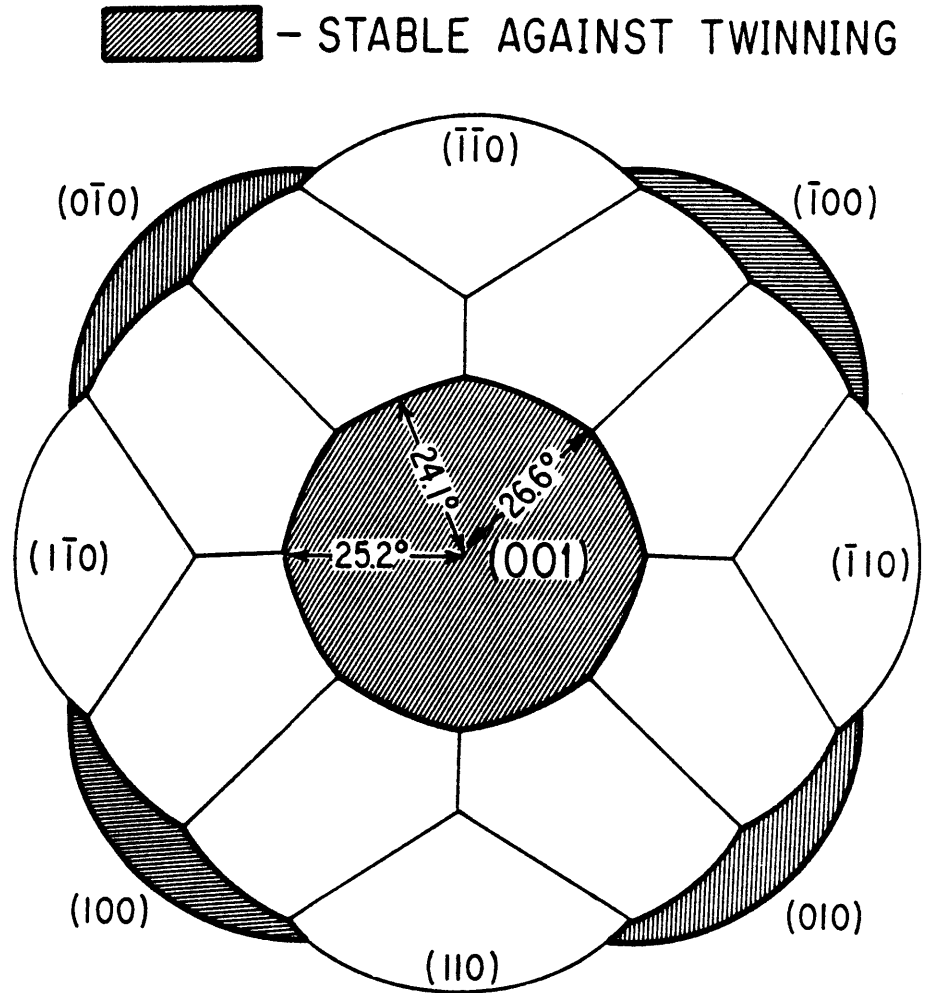


Fig. III.6.6 Stability map against twinning; a density-of-dangling-bonds composite surface for a (001) seeded crystal and all of its first-order twins (projection of the 3-dimensional surface onto the {001} surface)

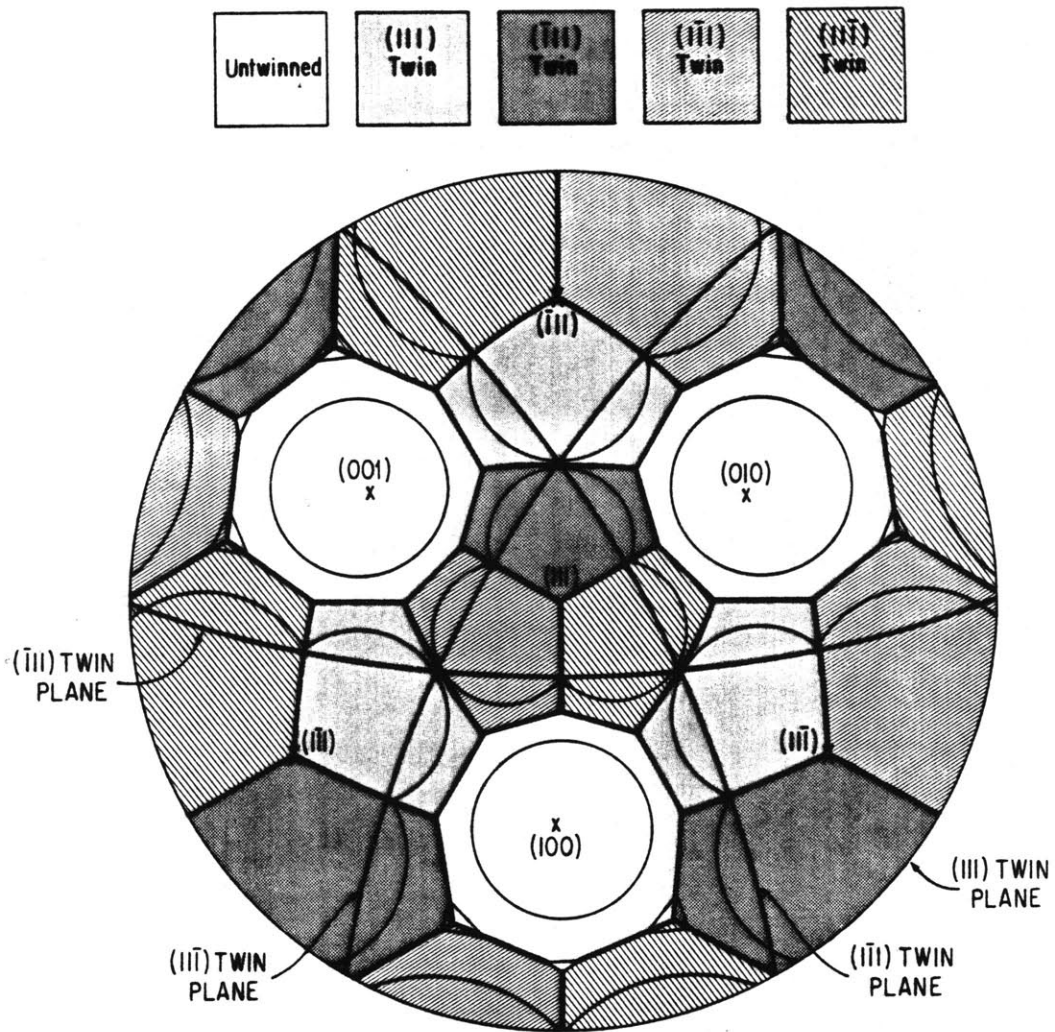
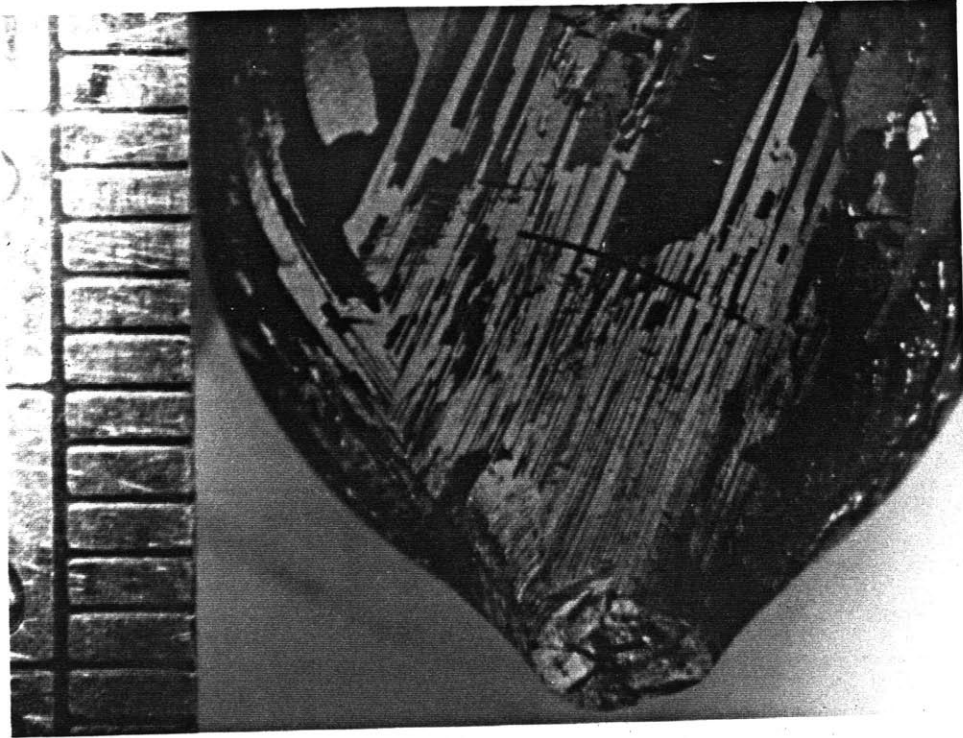
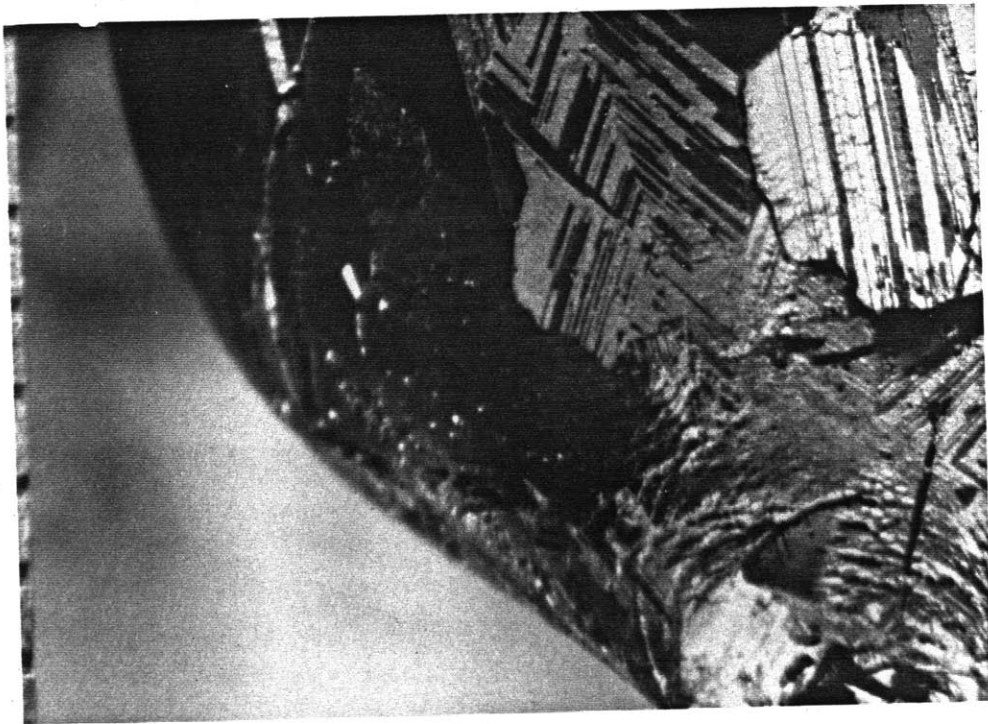


Fig. III.6.7 Stability map against twinning; shows preferred twin operations and stable regions vs. interface orientation



(a)



(b)

Fig. III.7.1 First to freeze portion of CdTe boule showing relatively uniform lamellar twinning

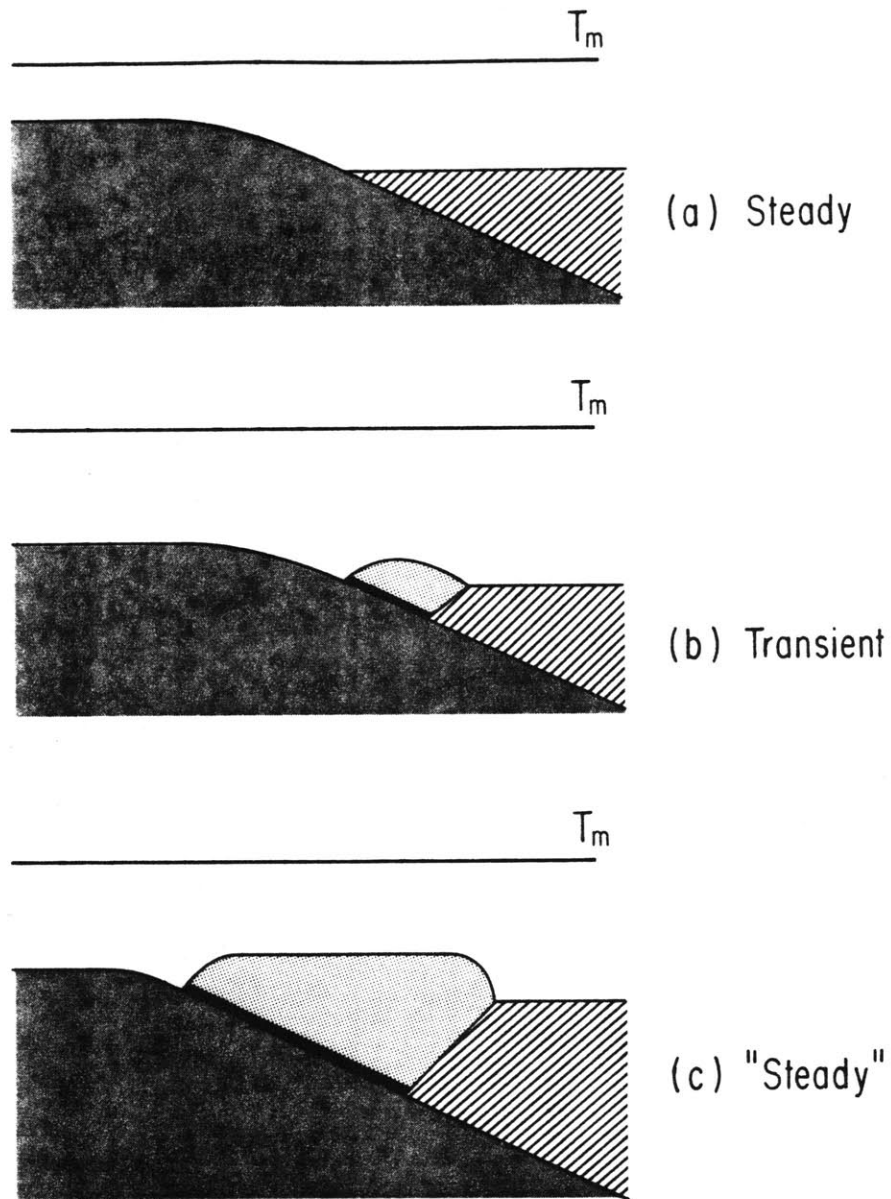


Fig. III.7.2 Initiation of a twin lamella from a twin boundary (schematic)

- (a) Cusp at solid-melt interface due to orientation difference across twin boundary
- (b) Nucleation of second order twin including a high energy boundary
- (c) The favorable orientation of the new grain gives it a lower kinetic undercooling

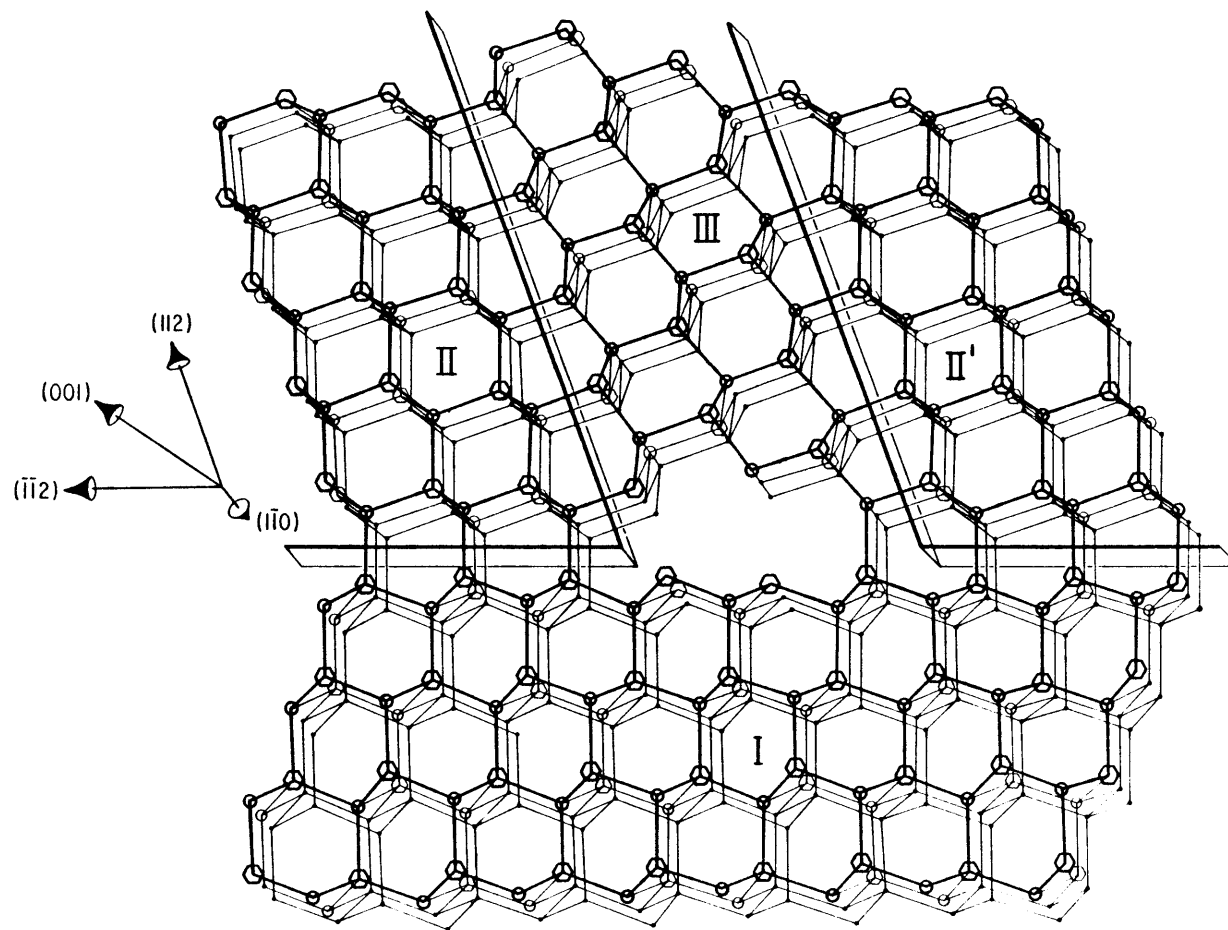
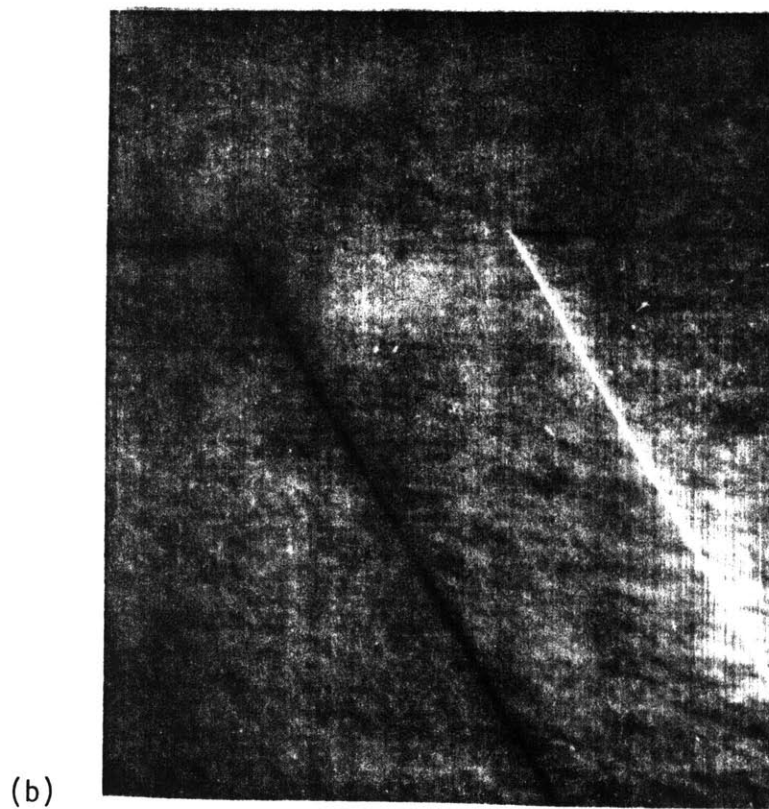
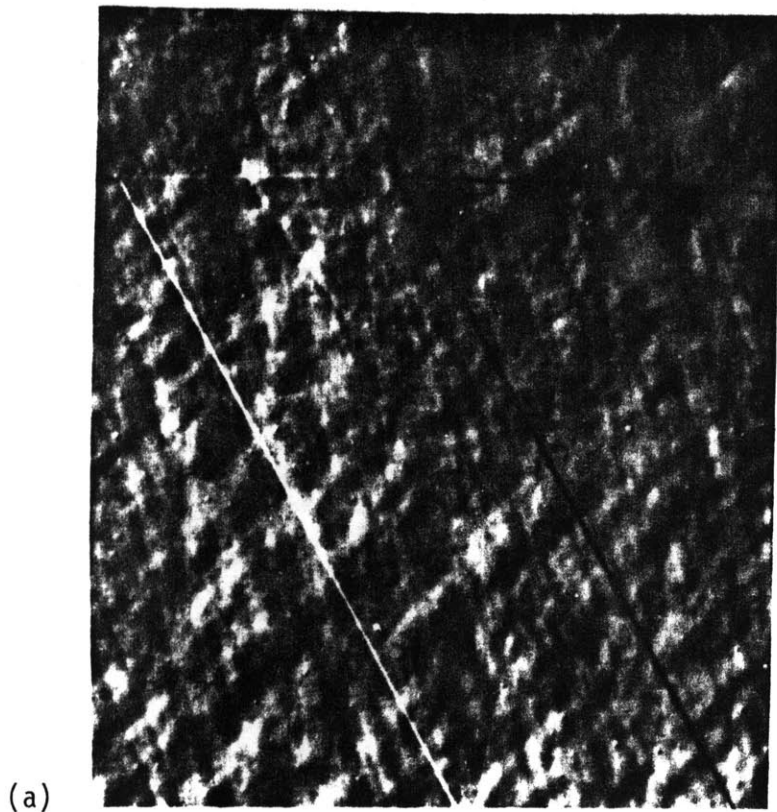


Fig. III.7.3a Atomic model of the thinnest (3 double layers) twin lamella allowed by crystallographic constraints

SURFACE PREPARATION OF CdTe

P. 189



Etched CdTe surface showing an example of a twin lamella (courtesy B. Fabes)
Fig. III.7.3 (concluded)

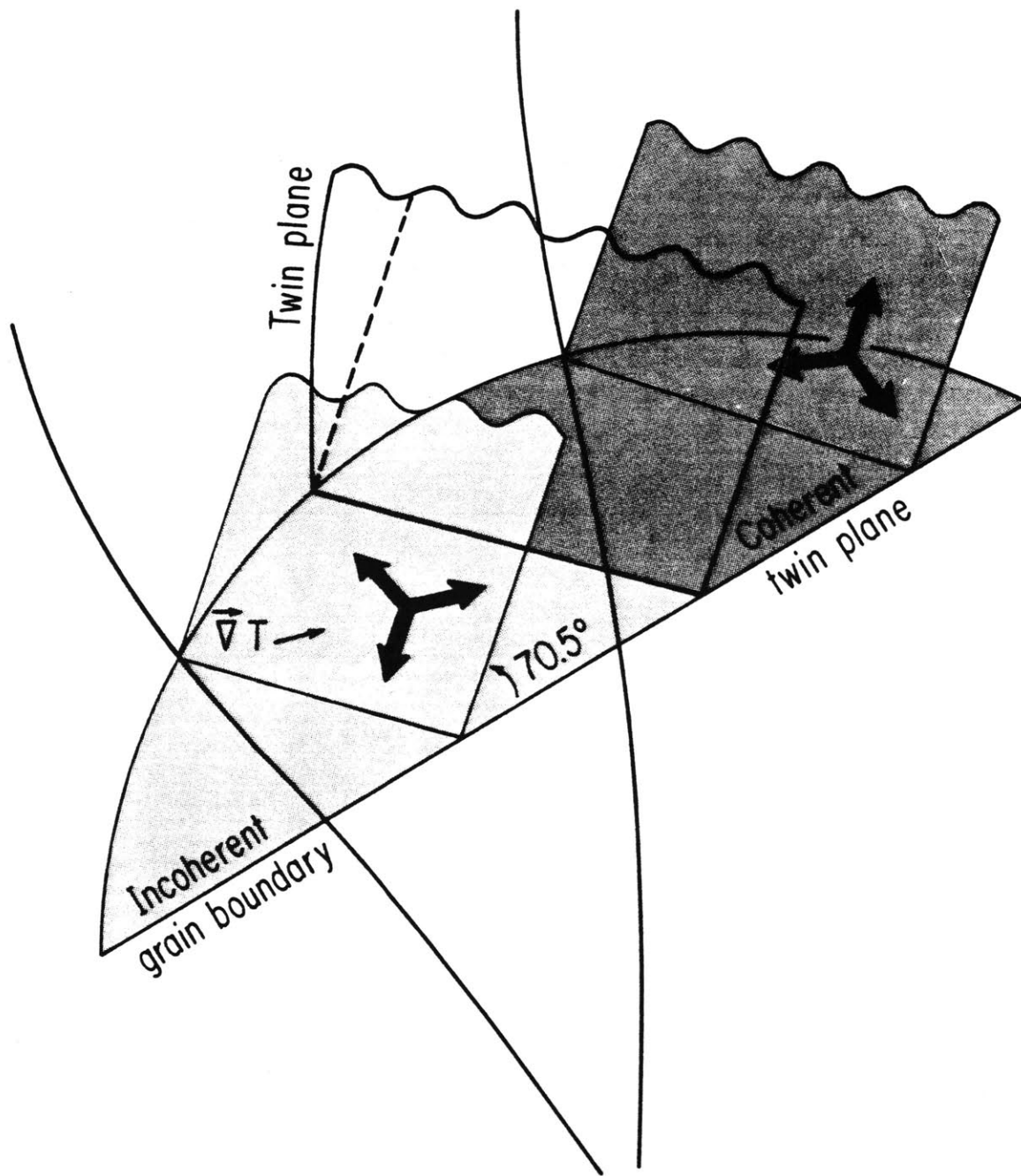


Fig. III.7.4a Lamellar twinning with acute dihedral angle towards the melt

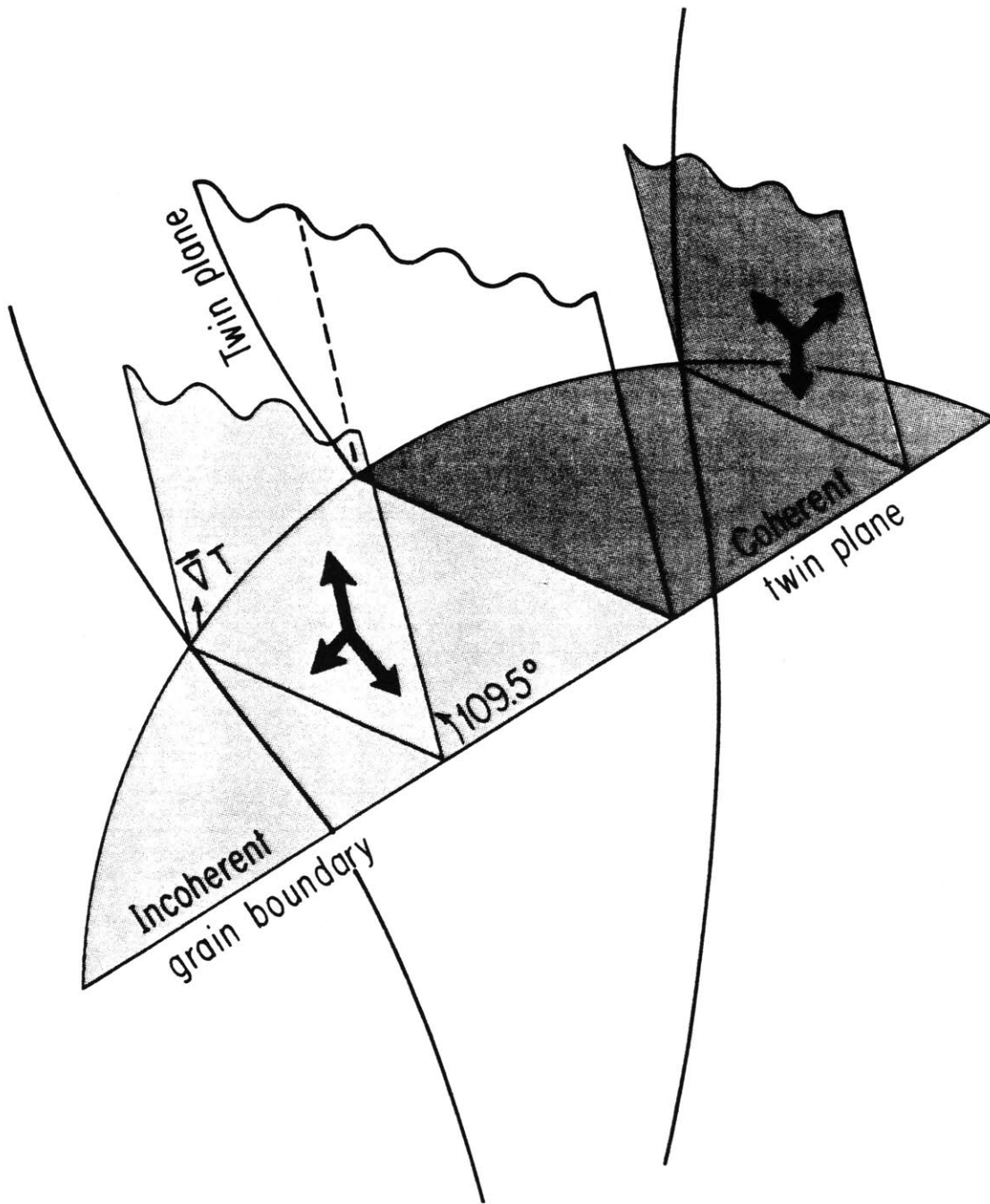


Fig. III.7.4b Lamellar twinning with obtuse dihedral angle towards the melt

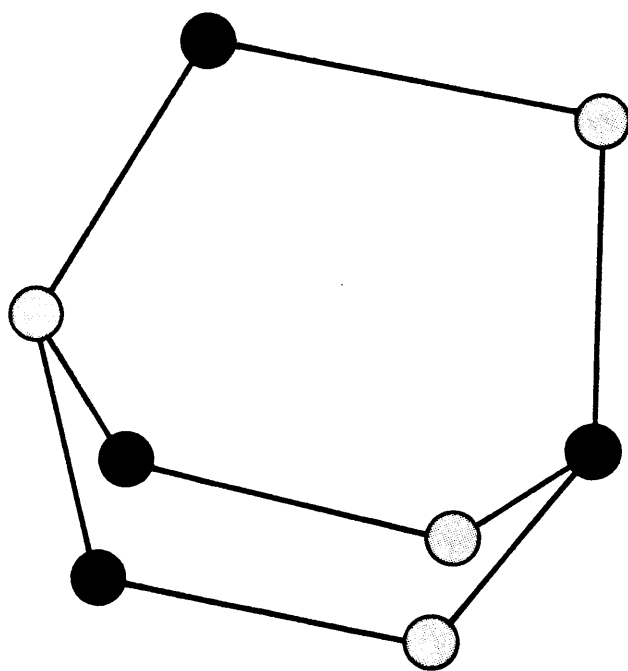


Fig. III.9.1 8-atom twin nucleus with an average of 1.75 dangling bonds per atom

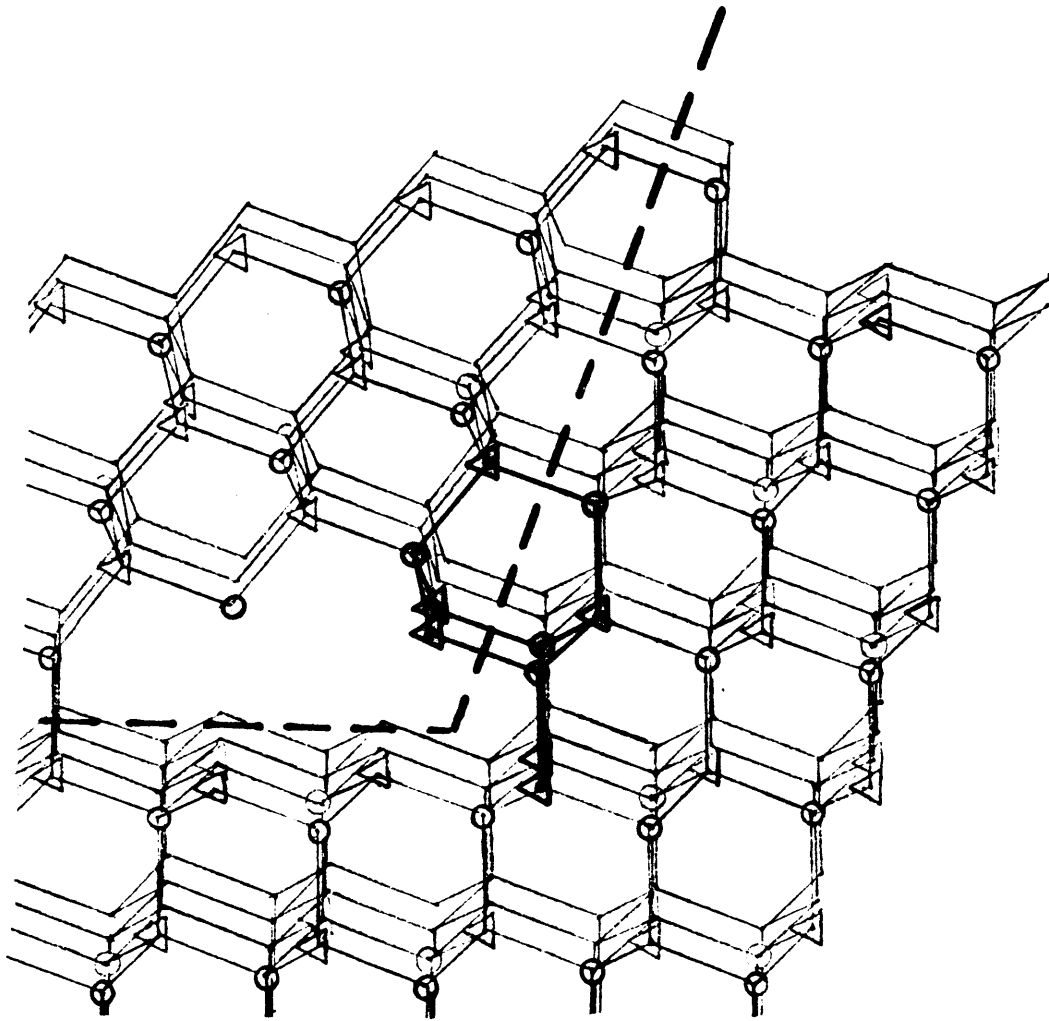


Fig. III.9.2 Initiation of oblique twin at 8-atom cluster

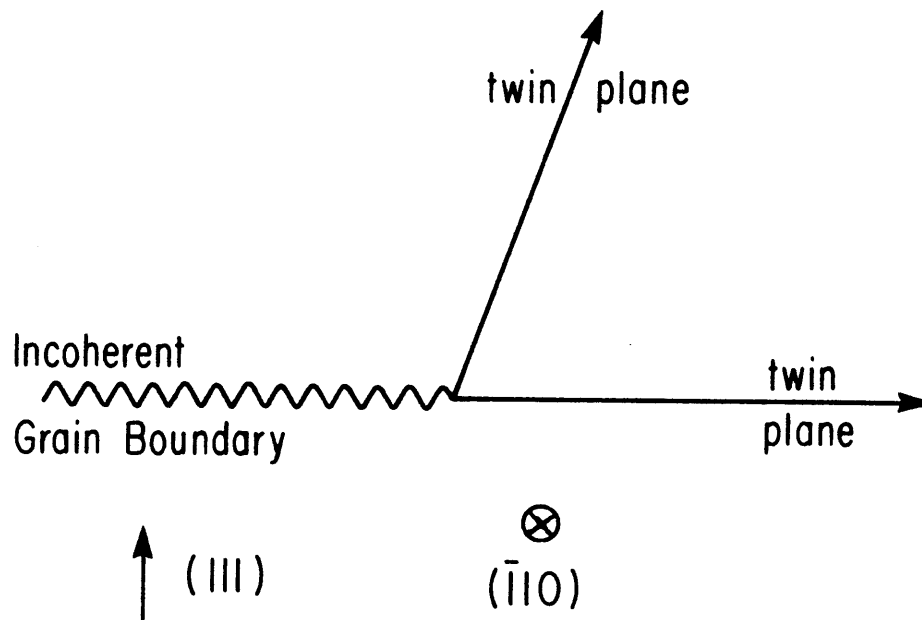
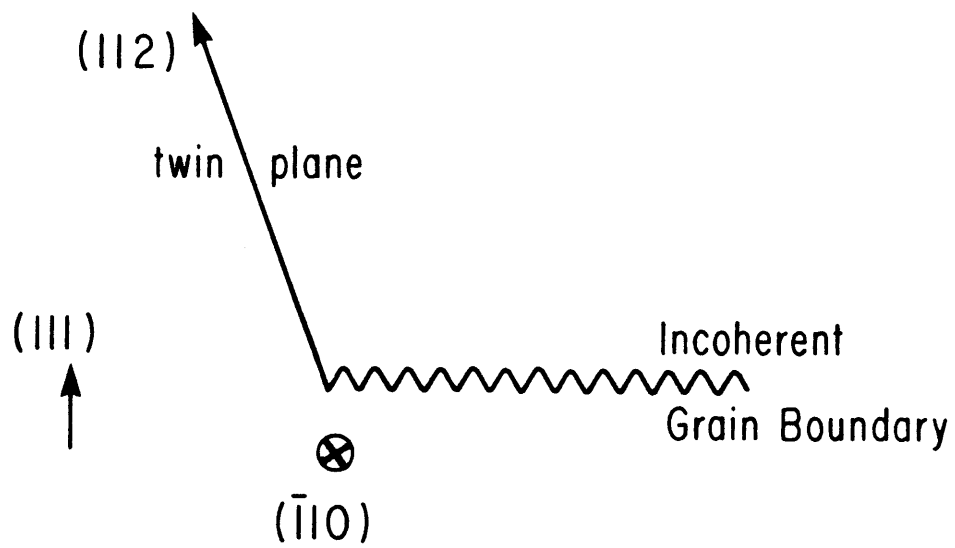


Fig. III.9.3 Crystallographically allowed oblique twin planes

$$GR > V\Delta Tu \frac{\partial^2 N_{\infty}}{\partial t \partial V} \quad (\text{No clusters})$$

$$\frac{G}{R} > m' \frac{C_{\infty}}{D} \frac{1-k_0}{k_0} \quad (\text{No constitutional supercooling})$$

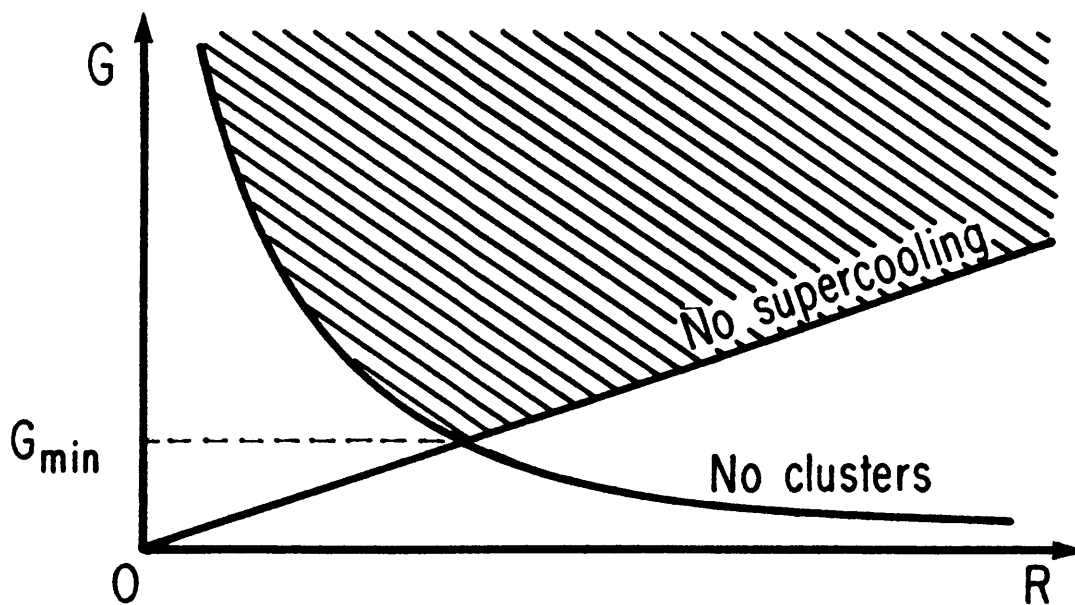


Fig. III.9.4 Stability region (cross hatched) against twinning in thermal gradient vs. growth rate space, as predicted by the clustering model

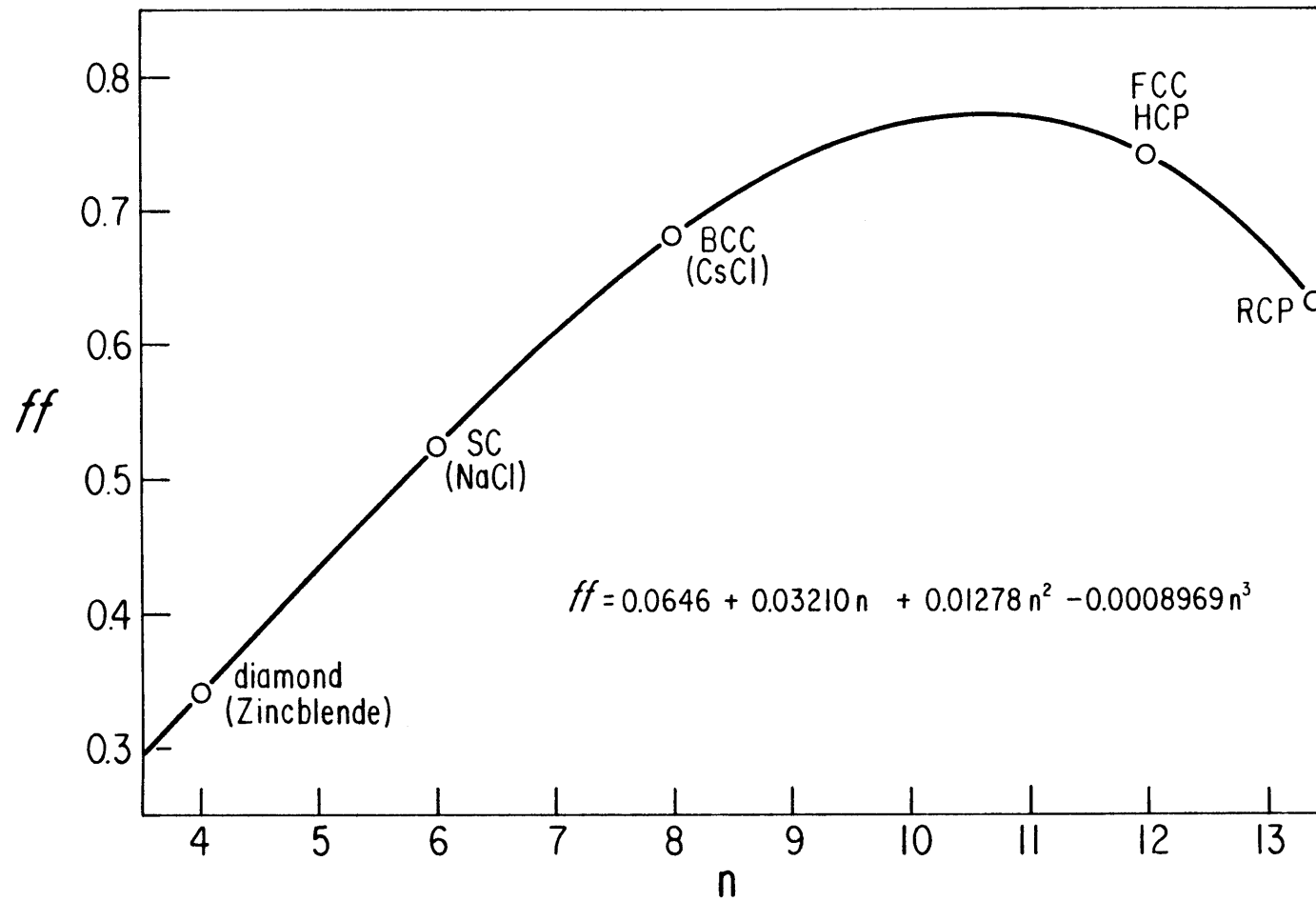
Fig. III.9.5 Filling factor (ff) (or packing fraction) vs. coordination number (n)

Table III.A2.1

Second axis \hat{u}_2 First axis \hat{u}_1	(III)	(ITT)	(TIT)	(TTI)
$R(111)$ $= \frac{1}{3} \begin{pmatrix} -1 & 2 & 2 \\ 2 & -1 & 2 \\ 2 & 2 & -1 \end{pmatrix}$	1	$\frac{1}{9} \begin{pmatrix} -7 & 4 & 4 \\ -4 & 1 & -8 \\ -4 & -8 & 1 \end{pmatrix}$	$\frac{1}{9} \begin{pmatrix} 1 & -4 & -8 \\ 4 & -7 & 4 \\ -8 & -4 & 1 \end{pmatrix}$	$\frac{1}{9} \begin{pmatrix} 1 & -8 & -4 \\ -8 & 1 & -4 \\ 4 & 4 & -7 \end{pmatrix}$
$R(1TT)$ $= \frac{1}{3} \begin{pmatrix} -1 & -2 & -2 \\ -2 & -1 & 2 \\ -2 & 2 & -1 \end{pmatrix}$	$\frac{1}{9} \begin{pmatrix} -7 & -4 & -4 \\ 4 & 1 & -8 \\ 4 & -8 & 1 \end{pmatrix}$	1	$\frac{1}{9} \begin{pmatrix} 1 & 8 & 4 \\ 8 & 1 & -4 \\ -4 & 4 & -7 \end{pmatrix}$	$\frac{1}{9} \begin{pmatrix} 1 & 4 & 8 \\ -4 & -7 & 4 \\ 8 & -4 & 1 \end{pmatrix}$
$R(TIT)$ $= \frac{1}{3} \begin{pmatrix} -1 & -2 & 2 \\ -2 & -1 & -2 \\ 2 & -2 & -1 \end{pmatrix}$	$\frac{1}{9} \begin{pmatrix} 1 & 4 & -8 \\ -4 & -7 & -4 \\ -8 & 4 & 1 \end{pmatrix}$	$\frac{1}{9} \begin{pmatrix} 1 & 8 & -4 \\ 8 & 1 & 4 \\ 4 & -4 & -7 \end{pmatrix}$	1	$\frac{1}{9} \begin{pmatrix} -7 & -4 & 4 \\ 4 & 1 & 8 \\ -4 & 8 & 1 \end{pmatrix}$
$R(TTI)$ $= \frac{1}{3} \begin{pmatrix} -1 & 2 & -2 \\ 2 & -1 & -2 \\ -2 & -2 & -1 \end{pmatrix}$	$\frac{1}{9} \begin{pmatrix} 1 & -8 & 4 \\ -8 & 1 & 4 \\ -4 & -4 & -7 \end{pmatrix}$	$\frac{1}{9} \begin{pmatrix} 1 & -4 & 8 \\ 4 & -7 & -4 \\ 8 & 4 & 1 \end{pmatrix}$	$\frac{1}{9} \begin{pmatrix} -7 & 4 & -4 \\ -4 & 1 & 8 \\ 4 & 8 & 1 \end{pmatrix}$	1

Table III.A2 . 2

$\sqrt{3} \hat{u}_1$	$\sqrt{3} \hat{u}_2$	$\frac{1}{\sqrt{3}} (111)$	$\frac{1}{\sqrt{3}} (1\bar{1}\bar{1})$	$\frac{1}{\sqrt{3}} (\bar{1}\bar{1}\bar{1})$	$\frac{1}{\sqrt{3}} (\bar{1}\bar{1}1)$	(100)	(010)	(001)
(111)		$\frac{1}{3\sqrt{3}} (111)$	$\frac{1}{3\sqrt{3}} (5\bar{1}1)$	$\frac{1}{3\sqrt{3}} (1\bar{5}1)$	$\frac{1}{3\sqrt{3}} (11\bar{5})$	$\frac{1}{3} (\bar{1}22)$	$\frac{1}{3} (2\bar{1}2)$	$\frac{1}{3} (22\bar{1})$
	(1 $\bar{1}\bar{1}$)	$\frac{1}{9\sqrt{3}} (1 \bar{1}\bar{1} \bar{1}\bar{1})$	$\frac{1}{3\sqrt{3}} (5\bar{1}1)$	$\frac{1}{9\sqrt{3}} (7 \ 13 \ \bar{5})$	$\frac{1}{9\sqrt{3}} (7 \ \bar{5} \ 13)$	$\frac{1}{9} (\bar{7}\bar{4}\bar{4})$	$\frac{1}{9} (4\bar{1}\bar{8})$	$\frac{1}{9} (4\bar{8}\bar{1})$
	($\bar{1}\bar{1}\bar{1}$)	$\frac{1}{9\sqrt{3}} (\bar{1}\bar{1} \ 1 \ \bar{1}\bar{1})$	$\frac{1}{9\sqrt{3}} (13 \ 7 \ \bar{5})$	$\frac{1}{3\sqrt{3}} (1 \ \bar{5} \ 1)$	$\frac{1}{9\sqrt{3}} (\bar{5} \ 7 \ 13)$	$\frac{1}{9} (14\bar{8})$	$\frac{1}{9} (\bar{4}\bar{7}\bar{4})$	$\frac{1}{9} (\bar{8}4\bar{1})$
	($\bar{1}\bar{1}1$)	$\frac{1}{9\sqrt{3}} (\bar{1}\bar{1} \ \bar{1}\bar{1} \ 1)$	$\frac{1}{9\sqrt{3}} (13 \ \bar{5} \ 7)$	$\frac{1}{9\sqrt{3}} (\bar{5} \ 13 \ 7)$	$\frac{1}{3\sqrt{3}} (11\bar{5})$	$\frac{1}{9} (1\bar{8}4)$	$\frac{1}{9} (\bar{8}14)$	$\frac{1}{9} (\bar{4}\bar{4}\bar{7})$
(1 $\bar{1}\bar{1}$)		$\frac{1}{3\sqrt{3}} (5\bar{1}\bar{1})$	$\frac{1}{\sqrt{3}} (1\bar{1}\bar{1})$	$\frac{1}{3\sqrt{3}} (1\bar{1}\bar{5})$	$\frac{1}{3\sqrt{3}} (15\bar{1})$	$\frac{1}{3} (\bar{1}\bar{2}\bar{2})$	$\frac{1}{3} (2\bar{1}\bar{2})$	$\frac{1}{3} (22\bar{1})$
	(111)	$\frac{1}{3\sqrt{3}} (5\bar{1}\bar{1})$	$\frac{1}{9\sqrt{3}} (1 \ 11 \ 11)$	$\frac{1}{9\sqrt{3}} (7 \ 5 \ \bar{1}\bar{3})$	$\frac{1}{9\sqrt{3}} (7 \ \bar{1}\bar{3} \ 5)$	$\frac{1}{9} (\bar{7}44)$	$\frac{1}{9} (4\bar{1}\bar{8})$	$\frac{1}{9} (4\bar{8}\bar{1})$
	($\bar{1}\bar{1}\bar{1}$)	$\frac{1}{9\sqrt{3}} (13 \ 5 \ \bar{7})$	$\frac{1}{9\sqrt{3}} (\bar{1}\bar{1} \ 11 \ \bar{1})$	$\frac{1}{3\sqrt{3}} (1 \ \bar{1} \ 5)$	$\frac{1}{9\sqrt{3}} (\bar{5} \ \bar{1}\bar{3} \ 7)$	$\frac{1}{9} (1\bar{8}4)$	$\frac{1}{9} (814)$	$\frac{1}{9} (44\bar{7})$
	($\bar{1}\bar{1}1$)	$\frac{1}{9\sqrt{3}} (13 \ \bar{7} \ 5)$	$\frac{1}{9\sqrt{3}} (\bar{1}\bar{1} \ \bar{1} \ 11)$	$\frac{1}{9\sqrt{3}} (\bar{5} \ \bar{7} \ \bar{1}\bar{3})$	$\frac{1}{3\sqrt{3}} (1 \ 5 \ \bar{1})$	$\frac{1}{9} (1\bar{4}\bar{8})$	$\frac{1}{9} (4\bar{7}\bar{4})$	$\frac{1}{9} (841)$
($\bar{1}\bar{1}\bar{1}$)		$\frac{1}{3\sqrt{3}} (\bar{1} \ \bar{5} \ \bar{1})$	$\frac{1}{3\sqrt{3}} (\bar{1} \ 1 \ 5)$	$\frac{1}{\sqrt{3}} (\bar{1} \ 1 \ \bar{1})$	$\frac{1}{3\sqrt{3}} (5 \ 1 \ \bar{1})$	$\frac{1}{3} (\bar{1}\bar{2}\bar{2})$	$\frac{1}{3} (2\bar{1}\bar{2})$	$\frac{1}{3} (22\bar{1})$
	(111)	$\frac{1}{3\sqrt{3}} (\bar{1} \ \bar{5} \ \bar{1})$	$\frac{1}{9\sqrt{3}} (5 \ 7 \ \bar{1}\bar{3})$	$\frac{1}{9\sqrt{3}} (11 \ 1 \ 11)$	$\frac{1}{9\sqrt{3}} (\bar{1}\bar{3} \ \bar{7} \ 5)$	$\frac{1}{9} (1\bar{4}\bar{8})$	$\frac{1}{9} (4\bar{7}\bar{4})$	$\frac{1}{9} (\bar{8}\bar{4}\bar{1})$
	($\bar{1}\bar{1}\bar{1}$)	$\frac{1}{9\sqrt{3}} (5 \ 13 \ \bar{7})$	$\frac{1}{3\sqrt{3}} (\bar{1} \ 1 \ 5)$	$\frac{1}{9\sqrt{3}} (11 \ \bar{1}\bar{1} \ \bar{1})$	$\frac{1}{9\sqrt{3}} (\bar{1}\bar{3} \ \bar{5} \ \bar{7})$	$\frac{1}{9} (184)$	$\frac{1}{9} (81\bar{4})$	$\frac{1}{9} (\bar{4}\bar{4}\bar{7})$
	($\bar{1}\bar{1}1$)	$\frac{1}{9\sqrt{3}} (\bar{7} \ 13 \ 5)$	$\frac{1}{9\sqrt{3}} (\bar{7} \ \bar{5} \ \bar{1}\bar{3})$	$\frac{1}{9\sqrt{3}} (\bar{1} \ \bar{1}\bar{1} \ 11)$	$\frac{1}{3\sqrt{3}} (5 \ 1 \ \bar{1})$	$\frac{1}{9} (\bar{7}\bar{4}\bar{4})$	$\frac{1}{9} (4\bar{1}\bar{8})$	$\frac{1}{9} (481)$
($\bar{1}\bar{1}1$)		$\frac{1}{3\sqrt{3}} (\bar{1} \ \bar{1} \ \bar{5})$	$\frac{1}{3\sqrt{3}} (\bar{1} \ 5 \ 1)$	$\frac{1}{3\sqrt{3}} (5 \ \bar{1} \ 1)$	$\frac{1}{\sqrt{3}} (\bar{1} \ \bar{1} \ 1)$	$\frac{1}{3} (\bar{1}\bar{2}\bar{2})$	$\frac{1}{3} (2\bar{1}\bar{2})$	$\frac{1}{3} (22\bar{1})$
	(111)	$\frac{1}{3\sqrt{3}} (\bar{1} \ \bar{1} \ \bar{5})$	$\frac{1}{9\sqrt{3}} (5 \ \bar{1}\bar{3} \ 7)$	$\frac{1}{9\sqrt{3}} (\bar{1}\bar{3} \ 5 \ 7)$	$\frac{1}{9\sqrt{3}} (11 \ 11 \ 1)$	$\frac{1}{9} (1\bar{8}4)$	$\frac{1}{9} (\bar{8}\bar{1}\bar{4})$	$\frac{1}{9} (44\bar{7})$
	($\bar{1}\bar{1}\bar{1}$)	$\frac{1}{9\sqrt{3}} (\bar{5} \ \bar{7} \ 13)$	$\frac{1}{3\sqrt{3}} (\bar{1} \ 5 \ 1)$	$\frac{1}{9\sqrt{3}} (\bar{1}\bar{3} \ \bar{7} \ \bar{5})$	$\frac{1}{9\sqrt{3}} (11 \ \bar{1} \ \bar{1}\bar{1})$	$\frac{1}{9} (148)$	$\frac{1}{9} (4\bar{7}\bar{4})$	$\frac{1}{9} (8\bar{4}\bar{1})$
	($\bar{1}\bar{1}1$)	$\frac{1}{9\sqrt{3}} (\bar{7} \ 5 \ 13)$	$\frac{1}{9\sqrt{3}} (\bar{7} \ \bar{1}\bar{3} \ \bar{5})$	$\frac{1}{3\sqrt{3}} (5 \ \bar{1} \ 1)$	$\frac{1}{9\sqrt{3}} (\bar{1} \ 11 \ \bar{1}\bar{1})$	$\frac{1}{9} (\bar{7}\bar{4}\bar{4})$	$\frac{1}{9} (418)$	$\frac{1}{9} (4\bar{8}\bar{1})$

Table III.A3.1

n	ff	System
4	$\frac{\pi \sqrt{3}}{16} \approx .3401$	diamond (zincblende)
6	$\frac{\pi}{6} \approx .5236$	SC (NaCl)
8	$\frac{\pi \sqrt{3}}{8} \approx .6802$	BCC (CsCl)
12	$\frac{\pi}{3\sqrt{2}} \approx .7405$	FCC , HCP